

Macroscopic Traffic Models with Behavior Variation Driven by Noise

by

John P. Wakefield

A dissertation submitted in partial fulfillment
of the requirements for the degree of
Doctor of Philosophy
(Applied and Interdisciplinary Mathematics)
in The University of Michigan
2022

Doctoral Committee:

Professor Smadar Karni
Professor Robert Krasny
Professor Giovanni Russo, Università di Catania
Professor Romesh Saigal

John P. Wakefield
jwake@umich.edu
ORCID iD 0000-0002-9123-873X

© John Wakefield 2022

ACKNOWLEDGEMENTS

I am very grateful for the assistance of my primary advisor Professor Smadar Karni whose keen insight and unending patience made this thesis possible. The modeling approach and presentation in this thesis have benefited immensely from her guidance. I would also like to thank my co-advisor Professor Romesh Saigal for his practical advice and oversight. I would also like to express appreciation to Professor Giovanni Russo for sitting on my committee; our discussions of models for capacity drop motivated the formulation of the models in this thesis. In addition, I would like to thank Professor Robert Krasny for being on my committee. Finally, I would like to acknowledge the administrative staff in the math department for their support throughout the graduate program.

TABLE OF CONTENTS

ACKNOWLEDGEMENTS	ii
LIST OF FIGURES	v
LIST OF TABLES	xi
ABSTRACT	xii
CHAPTER	
I. Overview of Macroscopic Continuum Traffic Modeling	1
1.1 Lighthill Whitham and Richards (LWR)	3
1.2 The Fundamental Diagram	7
1.2.1 Classic Fundamental Diagrams	8
1.2.2 A Linearized Fundamental Diagram	11
1.2.3 An Idealized Fundamental Diagram	13
1.3 Traffic Experiments	15
1.3.1 The Ringroad Experiment	15
1.3.2 The Speed Drop Experiment	17
1.4 Thesis Outline	20
II. A Heat Equation with White Noise Forcing	22
2.1 Independent Processes in Each Cell	22
2.2 Stochastic Heat Equation	25
2.3 Parameters	28
2.4 Numerical Approximation	32
III. Stochastic Equilibrium Traffic Models	37
3.1 LWR on the Uncoupled Stochastic Heat Equation	38
3.1.1 Numerical Methods	39
3.1.2 Parameters in the Stochastic Heat Equation	40

3.1.3	The Ringroad Experiment	43
3.2	A Stochastic Extension to LWR with Constant Coefficients	43
3.2.1	Hyperbolicity, Anisotropy, and Boundedness	46
3.2.2	Vehicles have Personalities that Remain Unchanged by Motion	48
3.2.3	Numerical Methods	48
3.2.4	The Ringroad Experiment	51
3.3	Stochastic Extension to LWR with Density Dependent Coefficients	58
3.3.1	Numerical Methods	59
3.3.2	The Ringroad Experiment	59
3.3.3	The Speed Drop Experiment	66
3.4	Similarity to Non-Equilibrium Models	66
3.5	Higher Dimensional Representations of Driver Variation	70
3.6	Conclusion	70
IV.	Non-Equilibrium Traffic Models	72
4.1	General Form for Non-Equilibrium Models	73
4.1.1	Properties of the Hyperbolic Part	75
4.1.2	Stability	77
4.2	Payne	80
4.3	Aw, Rascle, and Zhang	81
4.4	Song and Karni	82
4.5	Numerical Considerations	85
4.6	Generalized Second Order Models (GSOM)	87
V.	Stochastic Non-Equilibrium Traffic Models	92
5.1	Stochastic Second-Order Models with an Auxiliary z Equation	93
5.1.1	Numerical Approximation	95
5.1.2	Ringroad	96
5.1.3	Speed drop	106
5.2	Stochastic Second-Order Models with Direct Noise	106
5.2.1	Numerical Approach	109
5.2.2	Ringroad	114
5.3	Conclusion	116
VI.	Conclusion	117
6.1	Equilibrium Models	118
6.2	Non-Equilibrium Models	119
6.3	Future Directions	120
APPENDICES		121
BIBLIOGRAPHY		133

LIST OF FIGURES

Figure

1.1	An illustration of the traffic quantities in Table 1.1.	1
1.2	Mean density-velocity relationship and standard deviation computed from the NGSIM [50] data. This data does not provide accurate velocities at low densities.	7
1.3	A selection of well known fundamental diagrams (Equations 1.16 through 1.18).	9
1.4	The ‘linearized’ fundamental diagram $V^{LF}(\rho, z) = V_0^{LF}(\rho) + zV_1^{LF}(\rho)$ plotted with parameters shown in Table 1.2.	10
1.5	A new fundamental diagram with dependence upon a deviation parameter z	14
1.6	Illustration of the ringroad experiment initial condition (a) and the congested pattern that evolves (b).	16
1.7	The speed drop experiment as realized by the LWR model (Equation 1.7) with the fundamental diagram presented in Section 1.2.2. The left plot contains density profiles at uniformly spaced times that increase as they go up the page. The right depicts vehicle trajectories spaced proportional to traffic density.	17
1.8	Transit time through the domain as a function of time corresponding to the vehicle trajectories shown in Figure 1.7.	18
1.9	Chapter dependency chart.	20
2.1	An illustration of several independent Ornstein-Uhlenbeck processes at a variety of points in space (left), contrasted to a set of stochastic processes correlated in space (right). The examples on the right are a representation of the process and parameters found in Section 2.2.	23
2.2	Characterization of a variety of solutions to Equation 2.3. Compare this Figure 2.6.	24
2.3	Four independent example realizations of z (Equation 2.4) using $\eta = 5.7742 \times 10^{-1}$, $\kappa = 2.4522 \times 10^{-4}$, and $\tau^z = 3.5294 \times 10^{-2}$. The domain is approximated by 800 cells.	26
2.4	Example realizations of the stochastic heat equation with and without advection using $\eta = 5.7742 \times 10^{-1}$, $\kappa = 2.4522 \times 10^{-4}$, and $\tau^z = 3.5294 \times 10^{-2}$. overlaid at $t = 0.02$. The domain is approximated by 800 cells.	27

2.5	Example realizations of the stochastic heat equation with constant advection (Equation 2.16) with velocity $v = 5.0$ using $\eta = 5.7742 \times 10^{-1}$, $\kappa = 2.4522 \times 10^{-4}$, and $\tau^z = 3.5294 \times 10^{-2}$. The domain is approximated by 800 cells.	33
2.6	Summary statistics of example realizations of Equation 2.4 computed using the method of Section 2.4. Note that, unlike the results shown in Figure 2.2, the behavior of this process is consistent as the computational mesh is refined.	34
3.1	An illustration of covariance in z with respect to differences in length and time. These curves are fully determined by the selection of σ^2 (the maximum of the two curves), the chosen $(\rho_{\text{ref}}^{-1}, \sigma_x^2)$ pair (red dots on upper plot), and the (δ, σ_t^2) pair (red dots on lower plot).	40
3.2	Statistics of $\frac{V_0(\rho) - v}{V_1(\rho)}$ for individual cars where $V_0(\rho)$ and $V_1(\rho)$ are the mean and standard deviation respectively of velocity at a given density computed from NGSIM [50] vehicle trajectories.	41
3.3	Four realizations of the ringroad experiment using LWR modified by a (decoupled) random process z (Equation 3.2). The linearized fundamental diagram (Equation 1.21) and the parameters in Table 1.2 with $\omega = 1$ were used with an initial density of $\rho_0 = 120.0$. Each row represents an independent realization. The first column shows the density profile at the initial time, and early time, and a later (fully developed) time; the second column shows the velocity profile at the same times; the third column shows sample vehicle trajectories.	44
3.4	Four realizations of the ringroad experiment using LWR modified by a (decoupled) random process z (Equation 3.2). The linearized fundamental diagram (Equation 1.21) and the parameters in Table 1.2 with $\omega = 1$ were used with an initial density of $\rho_0 = 140.0$. Each row represents an independent realization. The first column shows the density profile at the initial time, and early time, and a later (fully developed) time; the second column shows the velocity profile at the same times; the third column shows sample vehicle trajectories.	45
3.5	Realizations of the ringroad experiment using the LWRZ model (Equation 3.10) using the linearized fundamental diagram (Equation 1.21) and the parameters in Table 1.2. The initial density is $\rho_0 = 80.0$ and $\omega = 1.0$. Each row represents an independent realization. The first column shows the density profile at the initial time, and early time, and a later (fully developed time); the second column shows the velocity profile at the same times; the third column shows vehicle trajectories.	52
3.6	Realizations of the ringroad experiment using the LWRZ model (Equation 3.10) using the linearized fundamental diagram (Equation 1.21) and the parameters in Table 1.2. The initial density is $\rho_0 = 130.0$ and $\omega = 1.0$. Each row represents an independent realization. The first column shows the density profile at the initial time, and early time, and a later (fully developed time); the second column shows the velocity profile at the same times; the third column shows vehicle trajectories.	53

3.7	Realizations of the ringroad experiment using the LWRZ model (Equation 3.10) using the linearized fundamental diagram (Equation 1.21) and the parameters in Table 1.2. The initial density is $\rho_0 = 80.0$ and $\omega = 1.2$. Each row represents an independent realization. The first column shows the density profile at the initial time, and early time, and a later (fully developed time); the second column shows the velocity profile at the same times; the third column shows vehicle trajectories.	54
3.8	Realizations of the ringroad experiment using the LWRZ model (Equation 3.10) using the linearized fundamental diagram (Equation 1.21) and the parameters in Table 1.2. The initial density is $\rho_0 = 130.0$ and $\omega = 1.2$. Each row represents an independent realization. The first column shows the density profile at the initial time, and early time, and a later (fully developed time); the second column shows the velocity profile at the same times; the third column shows vehicle trajectories.	55
3.9	Histograms showing the distribution of the final time to traverse the domain (i.e. the last traversal before $t = 0.08$) across realizations of Equation 3.10 with constant coefficients as the amplitude of noise (ω) varies. Background density is $\rho_0 = 130.0$. Each histogram is compiled from 400 realizations.	56
3.10	Histograms showing the distribution of minimum velocity at $t = 0.08$ across realizations of Equation 3.10 with constant coefficients as the level of noise (ω) varies. Background density is $\rho_0 = 130.0$. Each histogram is compiled from 400 realizations.	57
3.11	Realizations of the ringroad experiment using the LWRZ model (Equation 3.10) with variable coefficients (Equations 3.26 and 3.27). The linearized fundamental diagram (Equation 3.10) with parameters in Table 1.2 was used. The initial density is $\rho_0 = 100.0$ and $\omega = 1.0$. Each row represents an independent realization. The first column shows the density profile at the initial time, and early time, and a later (fully developed time); the second column shows the velocity profile at these times; the third column contains vehicle trajectories.	60
3.12	Realizations of the ringroad experiment using the LWRZ model (Equation 3.10) with variable coefficients (Equations 3.26 and 3.27). The linearized fundamental diagram (Equation 3.10) with parameters in Table 1.2 was used. The initial density is $\rho_0 = 130.0$ and $\omega = 1.0$. Each row represents an independent realization. The first column shows the density profile at the initial time, and early time, and a later (fully developed time); the second column shows the velocity profile at these times; the third column contains vehicle trajectories.	61

3.13	Realizations of the ringroad experiment using the LWRZ model (Equation 3.10) with variable coefficients (Equations 3.26 and 3.27). The linearized fundamental diagram (Equation 3.10) with parameters in Table 1.2 was used. The initial density is $\rho_0 = 100.0$ and $\omega = 1.2$. Each row represents an independent realization. The first column shows the density profile at the initial time, and early time, and a later (fully developed time); the second column shows the velocity profile at these times; the third column contains vehicle trajectories.	62
3.14	Realizations of the ringroad experiment using the LWRZ model (Equation 3.10) with variable coefficients (Equations 3.26 and 3.27). The linearized fundamental diagram (Equation 3.10) with parameters in Table 1.2 was used. The initial density is $\rho_0 = 130.0$ and $\omega = 1.2$. Each row represents an independent realization. The first column shows the density profile at the initial time, and early time, and a later (fully developed time); the second column shows the velocity profile at these times; the third column contains vehicle trajectories.	63
3.15	Distribution of times taken to traverse the domain immediately before $t = 0.08$ under Equation 3.10 with coefficients varied according to Equations 3.27 and 3.26. The background density is $\rho_0 = 130.0$. Each histogram is compiled from 400 realizations.	64
3.16	Distribution of minimum velocity across the domain at $t = 0.08$ under Equation 3.10 with coefficients varied according to Equations 3.27 and 3.26. The background density is $\rho_0 = 130.0$. Each histogram is compiled from 400 realizations.	65
3.17	Example realizations of the speed drop experiment (Section 1.3.2) using Equation 3.10 with variable coefficients. Here $\omega = 1$	67
3.18	Average travel times from the inlet to the outlet of the speed drop experiment as modeled by Equation 3.10 with variable coefficients averaged across 40 realizations per value of ω	68
4.1	Evaluation of $\rho_e + \frac{g(\rho_e)}{V_\rho(\rho_e)}$ for a variety of densities ρ_e , $g(\rho)$ given in Equation 4.39, and fundamental diagrams given by Equation 1.18 (left) and Equation 1.21 (right). Parameters can be found in Tables 4.3, 1.2, and 4.2. The densities appearing in Figure 4.2, Figure 4.3, and Figure 4.4 are marked with red dots.	85
4.2	Numerical solutions to Equation 4.37 using the fundamental diagram found in Kerner [30] (Equation 1.18), parameters in Tables 4.2 and 4.3, and a small initial disturbance. The mean densities from top to bottom are $\rho_0 = 60.0$, $\rho_0 = 70.0$, and $\rho_0 = 90.0$. Solutions for higher densities are shown in Figure 4.3.	89
4.3	Numerical solutions to Equation 4.37 using the fundamental diagram found in Kerner [30] (Equation 1.18), parameters in Tables 4.2 and 4.3, and a small initial disturbance. The mean densities are $\rho_0 = 110.0$ (top) and $\rho_0 = 120.0$ (bottom). For lower densities see Figure 4.2.	90

4.4	Numerical solutions to Equation 4.37 using the linearized fundamental diagram (Equation 1.21), parameters in Tables 4.2 and 1.2, and a small initial disturbance. The mean densities from top to bottom are $\rho_0 = 40.0$, $\rho_0 = 50.0$, $\rho_0 = 60.0$, $\rho_0 = 70.0$, $\rho_0 = 80.0$	91
5.1	Example realizations of the ringroad experiment using Equation 5.1 with constant coefficients η and κ with an initial uniform density of 50.0. . . .	97
5.2	Example realizations of the ringroad experiment using Equation 5.1 with constant coefficients η and κ with an initial uniform density of 60.0. . . .	98
5.3	Example realizations of the ringroad experiment using Equation 5.1 with variable coefficients (Equation 3.25) with an initial uniform density of 40.0.	99
5.4	Example realizations of the ringroad experiment using Equation 5.1 with variable coefficients (Equation 3.25) with an initial uniform density of 50.0.	100
5.5	Example realizations of the ringroad experiment using Equation 5.1 with variable coefficients (Equation 3.25a) with an initial uniform density of 60.0.	101
5.6	Example realizations of the ringroad experiment using Equation 5.1 with variable coefficients (Equation 3.25a) with an initial uniform density of 70.0.	102
5.7	Distribution of velocity range at $t = 0.12$ for the ringroad experiment under Equation 5.1 with variable coefficients. Red vertical lines represent the velocity at this time under the deterministic equations with an initial density perturbation per Figure 4.4.	104
5.8	For example realizations of the ‘speed drop’ experiment under Equation 5.1 and $\omega = 1.0$	105
5.9	Speed drop experiment under Equation 5.1 and $\omega = 1.2$	105
5.10	Travel times in the speed drop experiment as a function of start time for selected values of ω , averaged over several realizations.	106
5.11	Example realizations of the ringroad experiment under Equation 5.9 with parameters in Table 4.2 and Table 5.1 and initial uniform density of $\rho_0 = 40.0$	110
5.12	Example realizations of the ringroad experiment under Equation 5.9 with parameters in Table 4.2 and Table 5.1 and initial uniform density of $\rho_0 = 50.0$	111
5.13	Example realizations of the ringroad experiment under Equation 5.9 with parameters in Table 4.2 and Table 5.1 and initial uniform density of $\rho_0 = 60.0$	112
5.14	Example realizations of the ringroad experiment under Equation 5.9 with parameters in Table 4.2 and Table 5.1 and initial uniform density of $\rho_0 = 70.0$	113
5.15	Distribution of velocity range at $t = 0.16$ for the ringroad experiment under Equation 5.9 with variable coefficients. Red vertical lines represent the velocity at this time under the deterministic equations with an initial density perturbation per Figure 4.4.	115
A.1	Example non-dimensional eigenvalues of the Jacobian (Equation A.9) evaluated at the steady state of equidistant vehicles.	124

A.2	An example realization of the car-following model Equation A.19. The left shows vehicle trajectories exhibiting development of stop and go waves whereas the right shows the corresponding behavioral ‘ z_n ’ variables.	128
A.3	An example realization of the car-following model Equation A.20. The left shows vehicle trajectories exhibiting development of stop and go patterns whereas the right shows the corresponding velocities (v_n).	129

LIST OF TABLES

Table

1.1	Microscopic traffic quantities and their macroscopic analogs. Some of these quantities are illustrated in Figure 1.1.	2
1.2	Parameters used in the linearized fundamental diagram (Equation 1.21).	11
3.1	Parameters used to evolve z (Equations 3.2 and 3.10) in this chapter. The tables on the left and right are equivalent through Equations 3.7a, 3.7b, and 3.7c (or alternatively Equations 3.25a, 3.25b, and 3.25c). Note these are the same parameters used throughout Chapter II.	41
4.1	Common formulas for $g(\rho)$ for traffic models in the form of Equation 4.9.	77
4.2	Parameters used for the model proposed by Song and Karni (Equation 4.37) and its stochastic counterparts (Equation 5.1).	84
4.3	Parameters used for the fundamental diagram given by Equation 1.18 in Figure 4.1. These parameters are similar to those used in [27, 59].	84
5.1	Parameters used for demonstrations of Equation 5.9.	109

ABSTRACT

Hyperbolic PDE can be used to describe the macroscopic dynamics of traffic flow. Models of traffic flow with conservation laws begin with conservation of mass. Equilibrium models (also called first order models) are scalar conservation laws with an explicit closure relation, called the *Fundamental Diagram* (FD), describing velocity as a function of density. The FD is largely approximated from observation, and in general velocity is a non-increasing function of density. Driver behavior, however, differs among drivers and over time; this variability is not captured by deterministic models. Real data suggests that while one may identify ‘mean’ driver behavior due to non-equilibrium effects and general variability in driving style there is some distribution around the mean. To model driver variability, we introduce a driver-related parameter that describes deviation from the mean and create a family of fundamental diagrams that provide velocity as a function of both density and this parameter. The parameter is governed by an advection diffusion equation with white noise forcing and a relaxation to mean behavior. The resulting models adhere to accepted principles for traffic modeling and are capable of reproducing a richer set of traffic flow phenomena. Most notably, they illustrate that small perturbations may grow into large coherent wave structures, including the formation of jams and emergence of stop-and-go flow patterns, in equilibrium models. Dynamic generalizations have been proposed by numerous authors and describe a velocity that does not instantaneously adjust to traffic density, but instead is governed by an additional equation. In addition to modeling driver variation

as an auxiliary variable, these models also permit variation of velocity through a direct modification to the velocity equation. In the present work equilibrium and non-equilibrium traffic models with a stochastic behavior variable are presented, as is a direct stochastic velocity perturbation.

CHAPTER I

Overview of Macroscopic Continuum Traffic Modeling

One approach to traffic modeling is to describe the evolution of macroscopic quantities (e.g. density) with hyperbolic PDE. ‘Macroscopic’ means that we will attempt to prescribe dynamics to space-averaged quantities rather than ‘microscopic’ quantities pertaining to relationships between individual vehicles. An analogy can and will frequently be made between the two approaches (see Table 1.1). Though not the focus of this work, we will include a discussion of microscopic car-following models (Appendix A) to the extent that they are analogs to the PDE models developed herein. There are macroscopic models that are not PDE models, including many with stochasticity (e.g. supply/demand [3, 7, 20, 35] and cellular automata models [17, 47, 56, 44, 1]). Mesoscopic models, describing dynamics

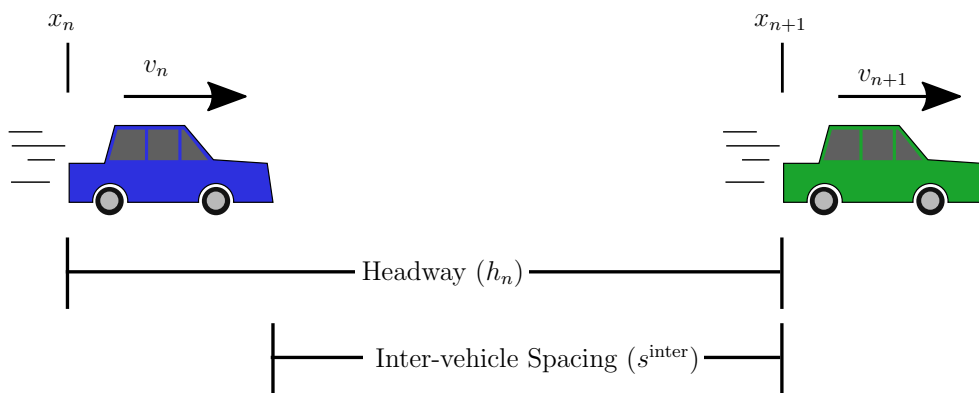


Figure 1.1: An illustration of the traffic quantities in Table 1.1.

Table 1.1: Microscopic traffic quantities and their macroscopic analogs. Some of these quantities are illustrated in Figure 1.1.

Microscopic Quantities		Macroscopic Quantities	
Position of car n	x_n	Density	ρ
Velocity of car n	v_n	Velocity	v
Inter-vehicle Spacing	$s_n^{\text{inter}} = x_{n+1} - x_n - \ell_c$	Mean Inter-vehicle Spacing	$\frac{1}{\rho} - \ell_c$
Minimum Intervehicle Spacing	$s_{\text{min}}^{\text{inter}}$	Maximum Density	$\rho^{\text{jam}} = \frac{1}{\ell_c + s_{\text{min}}^{\text{inter}}}$
Vehicle Length	ℓ_c		
Headway	$h_n = x_{n+1} - x_n$	Spacing	$s = \frac{1}{\rho}$

as probability densities in the position-velocity plane (e.g. those by [12]) have also been developed. This thesis will focus solely on traffic modeling with systems of PDE that are first order and quasilinear in time. Ultimately we would like to introduce a framework for incorporating stochastic driver variation into hyperbolic PDE traffic models. Other authors have also proposed approaches for doing so, including [10, 9, 8, 33, 42, 46]; the approach suggested here differs significantly in that it is the first approach (to the author’s knowledge) to be based on a mesh-independent numerical process in Eulerian coordinates.

The goal of this project was to model a broader range of phenomena than are possible without modeling driver inhomogeneity. First and foremost, the spontaneous growth and potential dissolution of congestion is by nature not a deterministic process, nor are these phenomena straightforward to simulate with existing models. A related phenomena difficult to capture with traditional models is capacity drop, the tendency for congestion to persist in a manner that manifests itself as a change to the fundamental diagram [31, 63]. The models in this thesis provide novel techniques for modeling spontaneous congestion and provide interesting paths forward in the modeling of other phenomena.

1.1 Lighthill Whitham and Richards (LWR)

The earliest macroscopic PDE models for traffic flow were derived from work on kinematic waves [48, 43]. Traffic modeling by nature relies heavily on assumptions about human behavior. The one fact that is known absolutely is that vehicles are not created or destroyed; this means the number of cars in some region may only change when cars leave that region to enter another or enter the present region from an adjacent region. The number of vehicles in the interval $(x, x + \Delta x)$ at time t is

$$\int_x^{x+\Delta x} \rho(y, t) dy. \quad (1.1)$$

The number of vehicles to move past a point in space x from time t to time $t + \Delta t$ is

$$\int_t^{t+\Delta t} \rho(x, t')v(x, t') dt'. \quad (1.2)$$

The quantity ρv is called flux. It follows from conservation of mass

$$\begin{aligned} \underbrace{\int_x^{x+\Delta x} \rho(y, t + \Delta t) dy}_{\text{cars later}} - \underbrace{\int_x^{x+\Delta x} \rho(y, t) dy}_{\text{cars now}} \\ = \underbrace{\int_t^{t+\Delta t} \rho(x, t')v(x, t') dt'}_{\text{cars in}} - \underbrace{\int_t^{t+\Delta t} \rho(x + \Delta x, t')v(x + \Delta x, t') dt'}_{\text{cars out}}. \end{aligned} \quad (1.3)$$

When the solution is smooth, the fundamental theorem of calculus may be used to obtain

$$\int_x^{x+\Delta x} \int_t^{t+\Delta t} \left(\frac{\partial}{\partial t} \rho + \frac{\partial}{\partial x} (\rho v) \right) dt' dy = 0. \quad (1.4)$$

It follows

$$\frac{\partial}{\partial t}\rho + \frac{\partial}{\partial x}(\rho v) = 0. \tag{1.5}$$

The collection of smooth and non-smooth solutions to Equation 1.5 are called ‘weak solutions’. Though this notion is vital to the work done in this thesis, the required background can be found in a variety of reference material, e.g. [13]. To close the model we need to define velocity. The simplest approach is to choose velocity as a function of density; the resulting function

$$v = V(\rho) \tag{1.6}$$

is called the *fundamental diagram*, and is ubiquitous in traffic modeling. Discussion of the fundamental diagram can be found in Section 1.2. The resulting traffic model is called the Lighthill, Whitham, and Richards (LWR) [43, 54] model

$$\rho_t + (\rho V(\rho))_x = 0. \tag{1.7}$$

In Chapter III we will modify Equation 1.7 by introducing an additional, small variable z and instead closing Equation 1.5 by specifying a function

$$v = V(\rho, z). \tag{1.8}$$

Both LWR and LWR augmented with auxiliary equations will be referred to as *equilibrium* models. Another way to close Equation 1.5 is to provide a PDE describing the dynamics of velocity; this approach will be discussed in Chapter IV and extended in Chapter V.

Theoretical tools for analyzing scalar conservation laws like Equation 1.7 [13, 57] as well as numerical methods for approximating solutions [39, 40] are widely available. We will briefly summarize properties of Equation 1.7 as they relate to traffic flow and utilize numerical methods for approximating solutions to interrogate our stochastic modifications.

While solutions remain smooth, Equation 1.7 can be solved using the method of charac-

teristics. If we consider the solution $\rho(c(t), t)$ along curves $c(t)$ we compute

$$\frac{d}{dt}\rho(c(t), t) = \rho_t(c(t), t) + c'(t)\rho_x(c(t), t)$$

and observe that ρ is constant along these curves (i.e. $\frac{d}{dt}\rho(c(t), t) = 0$) if we choose

$$c'(t) = V(\rho(c(t), t)) + \rho(c(t), t)V'(\rho(c(t), t)). \quad (1.9)$$

$\lambda(\rho(c(t), t)) = c'(t)$ is called the characteristic speed. These smooth transients are called ‘simple’ or ‘rarefaction’ waves. It is reasonable to assume that traffic velocity does not increase when density increases. Under this assumption

$$\lambda = V(\rho) + \rho V_\rho(\rho) \leq V(\rho) \quad (1.10)$$

so these disturbances may not move forward faster than the speed of traffic. The notion that information should not travel faster than the speed of traffic is a widely accepted principle of traffic dynamics [11, 2].

Equation 1.7 also admits discontinuous solutions moving at speed \mathfrak{s} satisfying the Rankine-Hugoniot condition

$$\rho_R V(\rho_R) - \rho_L V(\rho_L) = \mathfrak{s}(\rho_R - \rho_L). \quad (1.11)$$

These discontinuous solutions are called shock waves. Because in general discontinuities develop in finite time from smooth initial data, these discontinuous solutions must be allowed. Rapid deceleration observed when driving has a shock-like character, providing an interpretation of these discontinuities. However, allowing both rarefaction waves and shock waves leads to solutions that are not unique. Solutions from this set are called *weak solutions*. There are a variety of ways to choose a single solution to resolve this ambiguity. One

approach is to introduce a small viscous regularization

$$\rho_t + (\rho V(\rho))_x = \epsilon \rho_{xx} \tag{1.12}$$

and take $\epsilon \rightarrow 0^+$; these are called vanishing viscosity solutions. Another is to introduce an entropy condition like that of Lax

$$\lambda(\rho_L) > \mathfrak{s} > \lambda(\rho_R) \tag{1.13}$$

requiring that characteristics may go into but not emerge from shock waves [39]. A third is to prescribe dynamics for entropy, a quantity that is conserved in smooth solutions but decreases at discontinuities. Under the proper conditions this guarantees unique solutions as well.

The case of traffic flow is complicated by a variety of factors. Riemann problems for scalar conservation laws with flux functions that are either strictly concave or strictly convex consist of either one rarefaction wave or one shock wave, whereas in the general case more complex wave structures are possible. For traffic systems the flux functions in question are, if anything, concave. However, we will use the terms interchangeably to mean strictly concave or strictly convex. The flux function $f(\rho) = \rho V(\rho)$ is, in general, not convex. Moreover, some fundamental diagrams approximating real data are not convex (e.g. [58]). It should also be noted that most fundamental diagrams are bounded below by zero. Though an otherwise concave flux that is truncated at zero is not, strictly speaking, concave, in most cases densities greater than the first at which velocity is zero are unattainable. The truncation at zero velocity does however matter in some perturbed cases. This theoretical consideration is also important numerically, as we must ensure our numerical Riemann solver is robust enough to create these structures when required.

Second, the vanishing viscosity solution implies some amount of isotropy [40]. LeVeque [40] proposes a resolution to this problem based on the conditions for wave speeds in

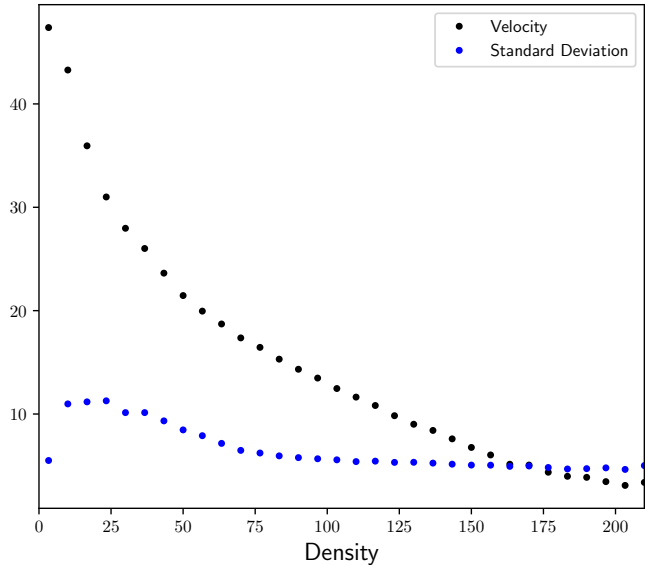


Figure 1.2: Mean density-velocity relationship and standard deviation computed from the NGSIM [50] data. This data does not provide accurate velocities at low densities.

traffic flow, requiring that

$$s \leq V(\rho_R) \tag{1.14}$$

holds across shocks, or equivalently

$$V(\rho_L) \geq V(\rho_R). \tag{1.15}$$

If we accept Leveque’s assertion that Equation 1.15 is sufficient to select a unique solution, then we can resolve both our problem with information propagation speed and our problem with uniqueness with a single condition.

1.2 The Fundamental Diagram

Determining accurate fundamental diagrams is a difficult problem in traffic modeling for a variety of reasons. First and foremost, most of the data available comes from inductive loop sensors. These sensors determine when a point on the road is or is not covered by

a vehicle. These sensors are often paired to yield accurate velocity information [63]. In principle, such a sensor pairing allows for estimation of both velocity and vehicle length at each vehicle crossing [63]. However, accurately determining spatial averages from complex time series data is a challenging problem. Even if we assume perfect data at sensor locations, the fundamental diagram varies by time of day, driver, and is likely unique to that portion of the road itself. This is true independent of density fluctuations. The difference between day and night even at similar densities is well documented (e.g. [63]). The goal of this work is to account for driver variation in a certain class of models. A qualitative picture of what a fundamental diagram parameterized by driver behavior should look like is required, but accurately matching models to data is not the focus of this work. For a matching of parameterized fundamental diagrams to data, see [14].

The fundamental diagram provides an average traffic velocity at each density. It has been observed [65, 42, 51] that the variance in velocity is density dependent. This can also be seen in the Next Generation SIMulation (NGSIM) data provided by the US Department of Transportation [50] (Figure 1.2). For the modeling in the remainder of this thesis we will need a prototype fundamental diagram that yields a function mapping from a ‘behavior parameter’ to an equilibrium velocity at each density (i.e. a function $V : \mathbb{R}^2 \rightarrow \mathbb{R}$). In this chapter we will review commonly used fundamental diagrams (Section 1.2.1) and present prototype fundamental diagrams that vary with an additional parameter (Section 1.2.2 and Section 1.2.3). As a convenience, we will sometimes write $V(\rho) = V(\rho, 0)$.

1.2.1 Classic Fundamental Diagrams

A variety of prototype relationships have been proposed for the fundamental diagram. The earliest is the linear relationship proposed by Greenshields [22]

$$V^{GS}(\rho) = v_{\max} \left(1 - \frac{\rho}{\rho^{\text{jam}}} \right). \quad (1.16)$$

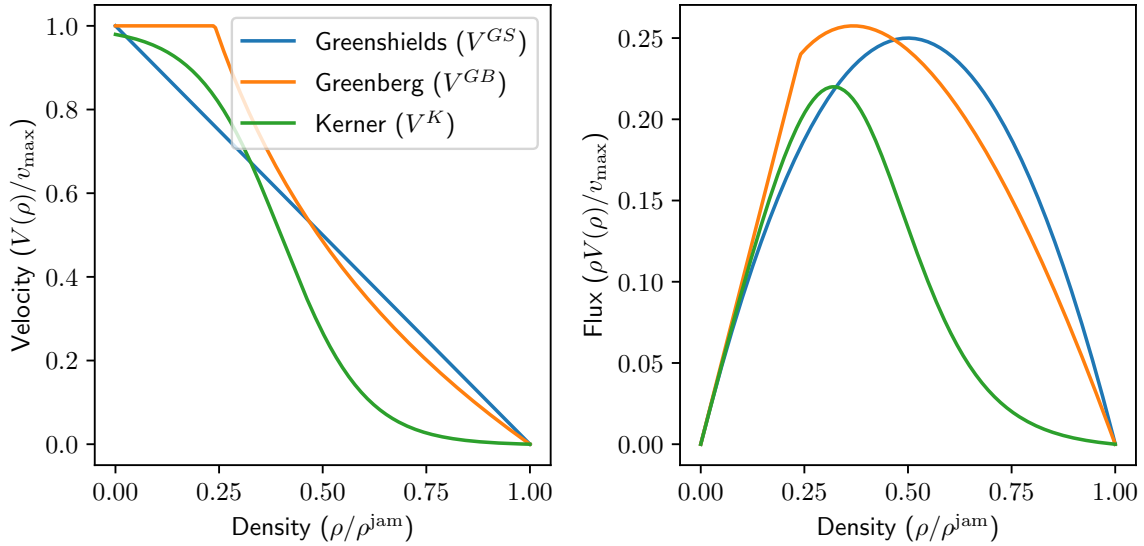


Figure 1.3: A selection of well known fundamental diagrams (Equations 1.16 through 1.18).

Another early fundamental diagram was proposed by Greenberg [21]

$$V(\rho) = c \log \left(\frac{\rho^{\text{jam}}}{\rho} \right).$$

A simple modification to obtain a more reasonable bounded version of Greenberg's fundamental diagram is to take

$$V^{GB}(\rho) = \min \left(v_{\max}, c \log \left(\frac{\rho^{\text{jam}}}{\rho} \right) \right) \quad (1.17)$$

instead. A later influential fundamental diagram used by Kerner [30] is of the form

$$V^K(\rho) = v_{\max} \left(\left(1 + \exp \left(\frac{\frac{\rho}{\rho^{\text{jam}}} - c}{w} \right) \right)^{-1} - k \right) \quad (1.18)$$

where parameters are chosen such that $V^K(\rho^{\text{jam}}) = 0$. A depiction of these fundamental diagrams and corresponding flux functions can be found in Figure 1.3.

There are several reasonable conditions that may be put on the fundamental diagram.

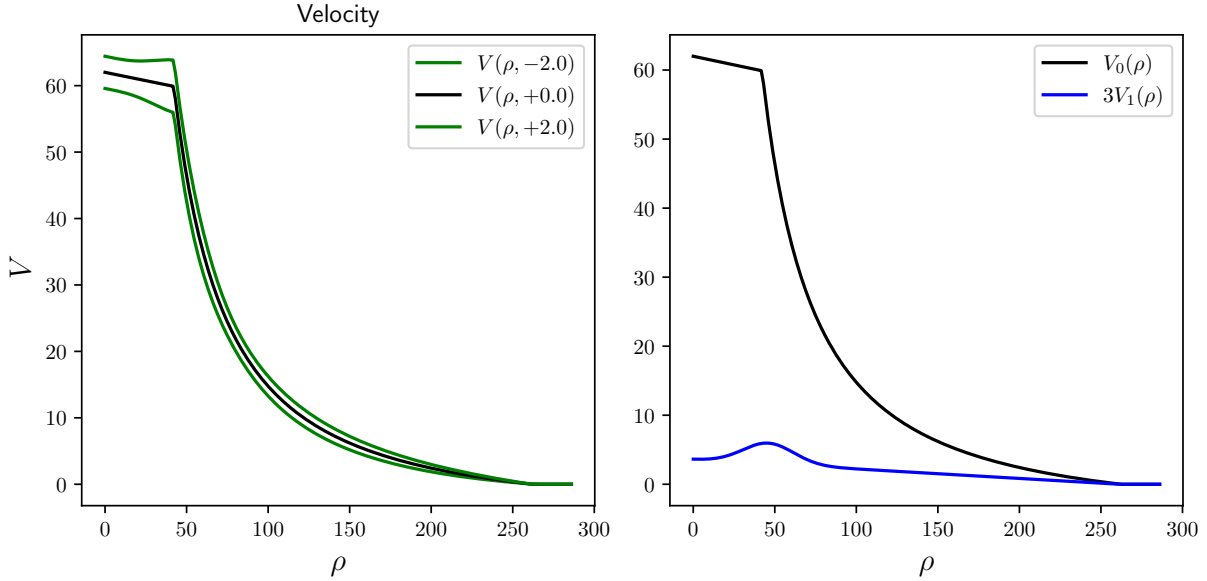


Figure 1.4: The ‘linearized’ fundamental diagram $V^{LF}(\rho, z) = V_0^{LF}(\rho) + zV_1^{LF}(\rho)$ plotted with parameters shown in Table 1.2.

Perhaps the most obvious is that the fundamental diagram should be positive, bounded, and non-increasing, i.e.

$$0 \leq V(\rho + \epsilon) \leq V(\rho) \leq v_{\max} \quad (1.19)$$

for all ρ and $\epsilon > 0$. As previously mentioned, a convex flux is also desirable and equivalent to the condition that

$$2V_\rho(\rho) + \rho V_{\rho\rho}(\rho) \leq 0 \quad (1.20)$$

for all ρ . Though convexity simplifies many mathematical aspects of the scalar conservation law, there is no real-world reason to expect traffic flux to be convex. Further, it is difficult to build fundamental diagrams that agree with data and meet this requirement; indeed some data driven fundamental diagrams (e.g. [58]) do not. We will not require that fundamental diagrams yield convex fluxes.

Table 1.2: Parameters used in the linearized fundamental diagram (Equation 1.21).

Free Flow		Congested Flow		Deviation	
v_{\max}	63.0	a	10607.41	h	5.8
s_f	0.06	p	1.36	c	50.0
		k	5.45	w	22.0
				b	3.2
				j	260.0

1.2.2 A Linearized Fundamental Diagram

Recall that we ultimately need to define a prototype family of fundamental diagrams that yields an equilibrium velocity for each pair consisting of a density and a driver dependent parameter (ρ, z) . Often only the standard deviation of velocity is available or easily computed from published traffic data, and for this reason it is convenient to identify this parameter with the standard deviation of velocity at a particular density. This identification is a convenient proxy for driver variation, but it does not solely represent driver variation. Because we have not established a well-understood meaning of the deviation parameter consistent with the models presented in Chapters III and V, this decision is arbitrary. It should also be emphasized that, while convenient for crafting prototype fundamental diagrams, we cannot justify this identification quantitatively.

For simplicity we will define a fundamental diagram (Figure 1.4) that is linear in z and has the qualitative features of the deviations shown in [42, 51]. It may be possible to extract parameterized families of fundamental diagrams from data but the far simpler linearized

fundamental diagram $V^{LF}(\rho, z)$ will be used throughout most of this work. We define

$$V^{LF}(\rho, z) = V_0^{LF}(\rho) + zV_1^{LF}(\rho) \quad (1.21)$$

$$V_0^{LF}(\rho) = \min \left(v_{\max} - f_s \rho, \max \left(\frac{a}{\rho^p} - k, 0 \right) \right) \quad (1.21a)$$

$$V_1^{LF}(\rho) = \max \left(h \exp \left(- \left(\frac{\rho - c}{w} \right)^2 \right) + b \left(1 - \frac{\rho}{j} \right), 0 \right) \quad (1.21b)$$

where $p > 1$ and v_{\max} , f_s , a , k , h , c , w , b , j are positive constants. Adopting this form of the fundamental diagram simplifies some computations as we can directly and explicitly relate the deviation parameter z to the actual velocity $V^{LF}(\rho, z)$ at any fixed density ρ . The shape of V_1^{LF} is chosen to be reminiscent of the standard deviation in real data (see Figure 1.2 as well as [42, 51]), but there is no reason to expect that deviations in behavior are proportional to these values. Behavior variation is a part of the cause of deviations from the mean, but not the entirety of it. It is impossible to collect ‘equilibrium’ traffic data; any variance in the data collected reflects velocity differences in driver behavior and differences due to traffic dynamics. The ‘ z ’ parameter introduced here does not have a physical interpretation that can be easily identified with the magnitude of the standard deviation in any sense.

However, in equilibrium models, structuring the fundamental diagram in this way does produce more variation in the density regimes where it is expected, even if not for the right reasons. An additional comment on the variations in traffic dynamics due to the influence of z in the fundamental diagram and variations due to non-equilibrium phenomena will be made in Section 3.4. An alternative justification is that deviations at these density regimes can be explained by deviations in parameters like intended time headway or tolerance for speeding. These deviations produce a fundamental diagram (Section 1.2.3) with larger variation in the same regimes, thus providing a potential partial explanation, but the linearized form is simpler. The largest disadvantage to a linearized fundamental diagram is the loss of monotonicity for large values of z . We will aim to stay away from regimes in which mono-

tonicity is lost, but due to the nature of the processes discussed in Chapter II this cannot be guaranteed.

1.2.3 An Idealized Fundamental Diagram

The quest for a more accurate fundamental diagram requires making a multitude of decisions, but also provides several interesting opportunities to introduce uncertainty in a sensible way. Drivers are typically told to obey three constraints:

1. do not exceed the speed limit,
2. maintain a given time between the front bumper of a car and the back bumper of the leading car, and
3. do not collide with the driver in front.

We will measure this time from front bumper to back bumper (i.e. the time to traverse the intervehicle spacing) rather than the ‘time headway’ as it is often defined in traffic flow. This is not only (arguably) more true to what drivers measure, but also has the advantage of producing a velocity of zero at high enough densities. The first of these is easily satisfied by requiring

$$v \leq v_{\max}. \tag{1.22}$$

The second and third are satisfied by requiring

$$\underbrace{\frac{1}{v} \left(\frac{1}{\rho} - \frac{1}{\rho^{\text{jam}}} \right)}_{\text{time to leading vehicle}} \geq t_{\min}^i \iff v \leq \frac{1}{t_{\min}^i} \left(\frac{1}{\rho} - \frac{1}{\rho^{\text{jam}}} \right). \tag{1.23}$$

This also ensures it always takes a finite time to reach the back bumper of the leading vehicle. We can then make small modifications to adapt this to what real data is known to look like (e.g. [58]). We introduce a small slope f_s in the free part (Equation 1.22) and a general power p in the congested part (Equation 1.23). If it is assumed driver variation appears in the the

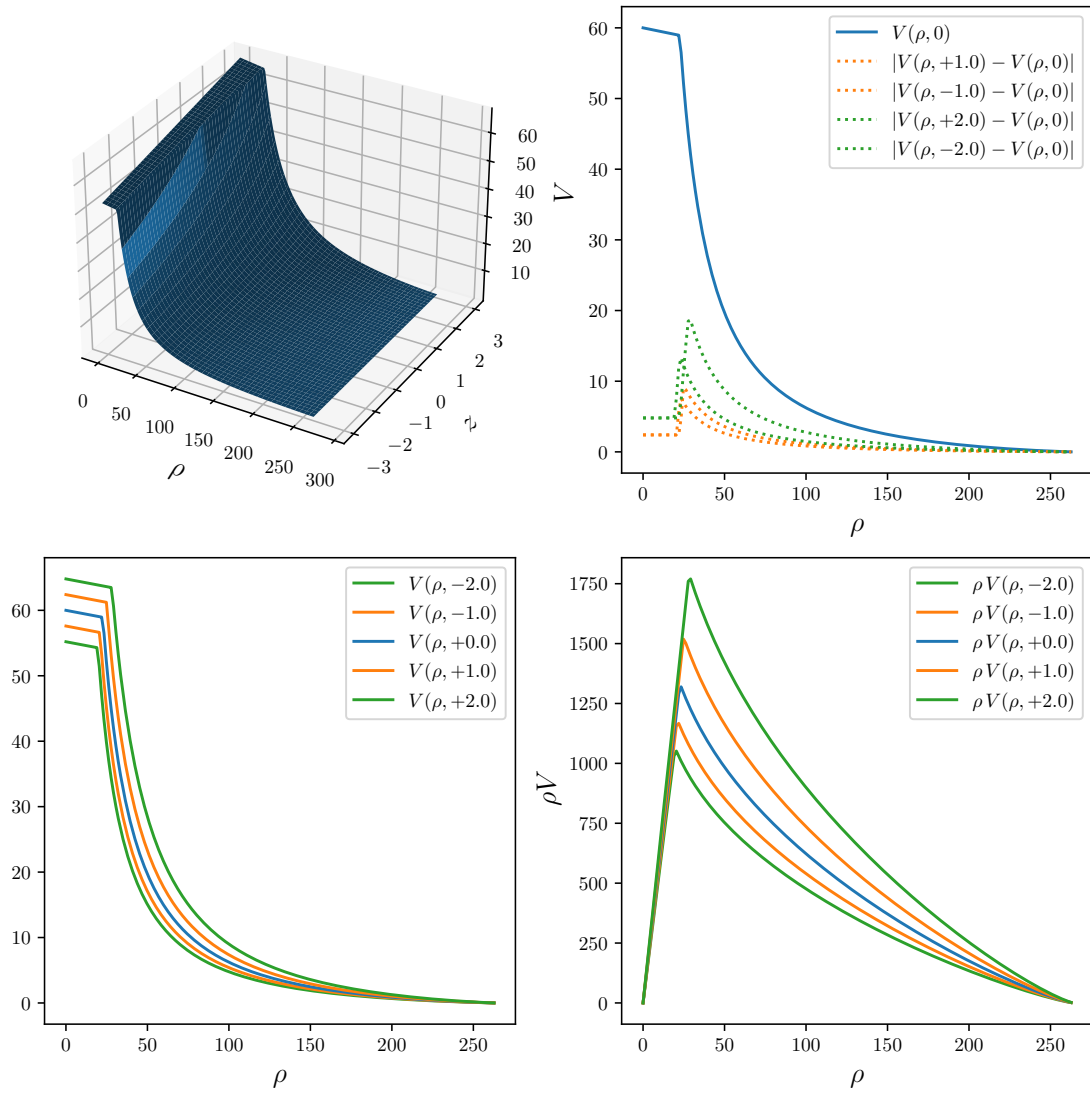


Figure 1.5: A new fundamental diagram with dependence upon a deviation parameter z .

desired maximum velocity and the desired time between vehicles, a resulting fundamental diagram, illustrated in Figure 1.5, is

$$V^p(\rho, z) = \max \left(\min \left(v_{\max} - f_s \rho + v_{\max}^{\text{dev}} z, \frac{1}{(t_{\min}^i - \gamma z)} \left(\frac{1}{\rho} - \frac{1}{\rho^{\text{jam}}} \right)^p \right), 0 \right). \quad (1.24)$$

1.3 Traffic Experiments

It is useful to consider a handful of test cases or ‘experiments’ that reveal the behavior of these traffic models in common scenarios, including cases designed to demonstrate the behavior we expect the proposed stochastic models to exhibit. The simplest and most well known test case in traffic modeling is what we will call the ‘ringroad experiment’ (Section 1.3.1). This is of particular relevance to us because it has been shown experimentally [60] that large ‘stop and go’ structures spontaneously arise from initial uniformity; this is precisely the type of phenomenon we would hope to observe with stochastic driver variation. We will also consider a case in which the speed limit decreases (Section 1.3.2). Because we aim to develop new models capable replicating traffic phenomena, we will focus on qualitative features rather than quantitative comparison to data or parameter estimation.

We will primarily visualize the results of these traffic experiments through macroscopic fields (e.g. density and velocity) and vehicle trajectories, i.e. curves $x_k(t)$ such that $\dot{x}_k(t) = v(x_k(t), t)$. Vehicle trajectories are always a representation of the velocity field and relative changes in density (they are streamlines), but they may or may not be an accurate representation of true density or vehicle spacing. In the context of traffic flow, vehicle trajectories have the added benefit of corresponding to probe data, allowing for qualitative comparison to phenomena seen in the literature.

1.3.1 The Ringroad Experiment

It is well known that congested patterns arise spontaneously from uniform or nearly uniform flow. This is often observed as ‘phantom jams’ on the highway. A simple test case that

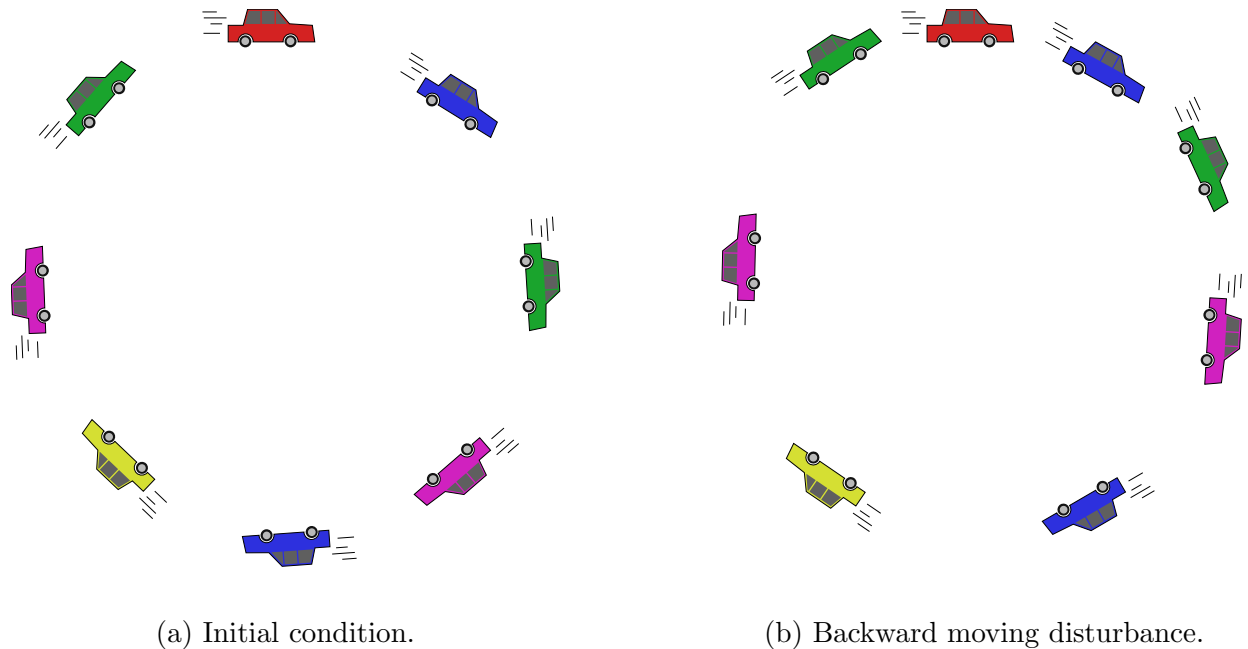


Figure 1.6: Illustration of the ringroad experiment initial condition (a) and the congested pattern that evolves (b).

exhibits this phenomenon (at a lower velocity) is the ‘ringroad’ experiment, a controlled version of which was conducted by Sugiyama et al [60]. In the experiment, drivers are spaced uniformly along a circular road (Figure 1.6a) and asked to follow the driver in front at a speed of approximately 30 kilometers per hour (18 miles per hour). After a short period of time a stop-and-go pattern develops (Figure 1.6b). There is disagreement about the precise mechanism for this. Particular authors (e.g. Kerner [31, 29] and Trieber [63, 64]) have worked extensively to develop a ‘physics’ of traffic flow with the aim of classifying traffic states (called ‘phases’) and transitions between them. However, the causes for congestion without bottlenecks are not agreed upon. As with most experiments, it is extremely difficult to find quantitative agreement between models and experiment. For quantitative agreement in models similar in spirit to the models in this thesis without stochastic terms, see Fan et al [14, 14]. For equilibrium models obtaining quantitative agreement would require obtaining appropriate fundamental diagrams; doing so is one of the core problems of traffic modeling. Estimating fundamental diagrams is extremely difficult in general, but data is

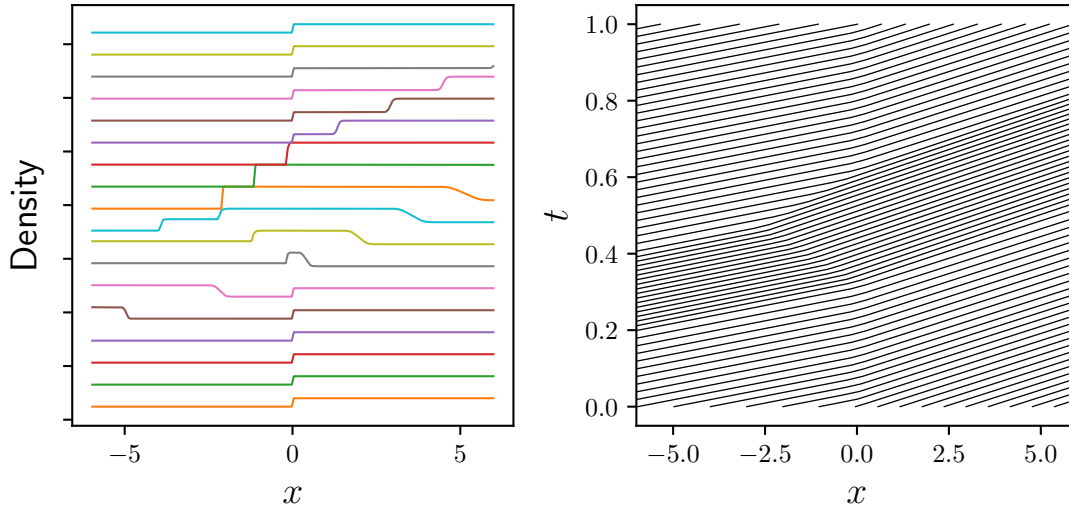


Figure 1.7: The speed drop experiment as realized by the LWR model (Equation 1.7) with the fundamental diagram presented in Section 1.2.2. The left plot contains density profiles at uniformly spaced times that increase as they go up the page. The right depicts vehicle trajectories spaced proportional to traffic density.

especially scarce in the low velocity regime, especially if one would like to isolate single-lane behavior. For this reason we will provide qualitative evidence that these models exhibit the proper phenomena and show dependence of these phenomena upon parameters and flow regime, but leave parameter fitting as a possible avenue for future work.

1.3.2 The Speed Drop Experiment

Another case we will consider is a decrease in speed limit resulting in an increase in density. For this experiment the fundamental diagram used must have an identifiable parameter representing the speed limit or maximum velocity that changes sharply at $x = 0$. In the case of LWR (Equation 1.7) the governing equation becomes

$$\rho_t + (\rho V(\rho, v_{\max}))_x = 0 \tag{1.25}$$

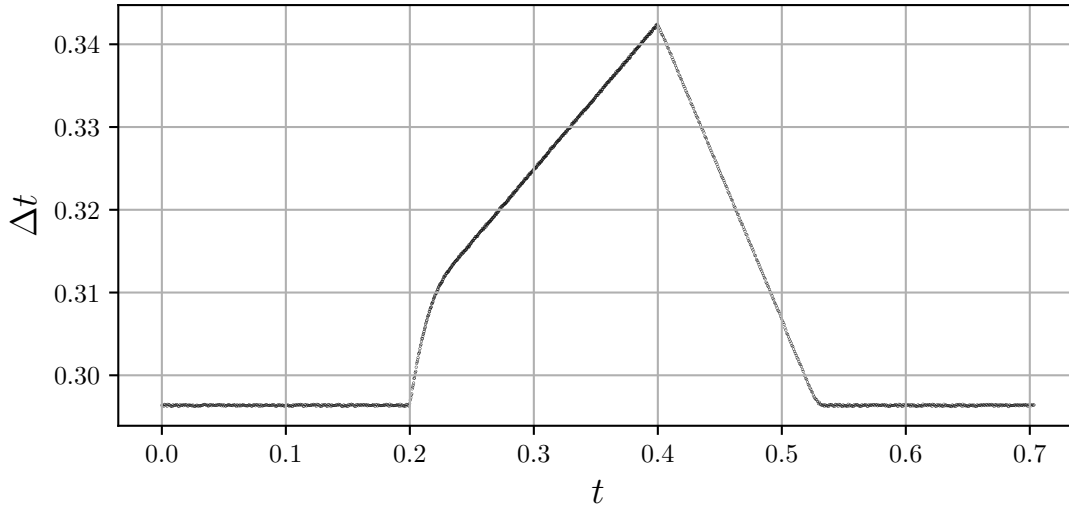


Figure 1.8: Transit time through the domain as a function of time corresponding to the vehicle trajectories shown in Figure 1.7.

where

$$v_{\max} = \begin{cases} v_{\max}^l & \text{if } x < 0 \\ v_{\max}^r & \text{if } x > 0 \end{cases}. \quad (1.26)$$

A thorough discussion of the Riemann problem with spatially varying flux can be found in [39, 41], among other places. Our speed drop experiment, depicted in Figure 1.7, consists of three time periods:

Steady State We initialize the domain with a density profile

$$\rho_0(x) = \begin{cases} \rho_0^l & \text{if } x < 0 \\ \rho_0^r & \text{if } x > 0 \end{cases} \quad (1.27)$$

where the constants ρ_0^l and ρ_0^r are a steady-state solution, i.e.

$$\rho_0^l V(\rho_0^l, v_{\max}^l) = \rho_0^r V(\rho_0^r, v_{\max}^r). \quad (1.28)$$

For this condition to be sufficient we also need the standing shock at this disconti-

nity to satisfy an entropy condition. It is established as a traffic principle that this *deceleration* results in a standing shock. Further, we require that

$$V(\rho_0^l, v_{\max}^l) + \rho_0^l \frac{\partial V}{\partial \rho}(\rho_0^l, v_{\max}^l) > 0 \quad (1.29)$$

so that the flow may be controlled from the inflow. For deterministic traffic models, the solution will be constant until the second period.

High Density Pulse At some later time, the inflow density doubles to $2\rho_0^l$. This produces a high density pulse through the domain. Upon reaching $x = 0$, part of this wave is transmitted and part is reflected.

Return to Steady State Before the reflected wave reaches the inlet, the inflow density is reverted to its original value ρ_0^l . For deterministic LWR models, flow conditions eventually revert to the initial profile.

(The word ‘phase’ may be more appropriate than the term ‘time period’, but the former has a different accepted meaning in traffic flow.) At each phase, there are several questions of interest:

Steady State For stochastic models, does stochasticity alone decrease flux such that backup is observed prior to introduction of the pulse? Does the point at which sharp deceleration occurs vary or does it stay precisely at $x = 0$?

High Density Pulse A high density pulse will, in general, result in increased travel time (see Figure 1.8). How does the severity of this increase depend on driver variation? How variable is this peak travel time under various models?

Return to Steady State How quickly does flow return to the initial steady state? Alternatively, does the flow return to the initial steady state at all? The failure of traffic flow to return to the steady state under these conditions is an example of the *capacity drop* phenomenon [63]; models for capacity drop are sought after in traffic modeling.

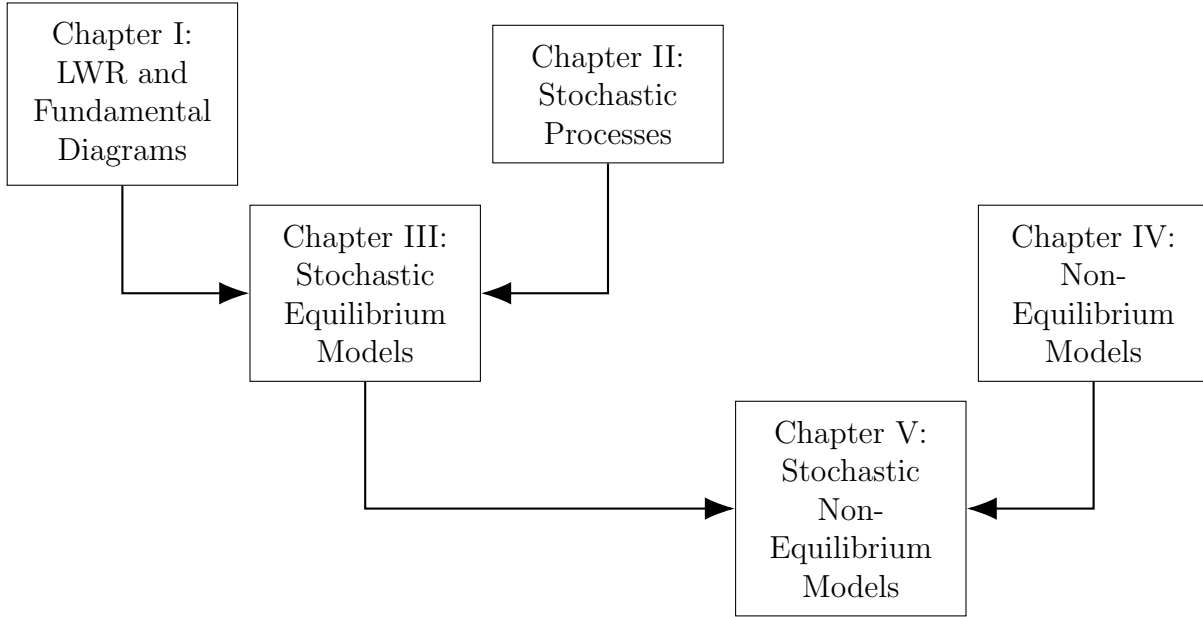


Figure 1.9: Chapter dependency chart.

1.4 Thesis Outline

The addition of driver-dependent parameters to macroscopic traffic models is a nascent field (see e.g. [33, 14, 49]). In this thesis a novel collection of models that aim to address some of the shortcomings are presented. We will

1. select a well-defined stochastic process that varies in space and time,
2. modify this process to better represent driver variation/noise, and finally
3. couple these stochastic processes to existing equilibrium (a.k.a. first order) traffic models and non-equilibrium (a.k.a. second order) traffic models.

While considering a random initial distribution of driver behaviors that are constant in time is an interesting area of research, it should be noted that stochastic variation in time only is insufficient. Varying the fundamental diagram stochastically in time but uniformly in space results in solutions that are identical to the nominal solution evaluated at a uncertain point in time. Though this is clear by a change of variables, this experiment was performed in [42].

These models exhibit a richer range of phenomena when compared to their deterministic counterparts, but are based on the same assumptions and subject to the same principles. In Chapter II we will give an overview of stochastic processes in one space dimension and one time dimension. In particular we will describe the stochastic heat equation as it exists outside of traffic models. Chapter III presents equilibrium traffic models (see Section 1.1) with a stochastic, driver-dependent parameter. Chapter IV summarizes non-equilibrium traffic models (i.e. those with velocity that evolves in time along with traffic density) and Chapter V will introduce a white noise source term to those models.

CHAPTER II

A Heat Equation with White Noise Forcing

There are several different generalizations of Brownian motion to multiple dimensions. Because there is not an underlying physical theory that provides a stochastic framework, we will consider a few possible random processes and select one that

1. varies in both space and time;
2. has well defined, continuous, and bounded solutions that,
3. when approximated numerically, have mesh-independent statistics, and
4. may be readily modified to incorporate different physical patterns, e.g. advection with the flow of traffic or boundary conditions.

‘Continuous’ and ‘bounded’ here should be preceded by ‘almost surely’, meaning that this is the case except for sets of measure zero in probability space. Because every statement in this chapter has this caveat and the goal of this chapter is to select a process to accomplish a practical purpose rather than prove properties of stochastic processes, we will omit the words ‘almost surely’ throughout.

2.1 Independent Processes in Each Cell

To motivate the need for this chapter, let us begin with a discussion of why adding noise naïvely does not produce a sensible random field. Begin with the (scalar) Ornstein-Uhlenbeck

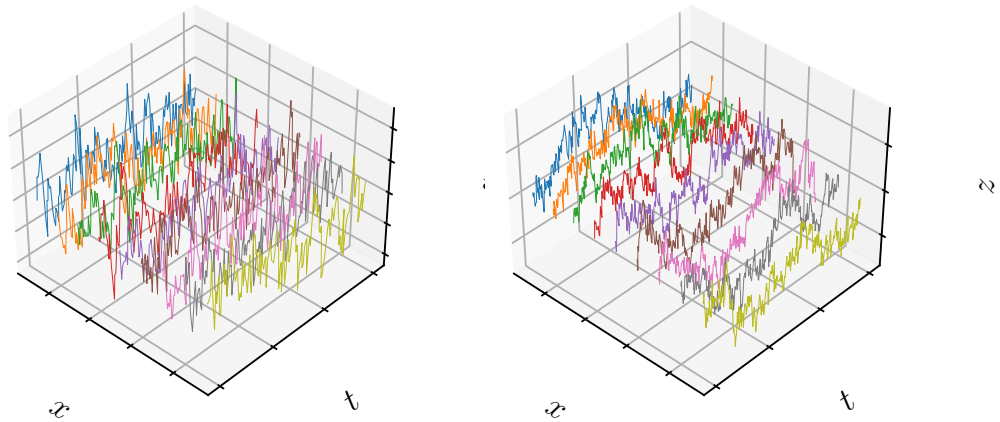


Figure 2.1: An illustration of several independent Ornstein-Uhlenbeck processes at a variety of points in space (left), contrasted to a set of stochastic processes correlated in space (right). The examples on the right are a representation of the process and parameters found in Section 2.2.

process

$$dz = -\frac{1}{\tau^z} dt + \eta dW, \quad (2.1)$$

i.e. a random increment dW with a reversion to the mean. A detailed analysis of this process can be found in several standard texts, e.g. [53]. Consider an approach in which we add a small random perturbation of this type in each computational cell. A simple first-order scheme that might result is

$$z_j^{n+1} = z_j^n - \frac{k}{\tau^z} z_j^n + \eta \sqrt{k} \xi_j^n \quad (2.2)$$

where ξ_j^n are independent and identically distributed (i.i.d.) variables. The result is an approximation of a different (independent) Ornstein-Uhlenbeck process in each spatial cell. Because there is no correlation from one computational cell to the next, we expect major changes (discontinuities) in our behavior variable from one cell to the next (see Figure 2.1).

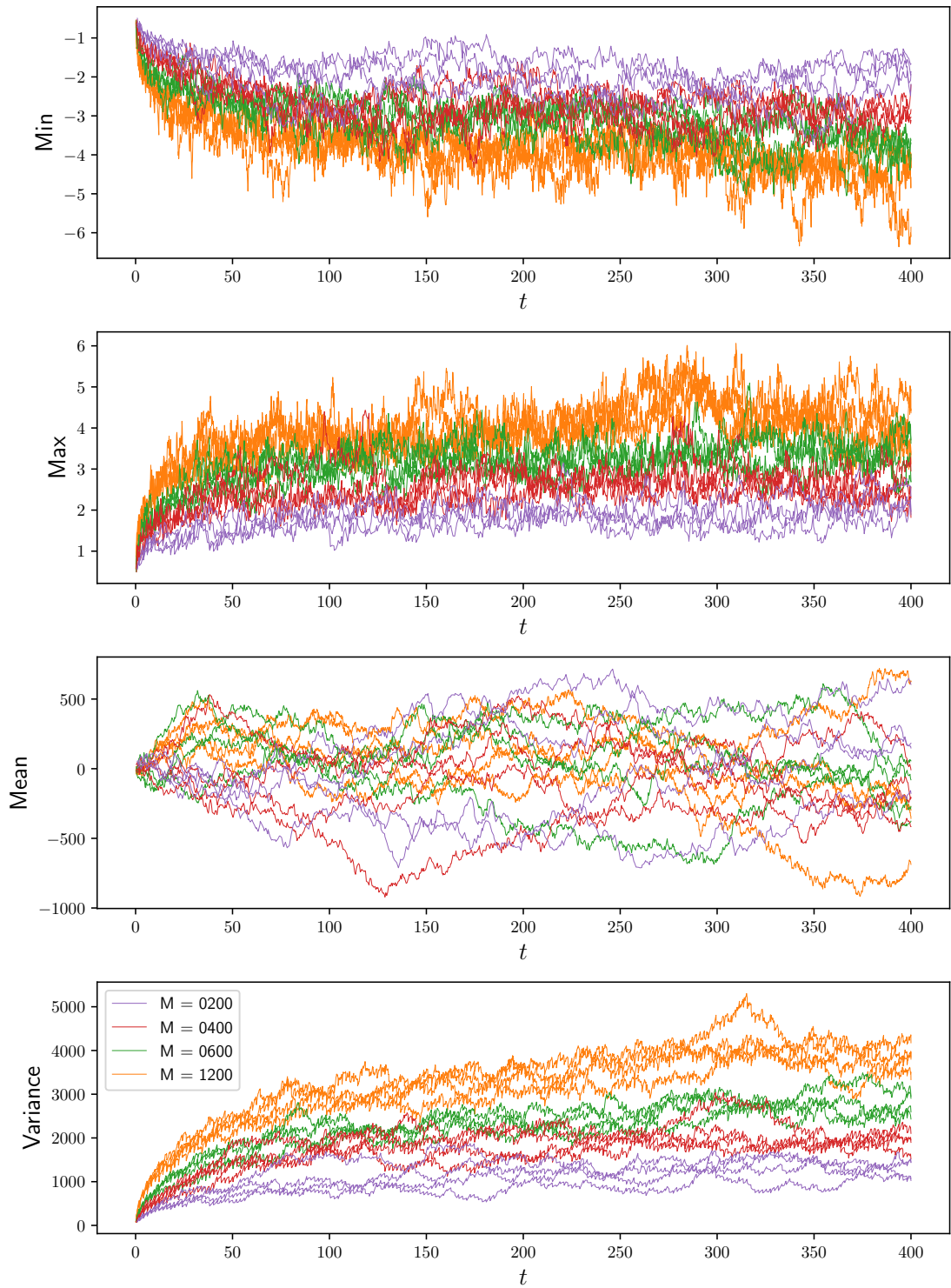


Figure 2.2: Characterization of a variety of solutions to Equation 2.3. Compare this Figure 2.6.

We could add an advective term to Equation 2.2 which might result in a discrete equation of the form

$$z_j^{n+1} = z_j^n + \frac{vk}{h} (z_j^n - z_{j-1}^n) - \frac{k}{\tau z} z_j^n + \eta\sqrt{k}\xi_j^n. \quad (2.3)$$

This results in what appear to be continuous realizations in space. At least in the case of constant velocity, these approximations are made continuous by numerical diffusion. We argue that any process we would like to use as a building block should at least make sense in the case of constant velocity. This is illustrated numerically in Figure 2.2.

One solution to this problem is to choose a discretization and work with the discrete model. Doing so draws a parallel between macroscopic PDE model and the resulting cellular models, but not one that is consistent under mesh refinement. The parameters in such models depend on cell size, and the model is no longer a discretization of a PDE. (Another approach that has been explored by the author but was ultimately discarded in favor of the present method was to evolve a traffic model atop a random topography generated by a Brownian sheet and similar processes.)

In the present work we will instead choose an underlying stochastic process that provides mesh-independent statistics, then couple it to existing macroscopic traffic models. The required regularization is ultimately achieved through a viscous term (Section 2.2). Throughout we will state well-known facts about the stochastic processes being discussed with references to texts on the subject but without proof; rigorous derivations of the processes discussed in this chapter are out of the scope of this thesis.

2.2 Stochastic Heat Equation

There are several modifications we might want to make to the process we choose to use. We would like to impose a variety of boundary conditions, advect the process with the flow of traffic, and make local changes to the process depending on local flow conditions. It is difficult to make these modifications to many other stochastic processes. The process described in

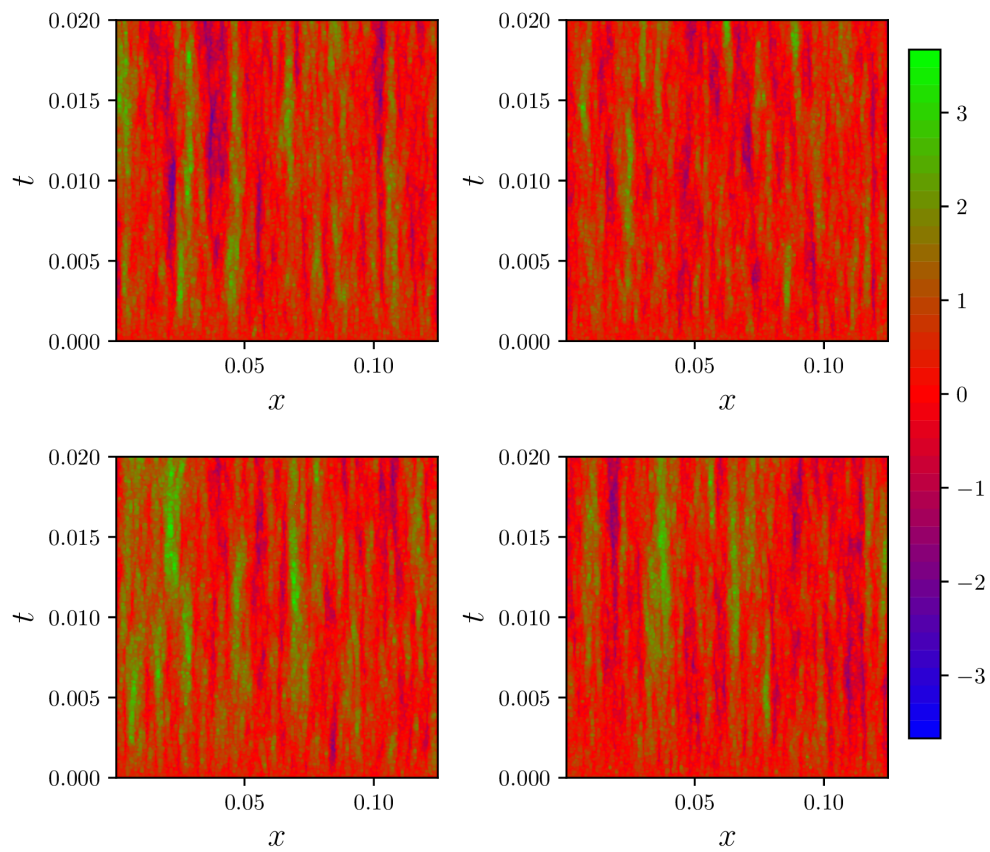
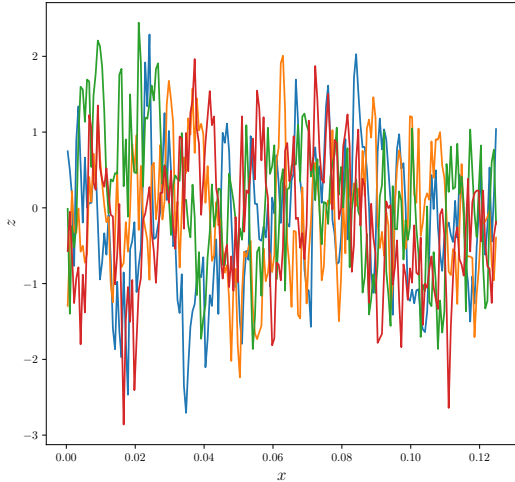
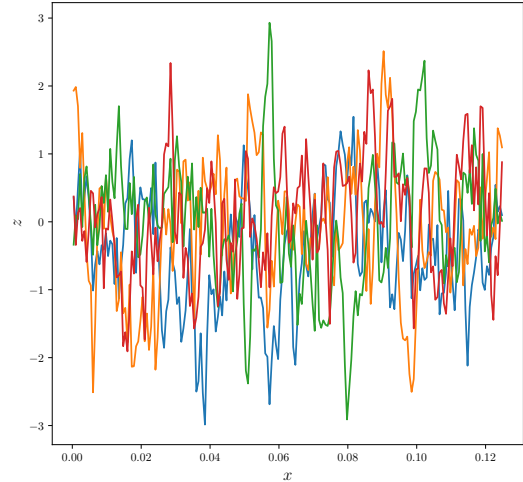


Figure 2.3: Four independent example realizations of z (Equation 2.4) using $\eta = 5.7742 \times 10^{-1}$, $\kappa = 2.4522 \times 10^{-4}$, and $\tau^z = 3.5294 \times 10^{-2}$. The domain is approximated by 800 cells.



(a) without advection



(b) with advection at a constant velocity $v = 5.0$

Figure 2.4: Example realizations of the stochastic heat equation with and without advection using $\eta = 5.7742 \times 10^{-1}$, $\kappa = 2.4522 \times 10^{-4}$, and $\tau^z = 3.5294 \times 10^{-2}$. overlaid at $t = 0.02$. The domain is approximated by 800 cells.

this section is a local description of a stochastic process and boundary conditions for it may be specified in the language of the PDE models we will couple it with. Additionally, modifications to traffic models using this approach (Equation 2.16) yield models that closely mirror other models involving transported traffic properties (e.g. [33, 14]) when the white noise and diffusion terms are neglected. An alternative way to justify this approach is to argue that the approach discussed at the beginning of this chapter is made sensible with the inclusion of a regularizing diffusive term.

We will begin by discussing general properties of the stochastic heat equation. This equation will serve as a ‘building block’ for the addition of white noise to the LWR model in Section 3.3. Consider

$$z_t = \kappa z_{xx} + \eta \xi - \frac{z}{\tau^z} \quad (2.4)$$

where κ , η , and τ^z are constants and ξ is a Gaussian white noise process such that

$$\mathbb{E} \iint_V \xi dx dt = 0 \tag{2.5}$$

$$\mathbb{E} \iint_V \xi^2 dx dt = m(V) \tag{2.6}$$

where $m(V)$ is the measure of the set $V \subset \{(x, t)\}$. Here we will ascribe units to the measure of a set in space-time (so $m(V)$ has units of length-time). It follows

$$\mathbb{E}[\xi(x, t)\xi(y, s)] = \delta(x - y)\delta(t - s). \tag{2.7}$$

As in previous parts of this chapter, our goal is to utilize this underlying process for traffic modeling; we will cite some necessary facts to justify its use without giving proof. Moreover, the treatment here will be less rigorous in the interest of brevity and clarity; a rigorous treatment can be found in [32] or [23].

Solutions to Equation 2.4 (almost surely) have continuous versions, and are (almost surely) bounded in $L^2(\mathbb{R} \times \mathbb{R}^+)$ [32]. Four independent realizations showing qualitative behavior of solutions can be found in Figure 2.3. Note that the time and length scales have been chosen to be markedly different, and each realization shows similar qualitative behavior. In these processes we also are seeking regions of markedly different behavior and a clear difference in magnitude with respect to space and time, both of which are present.

2.3 Parameters

To utilize this process in the models to follow we need some understanding of the characteristic length and time scales over which z changes. What follows is an extension of a

formal calculation proposed in [23]. We begin with

$$\begin{aligned} z_t &= \kappa z_{xx} - \frac{z}{\tau^z} + f \\ z(x, 0) &= g(x) \end{aligned} \tag{2.8}$$

The fundamental solution to Equation 2.8 is

$$\Phi(x, t) = \frac{1}{\sqrt{4\pi t \kappa}} \exp\left(-\frac{x^2}{4t\kappa} - \frac{t}{\tau^z}\right). \tag{2.9}$$

By ‘fundamental solution’ we mean

$$z(x, t) = \int_0^t \int_{\mathbb{R}} \Phi(x - y, t - s) f(y, s) dy ds + \int_{\mathbb{R}} \Phi(x - y, 0) g(y) dy \tag{2.10}$$

solves Equation 2.8 in \mathbb{R}^2 .

We then set $f = \eta\xi$ where ξ is a Gaussian white noise as described above. Without loss of generality ($\mathbb{E}[z(x, t)z(y, t')] = \mathbb{E}[z(x - y, t)z(0, t')]$), we compute

$$\begin{aligned} \mathbb{E}[z(x, t)z(0, t')] &= \mathbb{E}\left(\int_0^t \int_{\mathbb{R}} \Phi(x - y, t - s) \eta \xi(y, s) dy ds\right) \left(\int_0^{t'} \int_{\mathbb{R}} \Phi(-y', t' - s') \eta \xi(y', s') dy' ds'\right) \\ &= \mathbb{E} \int_0^t \int_0^{t'} \int_{\mathbb{R}} \int_{\mathbb{R}} \frac{\eta^2 \xi(y, s) \xi(y', s')}{4\pi\kappa\sqrt{(t-s)(t'-s')}} \exp\left(-\frac{(x-y)^2}{4\kappa(t-s)} - \frac{(y')^2}{4\kappa(t'-s')} \right. \\ &\quad \left. - \frac{t-s+t'-s'}{\tau^z}\right) dy dy' ds' ds \\ &= \eta^2 \int_0^{\min(t, t')} \int_{\mathbb{R}} \frac{1}{4\pi\kappa\sqrt{(t-s)(t'-s')}} \exp\left(-\frac{(x-y)^2}{t\kappa(t-s)} - \frac{y^2}{4\kappa(t'-s)} - \frac{t+t'-2s}{\tau^z}\right) dy ds \\ &= \eta^2 \int_0^{\min(t, t')} \frac{1}{\sqrt{4\pi\kappa(t+t'-2s)}} \exp\left(-\frac{x^2}{4\kappa(t+t'-2s)} - \frac{t+t'-2s}{\tau^z}\right) ds. \end{aligned}$$

The quantities of interest for us are a characterization of the covariance in space

$$\sigma_{xy}^2 = \lim_{t \rightarrow \infty} \mathbb{E}z(x, t)z(y, t) \tag{2.11}$$

and a characterization of the covariance in time

$$\sigma_{t\delta}^2 = \lim_{t \rightarrow \infty} \mathbb{E}z(x, t)z(x, t + \delta). \quad (2.12)$$

First addressing variance in the spatial variable x , we continue from above making the substitution $y = \frac{x^2}{8\kappa(t-s)}$:

$$\begin{aligned} \mathbb{E}z(x, t)z(0, t) &= \frac{\eta^2}{\sqrt{8\pi\kappa}} \int_0^t \frac{1}{\sqrt{t-s}} \exp\left(-\frac{x^2}{8\kappa(t-s)} - \frac{2(t-s)}{\tau^z}\right) ds \\ &= \frac{\eta^2}{\sqrt{8\pi\kappa}} \int_{\frac{x^2}{8\kappa t}}^{\infty} \frac{x^2}{8\kappa y^2} \sqrt{\frac{8\kappa y}{x^2}} \exp\left(-y - \frac{2x^2}{8\tau^z \kappa y}\right) dy \\ &= \frac{\eta^2 |x|}{8\kappa \sqrt{\pi}} \int_{\frac{x^2}{8\kappa t}}^{\infty} y^{-\frac{3}{2}} \exp\left(-y - \frac{x^2}{4\tau^z \kappa y}\right) dy. \end{aligned}$$

We can then use a symbolic computational tool to evaluate

$$\begin{aligned} \int_c^{\infty} y^{-\frac{3}{2}} \exp\left(-y - \frac{a}{y}\right) dy &= \sqrt{\frac{\pi}{4a}} \left(e^{-2\sqrt{a}} \left(\operatorname{erf}\left(\frac{\sqrt{a}-c}{\sqrt{c}}\right) + 1 \right) \right. \\ &\quad \left. + e^{+2\sqrt{a}} \left(\operatorname{erf}\left(\frac{\sqrt{a}+c}{\sqrt{c}}\right) - 1 \right) \right) \end{aligned}$$

and obtain

$$\lim_{t \rightarrow \infty} \mathbb{E}z(x, t)z(0, t) = \lim_{t \rightarrow \infty} \frac{\eta^2}{4} \sqrt{\frac{\tau^z}{\kappa}} \exp\left(-\frac{|x|}{\sqrt{\kappa\tau^z}}\right).$$

For general x and y we have

$$\lim_{t \rightarrow \infty} \mathbb{E}z(x, t)z(y, t) = \frac{\eta^2}{4} \sqrt{\frac{\tau^z}{\kappa}} \exp\left(-\frac{1}{\sqrt{\tau^z \kappa}} |x - y|\right). \quad (2.13)$$

For time, assume without loss of generality $\delta > 0$ and compute (immediately using the

substitution $y = (\tau^z)^{-1}(\delta + 2(t - s))$)

$$\begin{aligned}
\mathbb{E}z(0, t)z(0, t + \delta) &= \eta^2 \int_0^t \frac{1}{\sqrt{4\pi\kappa(\delta + 2(t - s))}} \exp\left(-\frac{\delta + 2(t - s)}{\tau^z}\right) ds \\
&= \eta^2 \frac{\tau^z}{2} \int_{\frac{\delta}{\tau^z}}^{\frac{\delta+2t}{\tau^z}} \frac{1}{\sqrt{4\pi\kappa y \tau^z}} e^{-y} dy \\
&= \frac{\eta^2}{4\sqrt{\pi}} \sqrt{\frac{\tau^z}{\kappa}} \int_{\frac{\delta}{\tau^z}}^{\frac{\delta+2t}{\tau^z}} y^{-\frac{1}{2}} e^{-y} dy
\end{aligned}$$

and obtain

$$\begin{aligned}
\lim_{t \rightarrow \infty} \mathbb{E}z(0, t)z(0, t + \delta) &= \lim_{t \rightarrow \infty} \frac{\eta^2}{4\sqrt{\pi}} \sqrt{\frac{\tau^z}{\kappa}} \int_{\frac{\delta}{\tau^z}}^{\frac{\delta+2t}{\tau^z}} y^{-\frac{1}{2}} e^{-y} dy \\
&= \frac{\eta^2}{4\sqrt{\pi}} \sqrt{\frac{\tau^z}{\kappa}} \int_{\frac{\delta}{\tau^z}}^{\infty} y^{-\frac{1}{2}} e^{-y} dy \\
&= \frac{\eta^2}{4\sqrt{\pi}} \sqrt{\frac{\tau^z}{\kappa}} \left(\Gamma\left(\frac{1}{2}\right) - \sqrt{\pi} \operatorname{erf}\left(\sqrt{\frac{\delta}{\tau^z}}\right) \right) \\
&= \frac{\eta^2}{4\sqrt{\pi}} \sqrt{\frac{\tau^z}{\kappa}} \left(\sqrt{\pi} - \sqrt{\pi} \operatorname{erf}\left(\sqrt{\frac{\delta}{\tau^z}}\right) \right) \\
&= \frac{\eta^2}{4} \sqrt{\frac{\tau^z}{\kappa}} \left(1 - \operatorname{erf}\left(\sqrt{\frac{\delta}{\tau^z}}\right) \right)
\end{aligned}$$

or for general x

$$\lim_{t \rightarrow \infty} \mathbb{E}z(x, t)z(x, t + \delta) = \frac{\eta^2}{4} \sqrt{\frac{\tau^z}{\kappa}} \left(1 - \operatorname{erf}\left(\sqrt{\frac{\delta}{\tau^z}}\right) \right). \quad (2.14)$$

From either the space or time relations we also obtain a pointwise variance,

$$\sigma^2 = \sigma_{xx}^2 = \sigma_{t0}^2 = \lim_{t \rightarrow \infty} \mathbb{E}z(x, t)z(x, t) = \frac{\eta^2}{4} \sqrt{\frac{\tau^z}{\kappa}}. \quad (2.15)$$

From here, we would like to determine what the ideal (potentially non-constant) coefficients are for coupling Equation 2.4 with a traffic model and potentially fit the resulting parameters to data. If z is to represent differences between *drivers*, the length scale it varies on should be proportional to ρ^{-1} as a single driver exists in this space. Replacing constant coefficients with non-constant values is discussed in Section 3.3 and Section 5.1. As for matching to data, the timescale over which driver behavior changes is unknown; extracting this requires separating driver bias from non-equilibrium effects. The problem of matching to data may be fundamentally different in the equilibrium and non-equilibrium cases; the nature of equilibrium traffic modeling does not allow for separation of an ‘intended’ velocity given by a fundamental diagram from an actual velocity. Determining precisely how to extract driver behavior from data in the context of an auxiliary variable of the form here will be left as an avenue for future research. For development of fundamental diagrams dependent upon a parameter, see e.g. [49, 42, 16, 14].

Looking forward to Chapters III and V because this property should be advected at the velocity of traffic, we will introduce an advection term to Equation 2.4 to obtain

$$z_t + v z_x = \kappa z_{xx} + \eta \xi - \frac{z}{\tau z}. \quad (2.16)$$

2.4 Numerical Approximation

First, let us discuss the ‘equation’

$$z_t = \eta \xi. \quad (2.17)$$

To numerically approximate cell averages

$$\bar{z}_j^n = \int_{x_{j-\frac{1}{2}}}^{x_{j+\frac{1}{2}}} z(y, t_n) dy \quad (2.18)$$

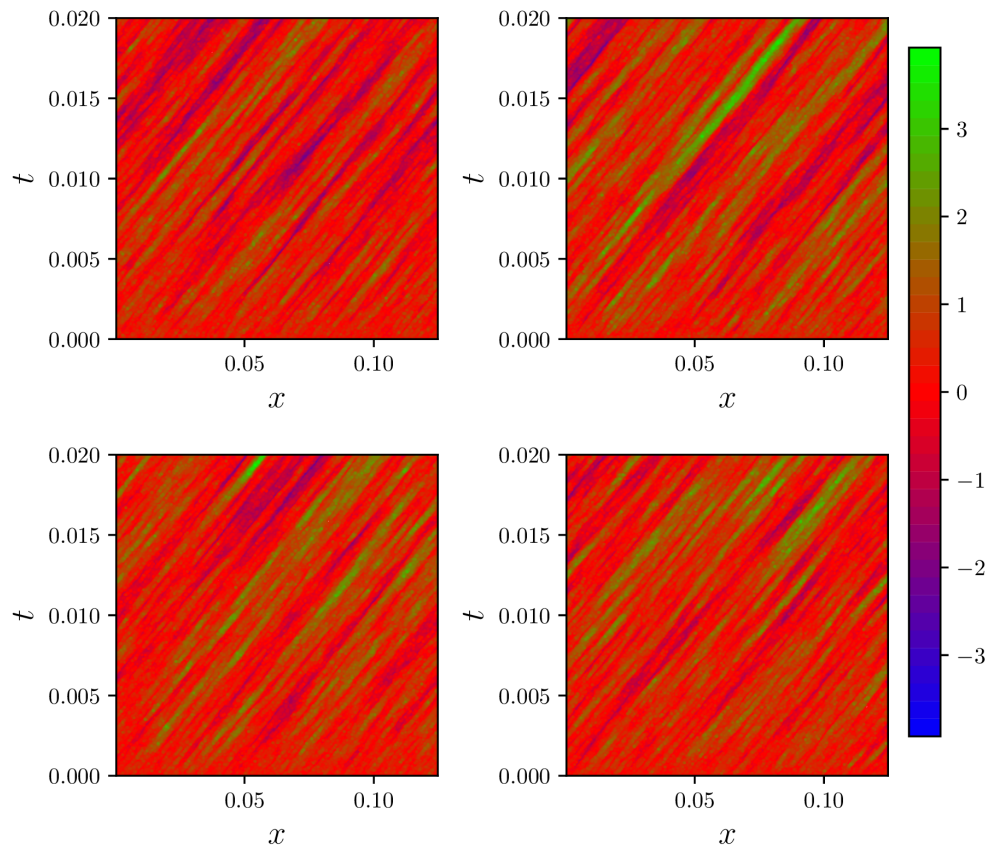


Figure 2.5: Example realizations of the stochastic heat equation with constant advection (Equation 2.16) with velocity $v = 5.0$ using $\eta = 5.7742 \times 10^{-1}$, $\kappa = 2.4522 \times 10^{-4}$, and $\tau^z = 3.5294 \times 10^{-2}$. The domain is approximated by 800 cells.

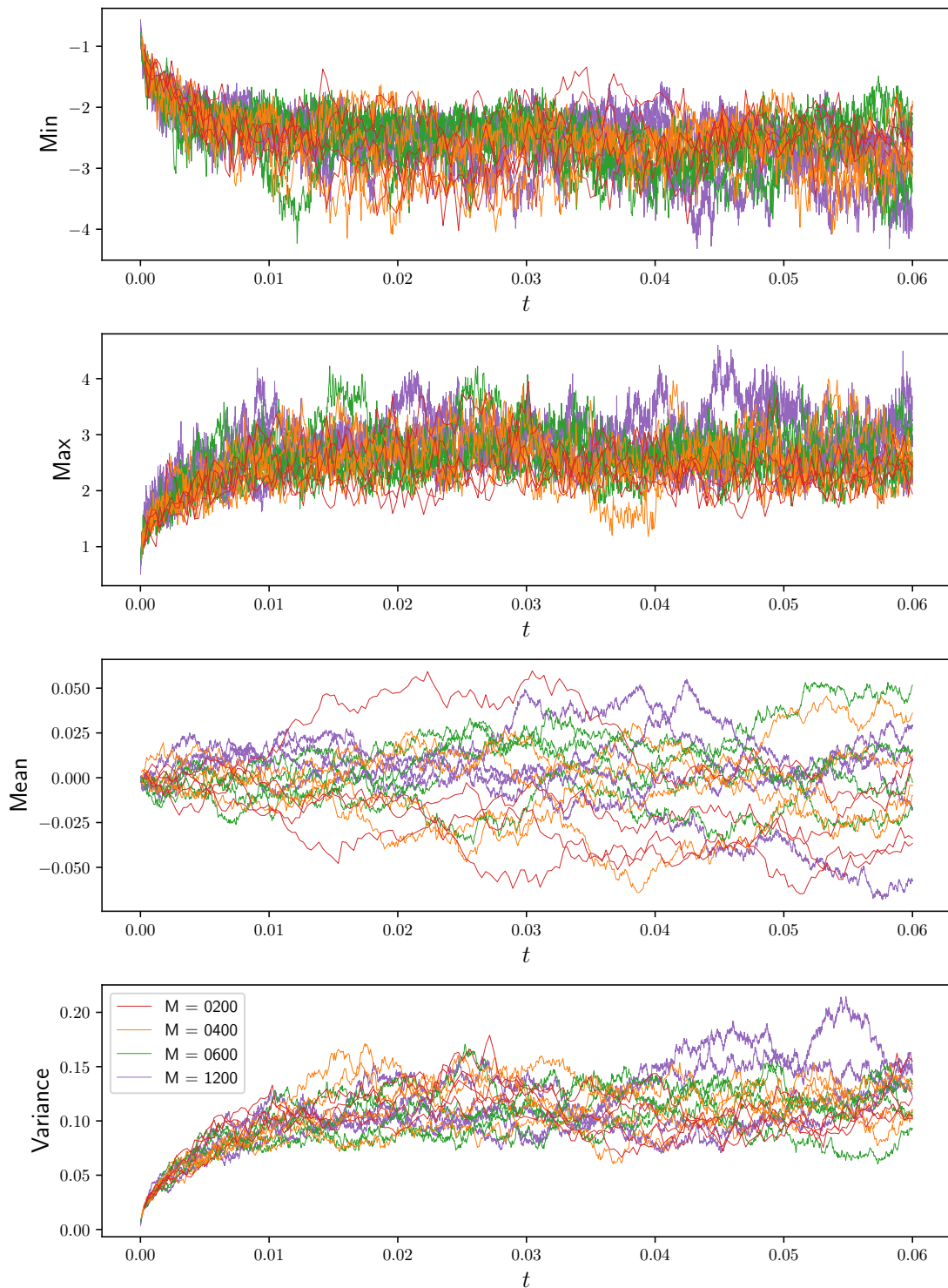


Figure 2.6: Summary statistics of example realizations of Equation 2.4 computed using the method of Section 2.4. Note that, unlike the results shown in Figure 2.2, the behavior of this process is consistent as the computational mesh is refined.

we integrate over a computational cell

$$\begin{aligned}
h\bar{z}_j^{n+1} - h\bar{z}_j^n &= \int_{x_{j-\frac{1}{2}}}^{x_{j+\frac{1}{2}}} z(y, t_{n+1}) dy - \int_{x_{j-\frac{1}{2}}}^{x_{j+\frac{1}{2}}} z(y, t_n) dy \\
&= \int_{x_{j-\frac{1}{2}}}^{x_{j+\frac{1}{2}}} \int_{t_n}^{t_{n+1}} z_t(y, \tau) d\tau dy \\
&= \int_{x_{j-\frac{1}{2}}}^{x_{j+\frac{1}{2}}} \int_{t_n}^{t_{n+1}} \xi(y, \tau) d\tau dy \\
&\sim \mathcal{N}(0, hk)
\end{aligned}$$

where ‘ $\sim \mathcal{N}(0, hk)$ ’ is understood to mean ‘normally distributed with variance hk ’. We then have

$$\frac{\bar{z}_j^{n+1} - \bar{z}_j^n}{k} = \frac{1}{\sqrt{hk}} \xi_j^n \quad (2.19)$$

where $\xi_j^n \sim \mathcal{N}(0, 1)$. This component will be used below.

Turning our attention to Equation 2.16, a computational step is split into two parts: one for the left hand side and one for the right hand side. The hyperbolic part (left hand side) is advanced by a Roe-type scheme with a flux limiter. The right hand side is taken using an explicit forward step for diffusive terms, backward Euler for the relaxation term, and forward Euler for the noise term. Explicitly, we first take the advective half-step

$$Z_j^{(1)} = Z_j^n - \nu (Z_j^n - Z_{j-1}^n + (1 - \nu) (Z_{j+1}^n - Z_j^n) \phi_{j-1} - (1 - \nu) (Z_j^n - Z_{j-1}^n) \phi_j) \quad (2.20)$$

where

$$\nu = \frac{vk}{h}$$

and

$$\phi_j = \phi \left(\frac{Z_{j-1}^n - Z_j^n}{Z_j^n - Z_{j-1}^n} \right)$$

where ϕ is a flux limiter. For the figures in this section the Superbee limiter

$$\phi^S(r) = \max(0, \min(1, 2r), \min(2, r)) \quad (2.21)$$

was used. We then take the half-step involving the right hand side

$$Z_j^{(2)} = -\frac{kZ_j^{(1)}}{\tau^z \left(1 + \frac{k}{\tau^z}\right)} + \kappa \frac{k}{2} \left(\frac{Z_{j+1}^{(1)} - 2Z_j^{(1)} + Z_{j-1}^{(1)}}{h^2} \right) + \eta \sqrt{\frac{k}{h}} \xi_j^n \quad (2.22)$$

$$\frac{\kappa k}{2} \frac{Z_{j+1}^{n+1} - 2Z_j^{n+1} + Z_{j-1}^{n+1}}{h^2} = Z_j^{(2)} \quad (2.23)$$

where $\xi_j^n \sim \mathcal{N}(0, 1)$ are i.i.d. random variables. To ensure the diffusive terms are fully resolved we choose

$$k < \min\left(\frac{h}{v}, \frac{h^2}{2\kappa}\right). \quad (2.24)$$

Example realizations computed using this method can be found in Figures 2.5 and 2.4b. We can compare basic statistics resulting from these computations Figure 2.6 to the method presented at the beginning of this chapter (Figure 2.2). For the purposes of this comparison the advective term has been neglected. Unlike the case of Figure 2.2, the minimum and maximum values are not clearly monotone with respect to mesh refinement, nor is the variance. Because a finer mesh allows more space for variation to occur, we might expect slightly wider ranges of minimum and maximum values at finer meshes, but nowhere near the clear mesh dependence shown at the beginning of this chapter.

CHAPTER III

Stochastic Equilibrium Traffic Models

In this chapter equilibrium traffic models of increasing complexity will be presented. In this context ‘equilibrium’ means velocity reacts instantaneously to changes in density. In these models velocity is a function of density, with the possible inclusion of other environmental or behavioral parameters. Mass is conserved, resulting in an LWR type equation with an additional parameter dependence in the fundamental diagram

$$\rho_t + (\rho V(\rho, z))_x = 0 \tag{3.1}$$

where z is a small random parameter. In this chapter we will discuss two ways to prescribe dynamics for z and investigate the behavior of these systems through numerical simulation. Both are based on diffusion of white noise (Section 2.2).

At this point we have put no restrictions upon what z may be or what it may depend on. There is no fundamental physics that prescribes the process describing z ; it is our choice. The underlying random process we choose for z should be easy to modify, simple to compute for unknown time horizons, and bounded. As was the case in Chapter II, nearly every mathematical statement in this thesis has the caveat of being true ‘almost surely’ and ‘almost everywhere’. For brevity and with the intended audience in mind, these caveats will be omitted from the text. We will use a stochastic heat equation (Section 2.2) to meet these requirements. Though a significant amount is known about the stochastic heat equation

with linear noise, little is known analytically about the systems to be discussed here. We will almost entirely rely on intuition and knowledge about the constituent parts to make inferences about existence of solutions and numerical methods. First, uncoupled stochastic fields will be used for z ; this is precisely a combination of Equation 3.1 with Equation 2.4. In Section 3.2 we will give a more thorough discussion of this stochastic extension to LWR using the stochastic heat equation advected with traffic as the underlying random process, and in Section 3.3 we will choose density dependent parameters in the stochastic heat equation.

3.1 LWR on the Uncoupled Stochastic Heat Equation

Using Equation 2.4 to describe driver variation we obtain the following system of equations:

$$\rho_t + (\rho V(\rho, z))_x = 0 \tag{3.2a}$$

$$z_t = \kappa z_{xx} + \eta \xi - \frac{z}{\tau z}. \tag{3.2b}$$

Because the dynamics of z do not depend on the traffic dynamics, we can think of Equation 3.2 as LWR for which the fundamental diagram is some function of space and time—an evolving topography. Utilization of a fundamental diagram that varies over space and time has been explored by other authors [5, 61, 33]. This approach differs in that z is (almost surely) continuous, and the resulting methods are independent of the chosen mesh (see Figure 2.2). There is little that can be said with regard to this system beyond Section 1.1 without numerical approximation. The system conserves mass. Wave speeds are variable with respect to a (random) function $z(x, t)$, but do not exceed traffic velocity. This model is the simplest of its class, and serves as a proof of concept that this combination of LWR and the stochastic heat equation can produce interesting phenomena not present in the unmodified equilibrium case.

3.1.1 Numerical Methods

Because in Equation 3.2 the dynamics of z do not depend on those of the modified LWR, $z(x, t)$ can be computed ahead of time if we wish, and the choice of numerical method for computing z can be made independently of the choice for ρ . We compute z_j^n using a forward time central space scheme for diffusive terms, forward Euler for the stochastic source term, and backward Euler for the relaxation term. One step is given by

$$z_j^{n+1} = z_j^n + \sqrt{\frac{k}{h}} \eta \xi_j^n - \frac{k z_j^n}{\tau z + k} + \kappa \frac{k}{h^2} (z_{j-1}^n - 2z_j^n + z_{j+1}^n) \quad (3.3)$$

where h is the size of a cell, k is the size of a timestep, and ξ_j^n are i.i.d. random normal variables. The density equation is then advanced by

$$\rho_j^{n+1} = \rho_j^n - \frac{k}{h} (F_{j+\frac{1}{2}} - F_{j-\frac{1}{2}}) \quad (3.4)$$

where $F_{j+\frac{1}{2}}$ is the numerical flux, given by

$$F_{j+\frac{1}{2}} = \begin{cases} \rho_j^n V(\rho_j^n, z_j^{n+1}) & \text{if } \lambda_j^n > \lambda_{j+1}^n \text{ and } s_{j+\frac{1}{2}}^n > 0 \\ \rho_{j+1}^n V(\rho_{j+1}^n, z_{j+1}^{n+1}) & \text{if } \lambda_j^n > \lambda_{j+1}^n \text{ and } s_{j+\frac{1}{2}}^n < 0 \\ \rho_j^n V(\rho_j^n, z_j^{n+1}) & \text{if } \lambda_j^n < \lambda_{j+1}^n \text{ and } \lambda_j^n > 0 \\ \rho_{j+1}^n V(\rho_{j+1}^n, z_{j+1}^{n+1}) & \text{if } \lambda_j^n < \lambda_{j+1}^n \text{ and } \lambda_{j+1}^n < 0 \\ \frac{1}{2} (\rho_j^n V(\rho_j^n, z_j^{n+1}) + \rho_{j+1}^n V(\rho_{j+1}^n, z_{j+1}^{n+1})) & \text{otherwise} \end{cases} \quad (3.5)$$

where

$$\lambda_j^n = V(\rho_j^n, z_j^{n+1}) + \rho_j^n V_\rho(\rho_j^n, z_j^{n+1})$$

$$s_j^n = \frac{\rho_{j+1}^n V(\rho_{j+1}^n, z_{j+1}^{n+1}) - \rho_j^n V(\rho_j^n, z_j^{n+1})}{\rho_{j+1}^n - \rho_j^n}.$$

The timestep is restricted to

$$k < \min \left(\max_j \frac{h}{|\lambda_j^n|}, \frac{h^2}{2\kappa}, 2\tau^z \right). \quad (3.6)$$

3.1.2 Parameters in the Stochastic Heat Equation

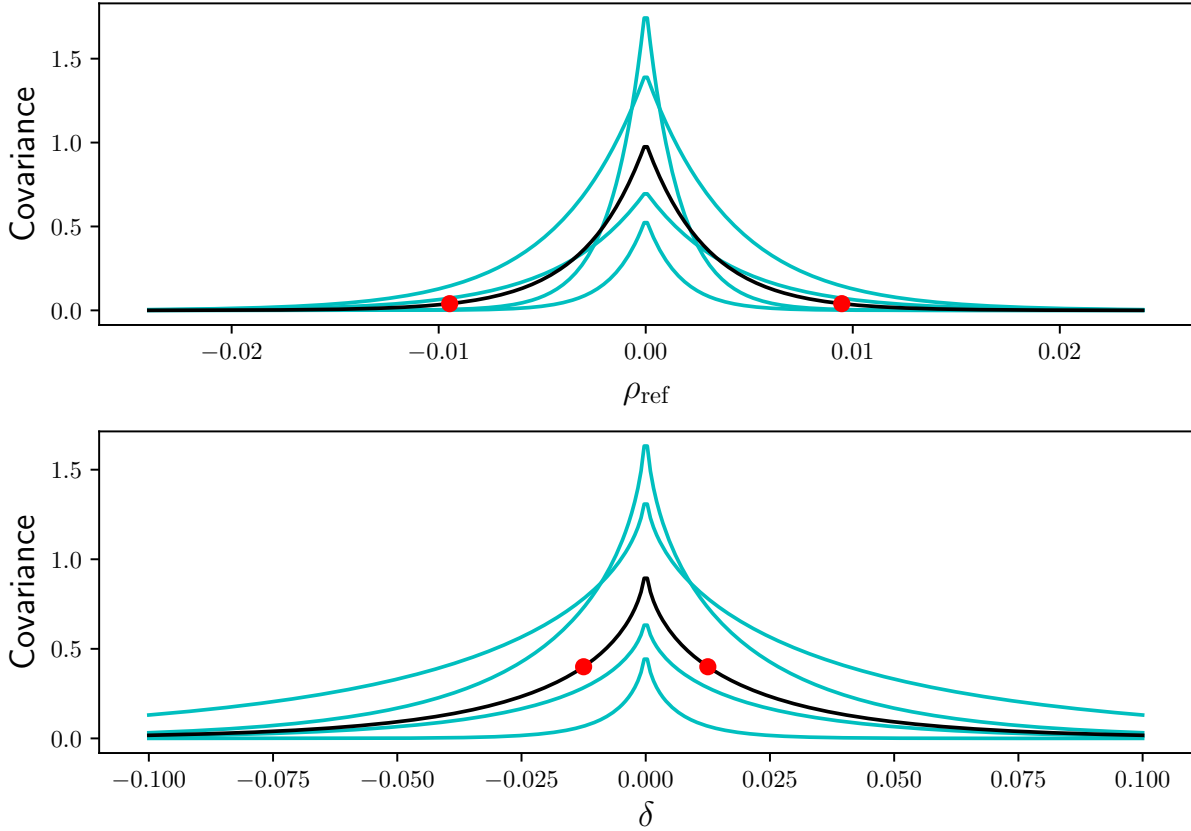
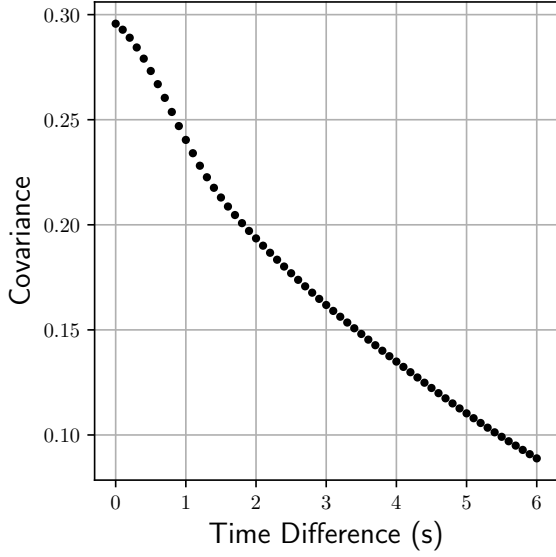
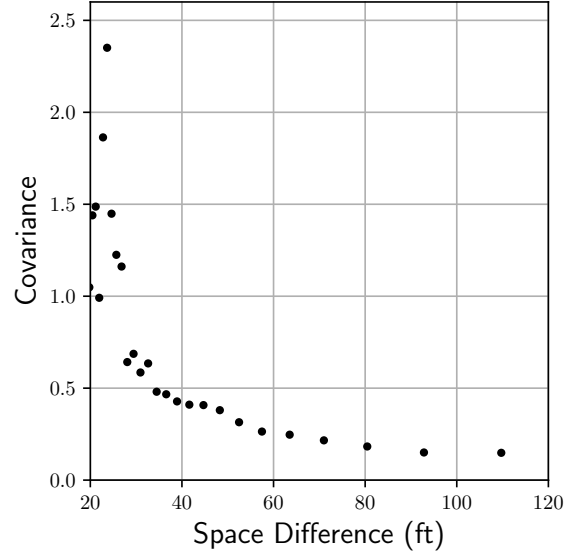


Figure 3.1: An illustration of covariance in z with respect to differences in length and time. These curves are fully determined by the selection of σ^2 (the maximum of the two curves), the chosen $(\rho_{\text{ref}}^{-1}, \sigma_x^2)$ pair (red dots on upper plot), and the (δ, σ_t^2) pair (red dots on lower plot).

To select κ , τ^z , and η it is useful to consider the Equation 2.4 detached from the traffic system. By doing so we obtain explicit relationships for the covariance between two points



(a) Autocorrelation of deviation of the mean velocity at the local density for individual drivers over time.



(b) Correlation of deviation from the mean velocity at the local density as a function of distance.

Figure 3.2: Statistics of $\frac{V_0(\rho) - v}{V_1(\rho)}$ for individual cars where $V_0(\rho)$ and $V_1(\rho)$ are the mean and standard deviation respectively of velocity at a given density computed from NGSIM [50] vehicle trajectories.

Table 3.1: Parameters used to evolve z (Equations 3.2 and 3.10) in this chapter. The tables on the left and right are equivalent through Equations 3.7a, 3.7b, and 3.7c (or alternatively Equations 3.25a, 3.25b, and 3.25c). Note these are the same parameters used throughout Chapter II.

Physical Description		Parameter Values	
σ^2	1.0	η	5.7742×10^{-1}
σ_x^2	0.04	κ	2.4522×10^{-4}
σ_t^2	0.4	τ^z	3.5294×10^{-2}
δ	45 / 3600	ρ_{ref}	120.0

with either a time or space separation (see Section 2.3):

$$\sigma_x^2 = \lim_{t \rightarrow \infty} \mathbb{E} z(x, t) z(x + \rho_{\text{ref}}^{-1}, t) = \frac{\eta^2}{4} \sqrt{\frac{\tau^z}{\kappa}} \exp\left(-\frac{1}{\sqrt{\tau^z \kappa}} \rho_{\text{ref}}^{-1}\right) \quad (3.7a)$$

$$\sigma_t^2 = \lim_{t \rightarrow \infty} \mathbb{E} z(x, t) z(x, t + \delta) = \frac{\eta^2}{4} \sqrt{\frac{\tau^z}{\kappa}} \left(1 - \text{erf}\left(\sqrt{\frac{\delta}{\tau^z}}\right)\right) \quad (3.7b)$$

$$\sigma^2 = \lim_{t \rightarrow \infty} \mathbb{E} (z(x, t))^2 = \frac{\eta^2}{4} \sqrt{\frac{\tau^z}{\kappa}}. \quad (3.7c)$$

These curves are fully determined by the choice of a length scale ρ_{ref}^{-1} , a time scale δ , the desired correlations over those scales σ_x^2 and σ_t^2 , and a pointwise variance σ^2 (Figure 3.1). The five values ρ_{ref}^{-1} , σ_x^2 , δ , σ_t^2 , and σ^2 uniquely determine the parameters η , κ , and τ^z using Equations 3.7. This choice can be visualized per Figure 3.1 as the selection of a single curve (black) from a family of possible curves (cyan) using these constraints (red).

We would like to choose these parameters such that, away from initial conditions, z varies at appropriate scales in time and space. If an analogy to a car-following model in which drivers carry their own independent z variable is made, then z would be constant over the length of road occupied by one driver, and be entirely uncorrelated with the constant regions ahead and behind. As a consequence of treating traffic as a continuum, this is not possible, nor is it necessarily desired. Further, the form of correlation as a function of distance has been determined by our choice of random process. If the stochastic heat equation is to be used, we must choose the parameters that best adapt the class of smooth curves with the step function that exists in the microscopic case (Figure 3.1). It is not clear what might guide the selection of a time scale. In what follows we will choose the pointwise variance (Equation 3.7c) to be one. This is a convenient scaling, but not one that is necessarily equivalent to the choices made in Section 1.2.2. The work by Fan et al [14, 15] has fit similar non-stochastic models to data.

An additional difficulty that arises in finding a proper scaling is that traffic dynamics are qualitatively driven as much by the extrema of z over a region in space as the mean

over a region in space. We will use a fundamental diagram that has the same form, but not an equivalent scaling, to that of Section 1.2.2. To investigate the effect of the stochastic parameter z , we will introduce an additional constant ω to control the amplitude of z by replacing Equation 3.2a with

$$\rho_t + (\rho V(\rho, \omega z))_x = 0. \quad (3.8)$$

Unless otherwise noted, $\omega = 1$.

3.1.3 The Ringroad Experiment

Figures 3.3 and 3.4 show sample realizations with periodic boundary conditions (see Section 1.3.1). While the density fields and stochastic fields are not smooth, the integrals of vehicle trajectories are smooth. Vehicle trajectories show that backward moving congestion waves develop spontaneously and consistently. Typically a smoothing \tilde{g} of noisy data g takes the form

$$\tilde{g}(x) = \int K(x - y)g(y) dy \quad (3.9)$$

where K is a kernel that must be chosen. Visualizing vehicle trajectories avoids the need for this arbitrary choice. Though the models are very different, it is interesting to compare the vehicle trajectories obtained by integrating a macroscopic equilibrium model like those in Figure 3.3 or Figure 3.4 with those of the microscopic pedestrian model in [62]. This is also the case for the figures that follow.

3.2 A Stochastic Extension to LWR with Constant Coefficients

Some previous authors have introduced driver behavior parameters [33, 38, 14]; here we will introduce a parameter governed by a random process. If z is to correspond to some property of an individual driver, it should be advected at the speed of traffic. To make z behave as a property of the driver rather than a property of the road, we modify

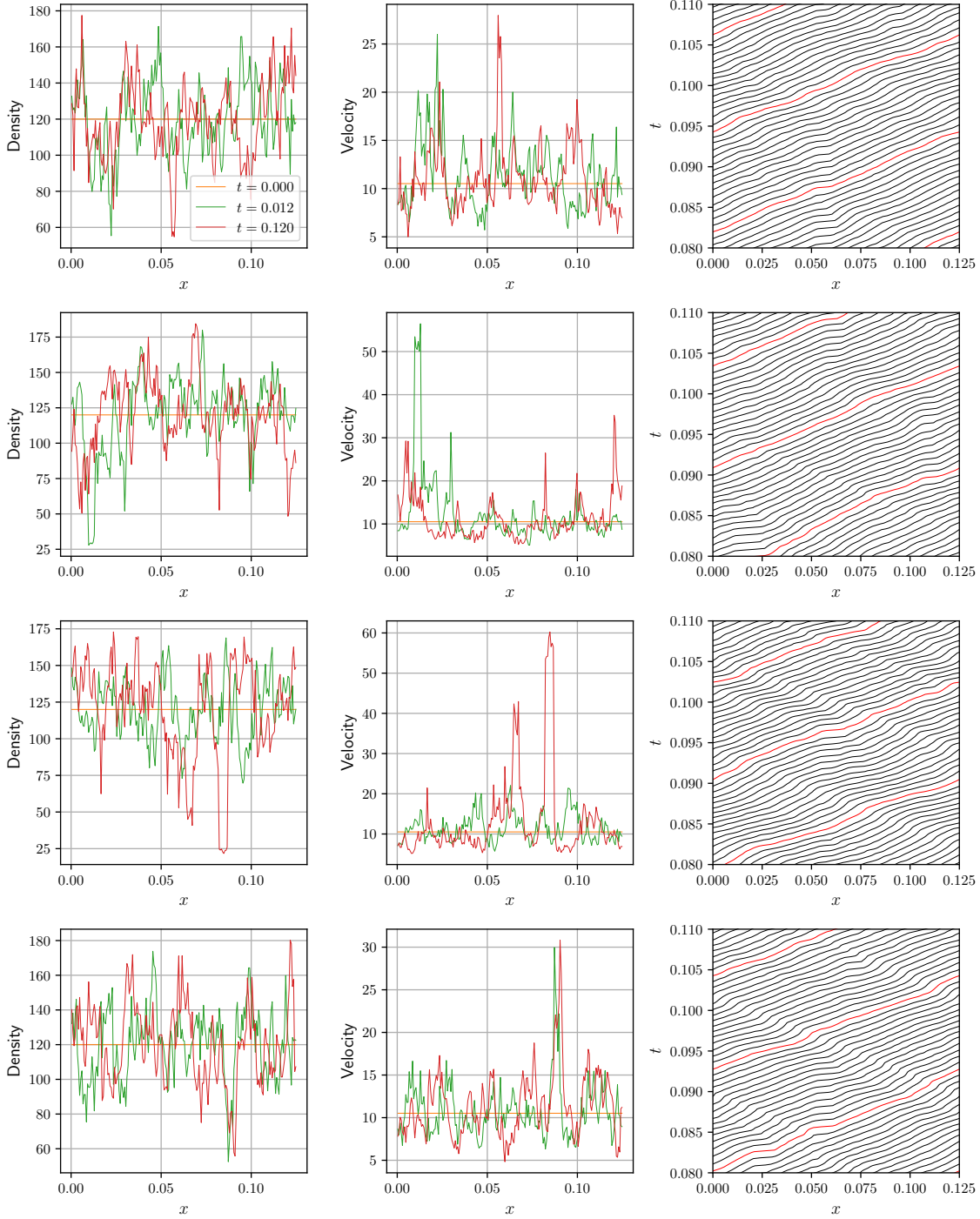


Figure 3.3: Four realizations of the ringroad experiment using LWR modified by a (decoupled) random process z (Equation 3.2). The linearized fundamental diagram (Equation 1.21) and the parameters in Table 1.2 with $\omega = 1$ were used with an initial density of $\rho_0 = 120.0$. Each row represents an independent realization. The first column shows the density profile at the initial time, and early time, and a later (fully developed) time; the second column shows the velocity profile at the same times; the third column shows sample vehicle trajectories.

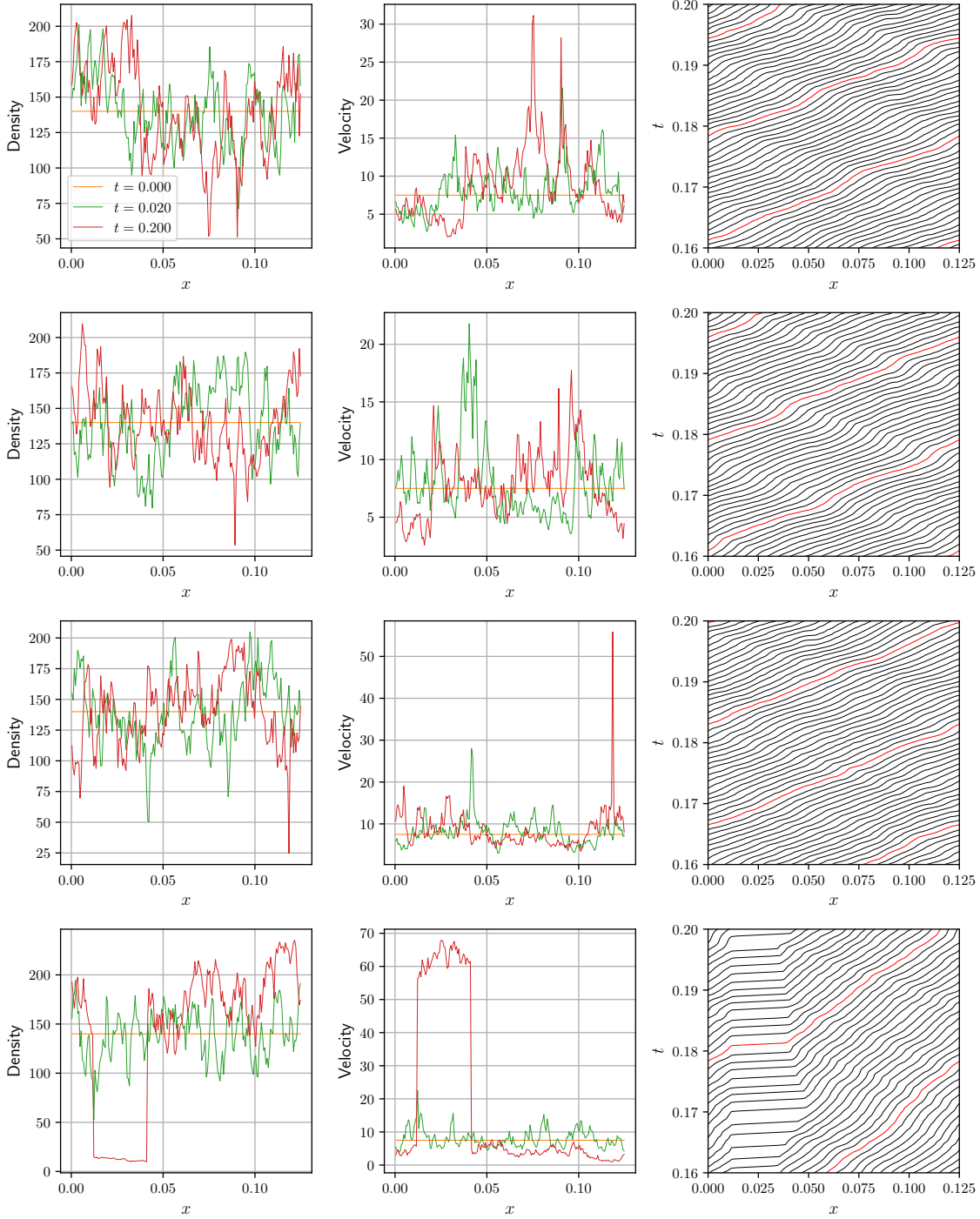


Figure 3.4: Four realizations of the ringroad experiment using LWR modified by a (decoupled) random process z (Equation 3.2). The linearized fundamental diagram (Equation 1.21) and the parameters in Table 1.2 with $\omega = 1$ were used with an initial density of $\rho_0 = 140.0$. Each row represents an independent realization. The first column shows the density profile at the initial time, and early time, and a later (fully developed) time; the second column shows the velocity profile at the same times; the third column shows sample vehicle trajectories.

Equation 3.2b to include an advection term

$$\rho_t + (\rho V(\rho, \omega z))_x = 0 \quad (3.10a)$$

$$z_t + V(\rho, \omega z)z_x = \kappa z_{xx} + \eta \xi - \frac{z}{\tau z}. \quad (3.10b)$$

One consequence of introducing a stochastic component to driver behavior is that many of the properties desired for macroscopic traffic models [2, 18] are violated or become difficult to analyze. In particular, the inclusion of the viscous term κz_{xx} renders the system no longer hyperbolic. However, introduction of the viscous regularization of the stochastic field in an auxiliary variable avoids most of the problems typically caused by viscous terms in traffic models. What follows is a reflection upon the traffic modeling principles outlined in [11, 2, 18] with respect to this system, followed by numerical results.

3.2.1 Hyperbolicity, Anisotropy, and Boundedness

The non-conservative form of Equation 3.10 is

$$\begin{bmatrix} \rho \\ z \end{bmatrix}_t + \underbrace{\begin{bmatrix} V + \rho V_\rho & \rho V_z \\ 0 & V \end{bmatrix}}_A \begin{bmatrix} \rho_x \\ z_x \end{bmatrix} = \begin{bmatrix} 0 \\ \kappa z_{xx} - \frac{z}{\tau z} + \eta \xi \end{bmatrix}. \quad (3.11)$$

This system has eigenvalues $\lambda_1 = V + \rho V_\rho$ and $\lambda_2 = V$. If $V_\rho \leq 0$ then $\lambda_1 \leq \lambda_2$. As usual, we will let

$$\Lambda = \begin{bmatrix} \lambda_1 & 0 \\ 0 & \lambda_2 \end{bmatrix}. \quad (3.12)$$

The corresponding eigenvectors (such that $AR = R\Lambda$) are

$$R = [\mathbf{r}_1 \ \mathbf{r}_2] = \begin{bmatrix} \rho & -\frac{V_z}{V_\rho} \\ 0 & 1 \end{bmatrix}. \quad (3.13)$$

As one would expect, the wave corresponding to $\lambda_2 = V(\rho, z)$ is linearly degenerate (i.e. $\nabla\lambda_2 \cdot \mathbf{r}_2 = 0$). The wave corresponding to $\lambda_1 = V(\rho, z) + \rho V_\rho(\rho, z)$ mirrors the behavior of LWR in that

$$\nabla\lambda_1 \cdot \mathbf{r}_1 = \rho(\rho V_{\rho\rho} + 2V_\rho) = \rho \frac{\partial}{\partial \rho} (V + \rho V_\rho). \quad (3.14)$$

From this we conclude that acceleration causes rarefactions and deceleration causes shocks, to the same extent that is the case in LWR.

The matrix A in Equation 3.11 is diagonalizable (and the system is hyperbolic) as long as the ratio V_z/V_ρ is defined. We might expect $V_\rho = 0$ for very low densities (free flow) and very high densities (stationary traffic). In the case of very high densities, this condition will be satisfied as would not expect even the most aggressive driver to accelerate with nowhere to go. For free flow, though we may expect constant velocity, most data collected suggests that there is a non-negligible decrease in velocity as density increases, even in free flow (see e.g. [65, 42]). In the case that this ratio is indeterminate, i.e. in regimes where all drivers behave identically, the system decouples as expected.

Hyperbolicity is generally considered a requirement for macroscopic traffic flow modeling with PDE [11, 2], and any relaxation of hyperbolicity should be justified. The inclusion of viscous terms and source terms result in a system that is not hyperbolic. We required that solutions to our underlying stochastic process be well-defined and (a.s.) bounded, but the coupling present in Equation 3.10 does not ensure such a result. Some authors (e.g. [33]) have taken an approach similar to the one at hand without a regularizing term in space; it is not clear in these cases that a solution to a differential equation is being computed (See Chapter II). The ‘regularization’ that appears on these solutions is likely dependent on

the amount of erroneous dissipation in the numerical scheme. Including a dissipative term allows a high-resolution treatment of the hyperbolic part and ensures the dominant part of the regularizing diffusion is not numerical error. In Section 2.4 mesh dependence for this type of ‘source term’ was demonstrated. In short, the justification for the viscous term is necessary for solutions to be independent of the discretization. This is true of an approach that includes stochasticity in space and time. Only including stochasticity in time (uniformly across space) results only in time uncertainty [42]. Including stochastic variation in space (or as a fixed property of drivers) has also been explored by previous authors [34, 19].

3.2.2 Vehicles have Personalities that Remain Unchanged by Motion

Daganzo [11] noted that “vehicles have personalities (e.g., aggressive and timid) that remain unchanged by motion.” Some authors (e.g. [2, 59]) have addressed this by noting that the second order models in question have the spirit of or are derived from car following models, whereas some [33, 4] have included a conserved quantity representing some kind of characteristic, addressing this point directly. The case for the regularization term has been made in Section 3.2.1. The decision for the driver-dependent property to be advected rather than conserved is in closer alignment to the fundamental principle that cars have ‘personalities.’

3.2.3 Numerical Methods

Unlike Equation 3.2, Equation 3.10 couples the driver variation process z with the evolution of traffic density ρ ; z cannot be computed independently of ρ . For the numerical results that follow, we discretize Equation 3.10 with an operator splitting in which the hyperbolic part (left hand side) is handled by a first-order wave propagation scheme and the source terms (right hand side) consists of a random increment, backward Euler for the relaxation term, and a forward time central space scheme for the diffusion term. A computational step

consists of the following:

$$\begin{bmatrix} \rho_j^* \\ z_j^* \end{bmatrix} = \begin{bmatrix} \rho_j^n \\ z_j^n \end{bmatrix} - \frac{k}{h} \left(R_{j-\frac{1}{2}} \Lambda_{j-\frac{1}{2}}^+ \boldsymbol{\alpha}_{j-\frac{1}{2}} + R_{j+\frac{1}{2}} \Lambda_{j+\frac{1}{2}}^- \boldsymbol{\alpha}_{j+\frac{1}{2}} \right) \quad (3.15a)$$

$$\rho_j^{n+1} = \rho_j^* \quad (3.15b)$$

$$z_j^{n+1} = z_j^* + \sqrt{\frac{k}{h}} \eta \xi_j^n - \frac{z_j^*}{1 + \frac{\tau^z}{k}} + \kappa \frac{k}{h^2} (z_{j-1}^* - 2z_j^* + z_{j+1}^*) \quad (3.15c)$$

where h is the cell width, k is the size of the timestep, Λ^+ (resp. Λ^-) are the element-wise maximum (resp. minimum) of Λ and zero,

$$\boldsymbol{\alpha} = \begin{bmatrix} \alpha_1 \\ \alpha_2 \end{bmatrix} = \begin{bmatrix} \frac{\Delta\rho}{\bar{\rho}} + \frac{\bar{V}_z}{\bar{\rho}\bar{V}_\rho} \Delta z \\ \Delta z \end{bmatrix}, \quad (3.16)$$

and ξ_j^n are i.i.d. random normal variables. Wave directions, speeds, and strengths are obtained from the eigendecomposition $A_{j+\frac{1}{2}} R_{j+\frac{1}{2}} = R_{j+\frac{1}{2}} \Lambda_{j+\frac{1}{2}}$ where $A_{j+\frac{1}{2}}$ is a chosen average of the Jacobian matrix (Equation 3.11) between cells j and $j+1$. We will refer to the left and right states as (ρ_L, z_L) and (ρ_R, z_R) , the corresponding velocities as $V_L = V(\rho_L, z_L)$ and $V_R = V(\rho_R, z_R)$, and differences as $\Delta\rho = \rho_R - \rho_L$, $\Delta z = z_R - z_L$, $\Delta V = V_R - V_L$, and $\Delta(\rho V) = \rho_R V_R - \rho_L V_L$. To conserve mass, we must have

$$\Delta(\rho V) = (\bar{V} + \bar{\rho}\bar{V}_\rho)\Delta\rho + \bar{\rho}\bar{V}_z\Delta z \quad (3.17)$$

$$= \bar{\rho} (\bar{V}_\rho\Delta\rho + \bar{V}_z\Delta z) + \bar{V}\Delta\rho. \quad (3.18)$$

If we require

$$\Delta V = \bar{V}_\rho\Delta\rho + \bar{V}_z\Delta z \quad (3.19)$$

then we must have

$$\Delta(\rho V) = \bar{\rho} \Delta V + \bar{V} \Delta \rho. \quad (3.20)$$

Because there is no conserved quantity corresponding to the property z the choice of \bar{z} is an unrestricted (as long as it is an average). We will use the simple arithmetic averages

$$\bar{\rho} = \frac{\rho_L + \rho_R}{2} \quad (3.21a)$$

$$\bar{z} = \frac{z_L + z_R}{2} \quad (3.21b)$$

$$\bar{V} = \frac{V_L + V_R}{2} \quad (3.21c)$$

To choose \bar{V}_ρ and \bar{V}_z such that Equation 3.19 is satisfied we take inspiration from [45]. The point

$$(x, y) = (V_\rho^*, V_z^*) = \left(\frac{1}{2} (V_\rho(\rho_L, z_L) + V_\rho(\rho_R, z_R)), \frac{1}{2} (V_z(\rho_R, z_R) + V_z(\rho_L, z_L)) \right)$$

is projected onto the line $x\Delta\rho + y\Delta z = \Delta V$ to obtain $(\bar{V}_\rho, \bar{V}_z)$. In other words, we choose \bar{V}_ρ and \bar{V}_z such that

$$(\bar{V}_\rho - V_\rho^*)^2 + (\bar{V}_z - V_z^*)^2$$

is minimized subject to Equation 3.19 where V_ρ^* and V_z^* are averages of the partial derivatives evaluated at the left and right states. The resulting approximations to the partial derivatives at the cell interface are

$$\bar{V}_\rho = \frac{(\Delta z)^2 V_\rho^* - (\Delta \rho)(\Delta z) V_z^* + (\Delta \rho)(\Delta V)}{(\Delta \rho)^2 + (\Delta z)^2} \quad (3.22a)$$

$$\bar{V}_z = \frac{-(\Delta \rho)(\Delta z) V_\rho^* + (\Delta \rho)^2 V_z^* + (\Delta z)(\Delta V)}{(\Delta \rho)^2 + (\Delta z)^2}. \quad (3.22b)$$

To obtain formulas that may be numerically evaluated for $(\Delta\rho)^2 + (\Delta z)^2 \approx 0$, we rearrange some terms and introduce a small $\epsilon > 0$:

$$\bar{V}_\rho \approx \left(1 + \frac{(\Delta\rho)^2}{(\Delta z)^2 + \epsilon}\right)^{-1} V_\rho^* + \left(\frac{(\Delta\rho)}{(\Delta\rho)^2 + (\Delta z)^2 + \epsilon}\right) (-(\Delta z)V_z^* + \Delta V) \quad (3.23a)$$

$$\bar{V}_z \approx \left(1 + \frac{(\Delta z)^2}{(\Delta\rho)^2 + \epsilon}\right)^{-1} V_z^* + \left(\frac{\Delta z}{(\Delta\rho)^2 + (\Delta z)^2 + \epsilon}\right) (-(\Delta\rho)V_\rho^* + \Delta V) \quad (3.23b)$$

These formulas recover the limit $(\bar{V}_\rho(\rho, z), \bar{V}_z(\rho, z)) \rightarrow (V_\rho(\bar{\rho}, \bar{z}), V_z(\bar{\rho}, \bar{z}))$ as $\Delta\rho, \Delta z \rightarrow 0$.

3.2.4 The Ringroad Experiment

Figures 3.5 and 3.6 show realizations of the ringroad experiment (Section 1.3.1) with moderate and high density. At moderate density (Figure 3.5) we observe separation of traffic into high and low density regimes. In this regime we see that blocks of traffic are forced to deviate from the fundamental diagram to the same extent as the slowest driver. Because the domain is small, the overall velocity decreases dramatically due to this (inevitable) limiting driver. Figure 3.6 shows the same experiment with a higher density. In the higher density regime we see ‘stop and go’ patterns develop; this is most clearly seen in vehicle trajectories. The development of this pattern is remarkably consistent across realizations. Figures 3.7 and 3.8 show the same two scenarios with 20% more variation in the fundamental diagram, greatly exaggerating the effects discussed.

Beyond showing that individual realizations are capable of exhibiting the desired behavior, as we increase the level of driver variation (through varying ω), we observe an increase in travel time. This can be seen in the the distribution across realizations of times taken to traverse the domain after a period of time (Figure 3.9) and the minimum velocity across the domain at this time (Figure 3.10). It is also of note that the variance in transit time (Figure 3.9) increases substantially as the effect of noise ω is increased. Practical use of the models in this section would require the stochastic parameters and fundamental diagram to be properly estimated. Because the deviation from the mean velocity $|V(\rho, z) - V(\rho, 0)|$ is

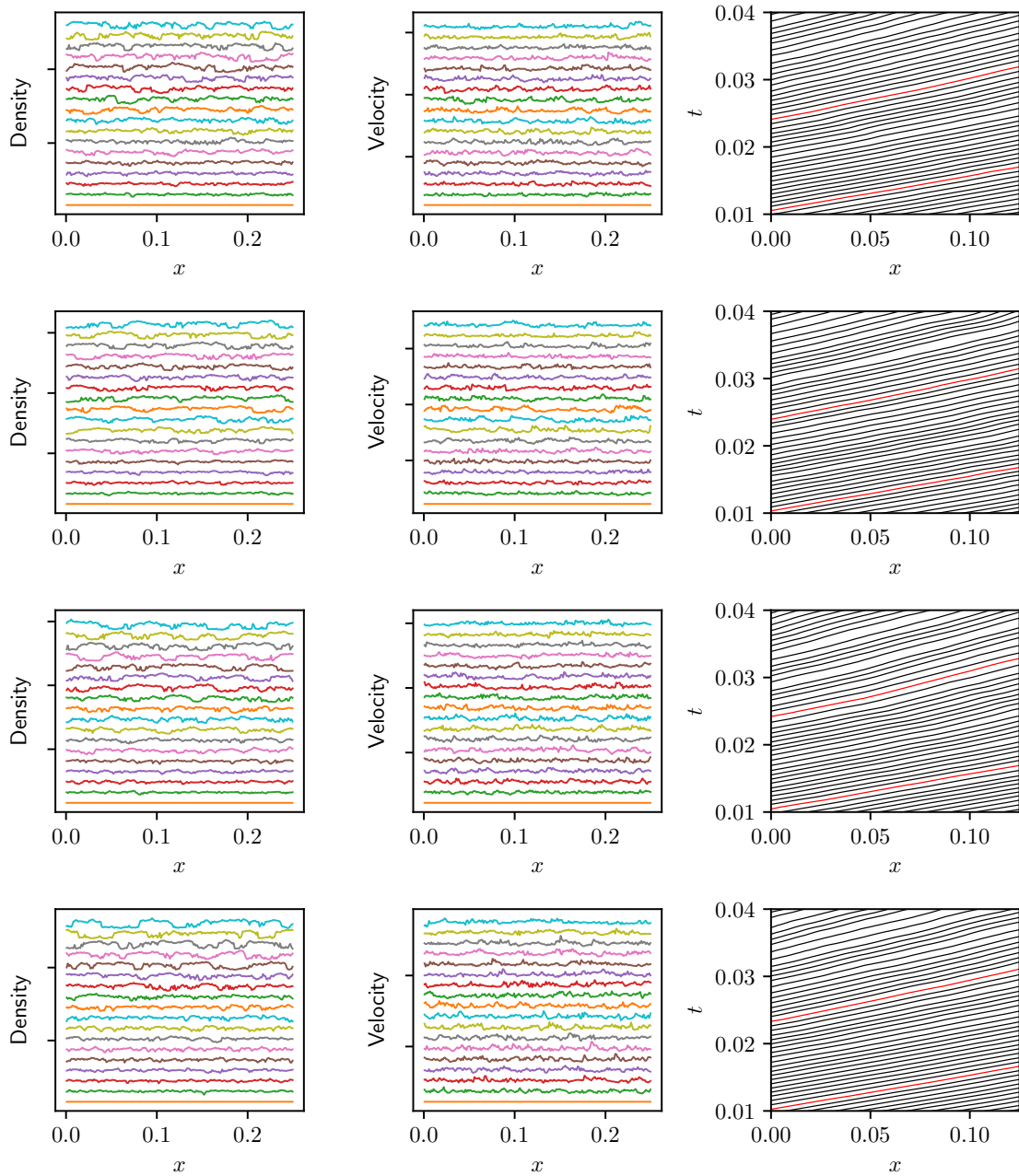


Figure 3.5: Realizations of the ringroad experiment using the LWRZ model (Equation 3.10) using the linearized fundamental diagram (Equation 1.21) and the parameters in Table 1.2. The initial density is $\rho_0 = 80.0$ and $\omega = 1.0$. Each row represents an independent realization. The first column shows the density profile at the initial time, and early time, and a later (fully developed time); the second column shows the velocity profile at the same times; the third column shows vehicle trajectories.

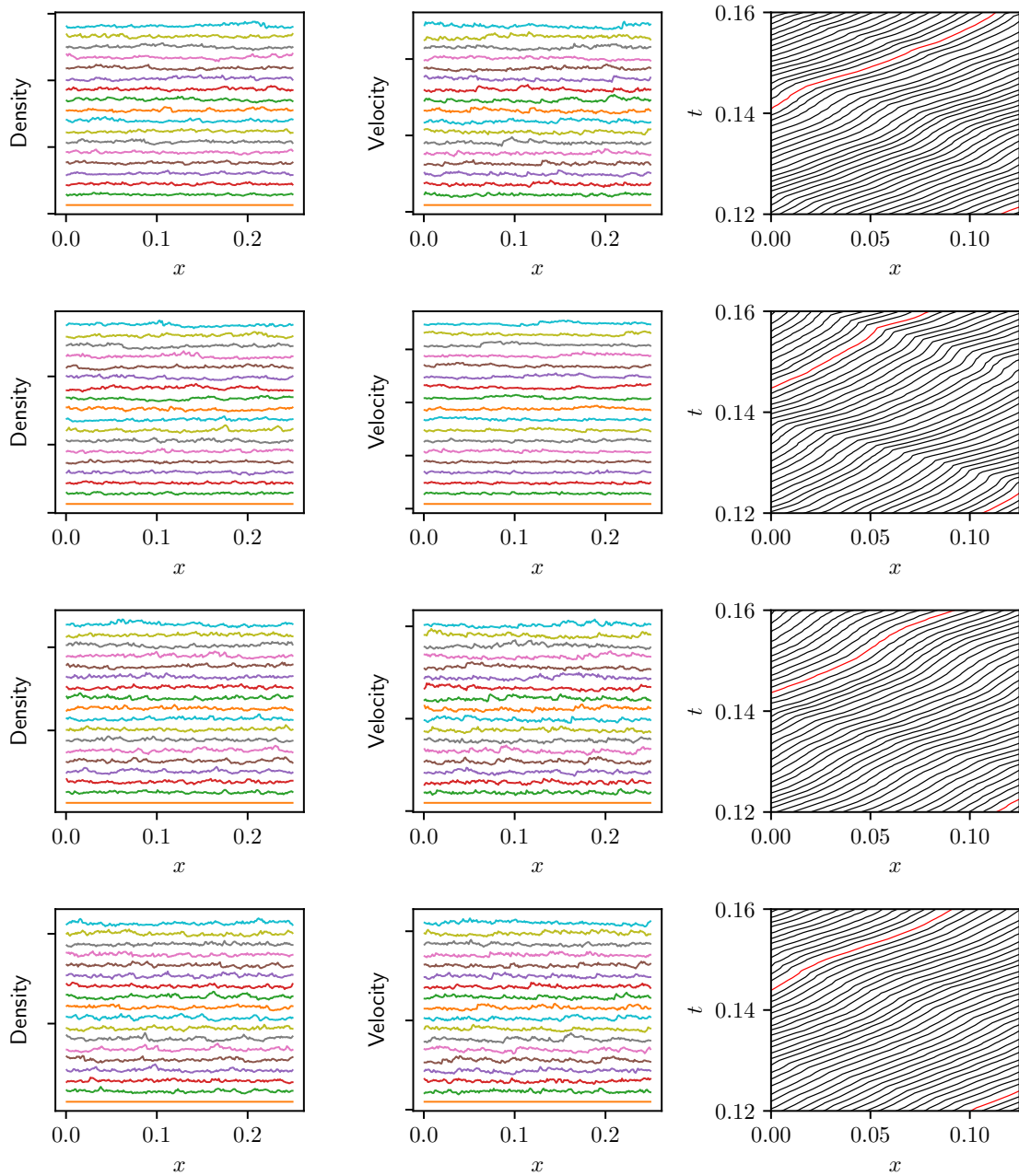


Figure 3.6: Realizations of the ringroad experiment using the LWRZ model (Equation 3.10) using the linearized fundamental diagram (Equation 1.21) and the parameters in Table 1.2. The initial density is $\rho_0 = 130.0$ and $\omega = 1.0$. Each row represents an independent realization. The first column shows the density profile at the initial time, and early time, and a later (fully developed time); the second column shows the velocity profile at the same times; the third column shows vehicle trajectories.

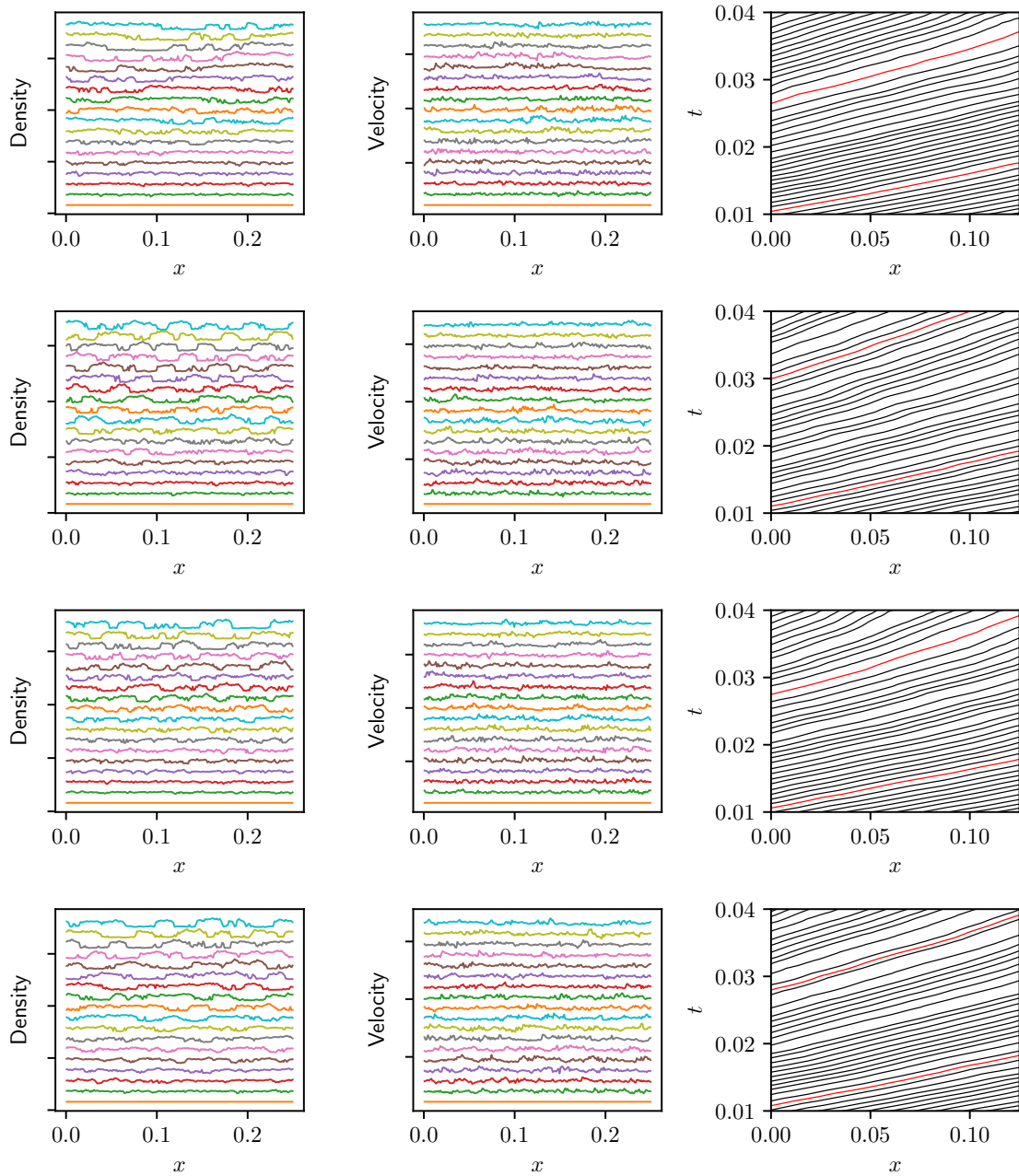


Figure 3.7: Realizations of the ringroad experiment using the LWRZ model (Equation 3.10) using the linearized fundamental diagram (Equation 1.21) and the parameters in Table 1.2. The initial density is $\rho_0 = 80.0$ and $\omega = 1.2$. Each row represents an independent realization. The first column shows the density profile at the initial time, and early time, and a later (fully developed time); the second column shows the velocity profile at the same times; the third column shows vehicle trajectories.

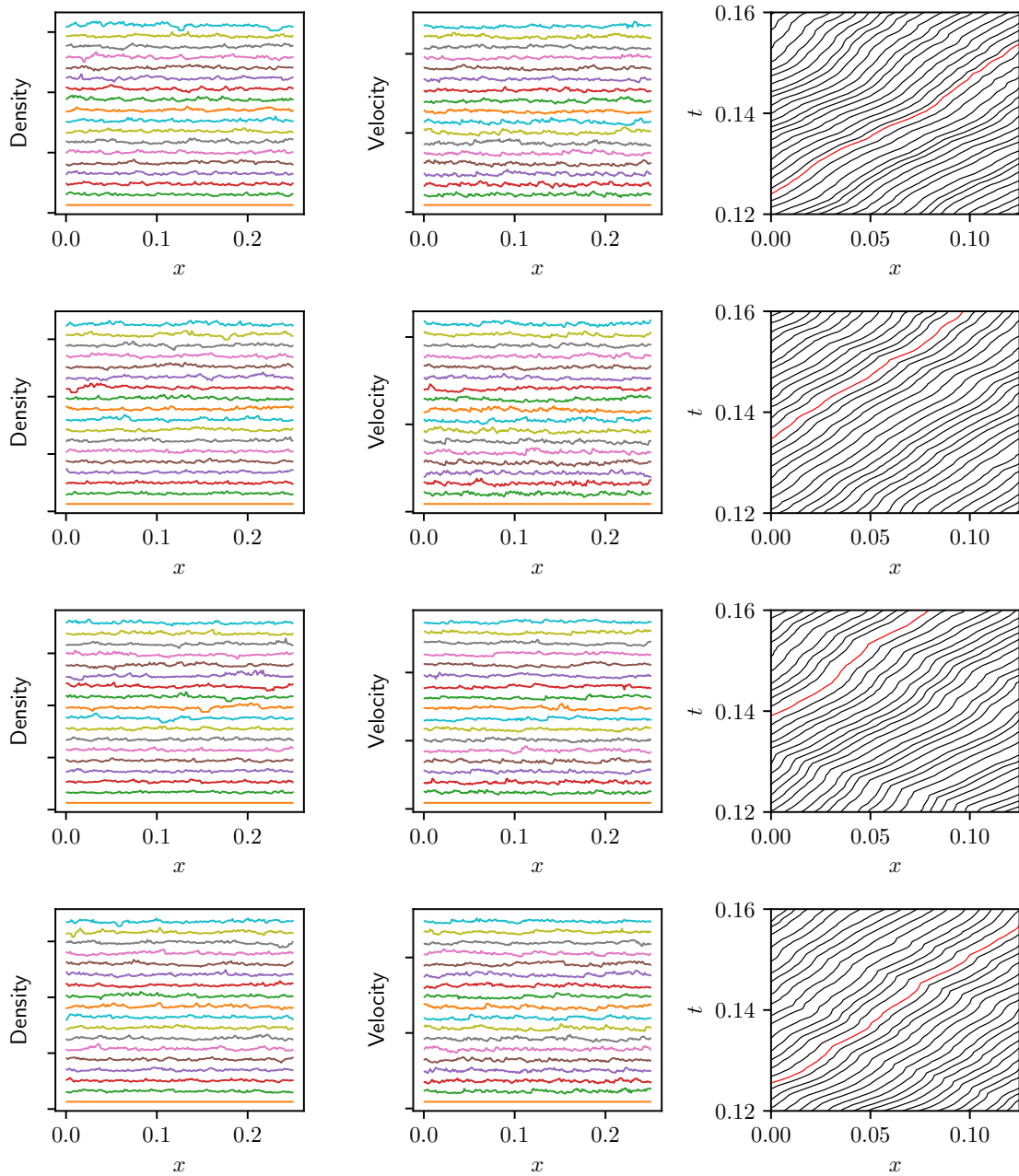


Figure 3.8: Realizations of the ringroad experiment using the LWRZ model (Equation 3.10) using the linearized fundamental diagram (Equation 1.21) and the parameters in Table 1.2. The initial density is $\rho_0 = 130.0$ and $\omega = 1.2$. Each row represents an independent realization. The first column shows the density profile at the initial time, and early time, and a later (fully developed time); the second column shows the velocity profile at the same times; the third column shows vehicle trajectories.

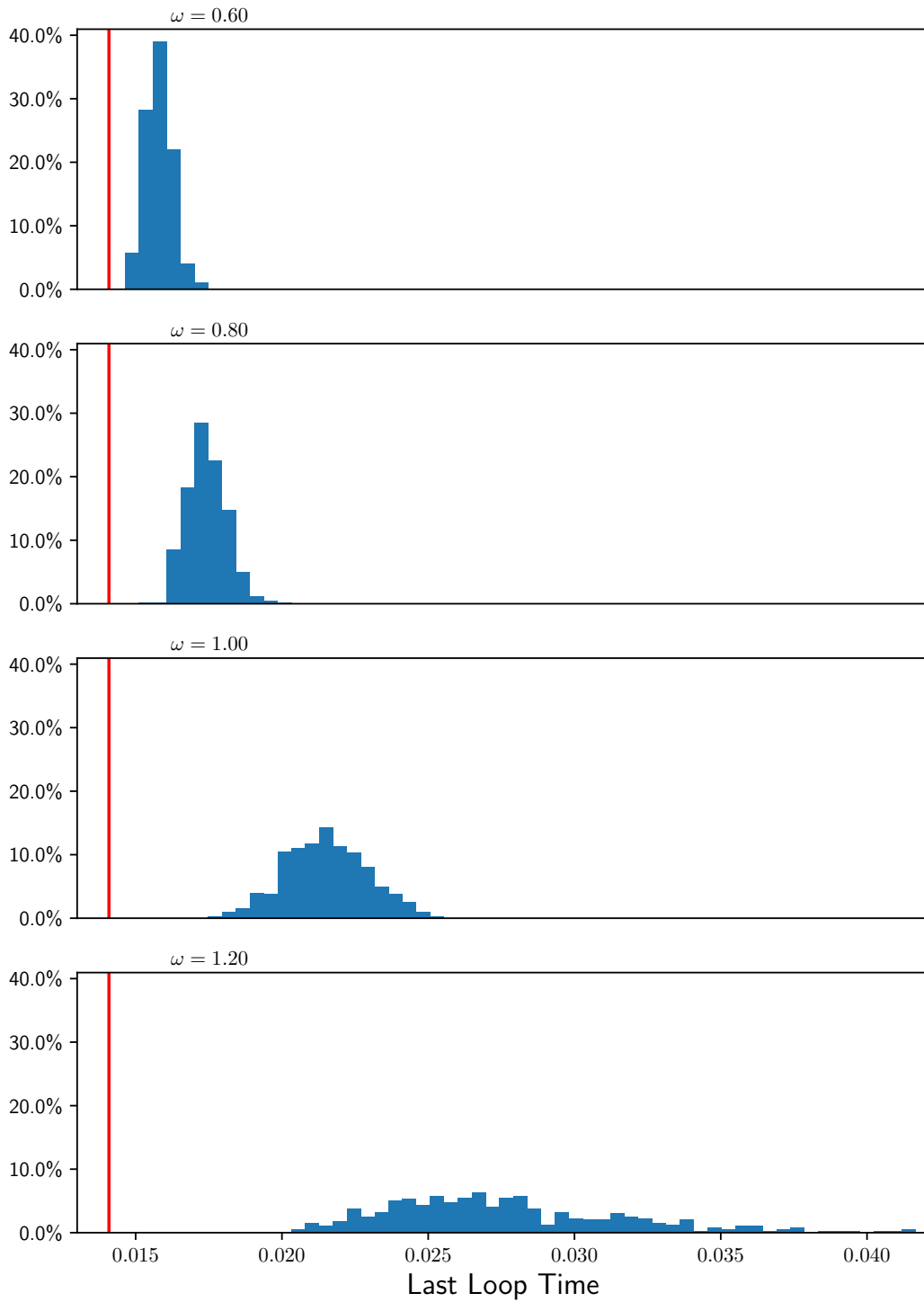


Figure 3.9: Histograms showing the distribution of the final time to traverse the domain (i.e. the last traversal before $t = 0.08$) across realizations of Equation 3.10 with constant coefficients as the amplitude of noise (ω) varies. Background density is $\rho_0 = 130.0$. Each histogram is compiled from 400 realizations.

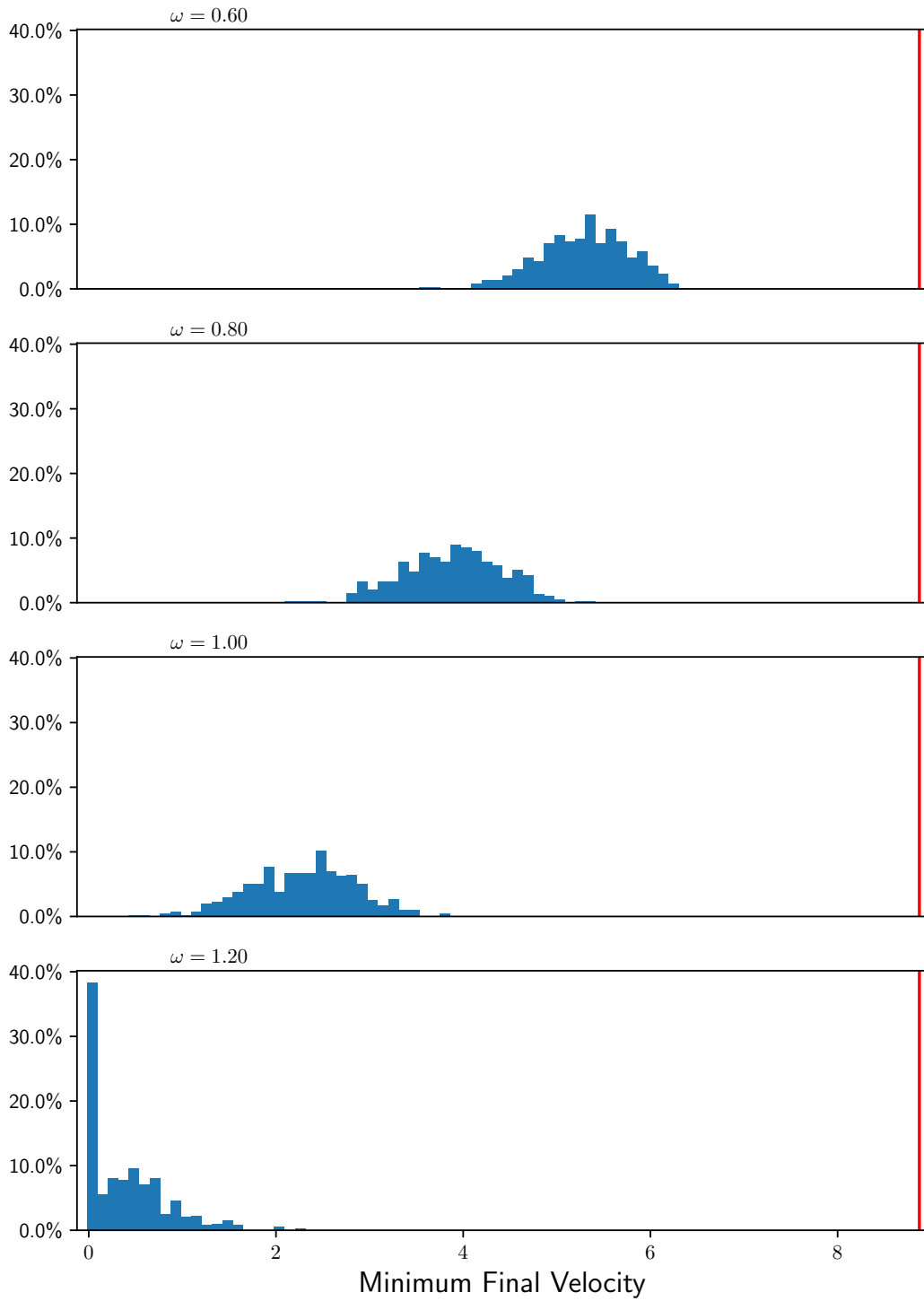


Figure 3.10: Histograms showing the distribution of minimum velocity at $t = 0.08$ across realizations of Equation 3.10 with constant coefficients as the level of noise (ω) varies. Background density is $\rho_0 = 130.0$. Each histogram is compiled from 400 realizations.

both a function of density and a variation parameter, properly choosing the fundamental diagram to produce useful predictions is a difficult task.

3.3 Stochastic Extension to LWR with Density Dependent Coefficients

In Section 3.2 we chose a characteristic length ρ_{ref}^{-1} , a characteristic time δ , and covariances σ^2 , σ_x^2 , σ_t^2 to obtain corresponding parameters κ , η , and τ^z . However, the length scale upon which we expect variation is the distance between drivers, not a fixed length. To remedy this, we choose σ^2 , σ_x^2 , σ_t^2 , and require

$$\sigma^2 = \lim_{t \rightarrow \infty} \mathbb{E} z(x, t) z(x, t) \quad (3.24a)$$

$$\sigma_x^2 = \lim_{t \rightarrow \infty} \mathbb{E} z(x, t) z\left(x + \frac{1}{\rho}\right) \quad (3.24b)$$

$$\sigma_t^2 = \lim_{t \rightarrow \infty} \mathbb{E} z(x, t) z(x, t + \delta). \quad (3.24c)$$

(Recall ρ^{-1} is mean distance between vehicles.) To satisfy these conditions we need

$$\sigma^2 = \frac{\eta^2}{4} \sqrt{\frac{\tau^z}{\kappa}} \quad (3.25a)$$

$$\sigma_x^2 = \frac{\eta^2}{4} \sqrt{\frac{\tau^z}{\kappa}} \exp\left(-\frac{1}{\sqrt{\tau^z \kappa}} \frac{1}{\rho}\right) \quad (3.25b)$$

$$\sigma_t^2 = \frac{\eta^2}{4} \sqrt{\frac{\tau^z}{\kappa}} \left(1 - \text{erf}\left(\sqrt{\frac{\delta}{\tau^z}}\right)\right); \quad (3.25c)$$

accomplishing this will require at least one of the ‘parameters’ to depend on density. We chose to make κ depend on density by introducing new constants η' and κ' such that

$$\eta = \eta' \sqrt{\frac{\rho_{\text{ref}}}{\rho}} \quad (3.26)$$

$$\kappa = \kappa' \left(\frac{\rho_{\text{ref}}}{\rho}\right)^2. \quad (3.27)$$

There are two degrees of freedom among these three constants. The advantages of including ρ_{ref} are to maintain the expected units and to make it simple to relate κ' and η' to κ and η in Section 3.2 at a fixed density. In other words, we can adapt parameter sets from Section 3.2 using this nominal density. This change results in fewer oscillations in regions of low density; this is not only more representative of the smaller number of drivers in those regions, but also leads to somewhat better behaved results.

3.3.1 Numerical Methods

Only minor modifications to the approach presented in Section 3.2.3 are required. To ensure stability across hundreds of realizations, a minimum density is imposed for the purposes of computing κ and η . For the entirety of this Chapter that value is $\rho_{\text{floor}} = 1.0$. This minimum is reached extremely infrequently; it is a precaution. To be explicit,

$$\begin{bmatrix} \rho_j^* \\ z_j^* \end{bmatrix} = \begin{bmatrix} \rho_j^n \\ z_j^n \end{bmatrix} - \frac{k}{h} \left(R_{j-\frac{1}{2}} \Lambda_{j-\frac{1}{2}}^+ \boldsymbol{\alpha}_{j-\frac{1}{2}} + R_{j+\frac{1}{2}} \Lambda_{j+\frac{1}{2}}^- \boldsymbol{\alpha}_{j+\frac{1}{2}} \right) \quad (3.28a)$$

$$\rho_j^{n+1} = \rho_j^* \quad (3.28b)$$

$$z_j^{n+1} = z_j^n + \sqrt{\frac{k}{h}} \eta_j^n \xi_j^n - \frac{k z_j^*}{k + \tau z} + \kappa_j^n \frac{k}{h^2} (z_{j-1}^* - 2z_j^* + z_{j+1}^*) \quad (3.28c)$$

where

$$\kappa_j^n = \kappa' \left(\frac{\rho_{\text{ref}}}{\max(\rho_j^*, \rho_{\text{floor}})} \right)^2 \quad (3.29)$$

$$\eta_j^n = \eta' \sqrt{\frac{\rho_{\text{ref}}}{\max(\rho_j^*, \rho_{\text{floor}})}}. \quad (3.30)$$

3.3.2 The Ringroad Experiment

Figures 3.11 and 3.13 show example realizations in a periodic domain with moderately high density, and are the variable coefficient analogs of Figures 3.5 and 3.7. Similarly,

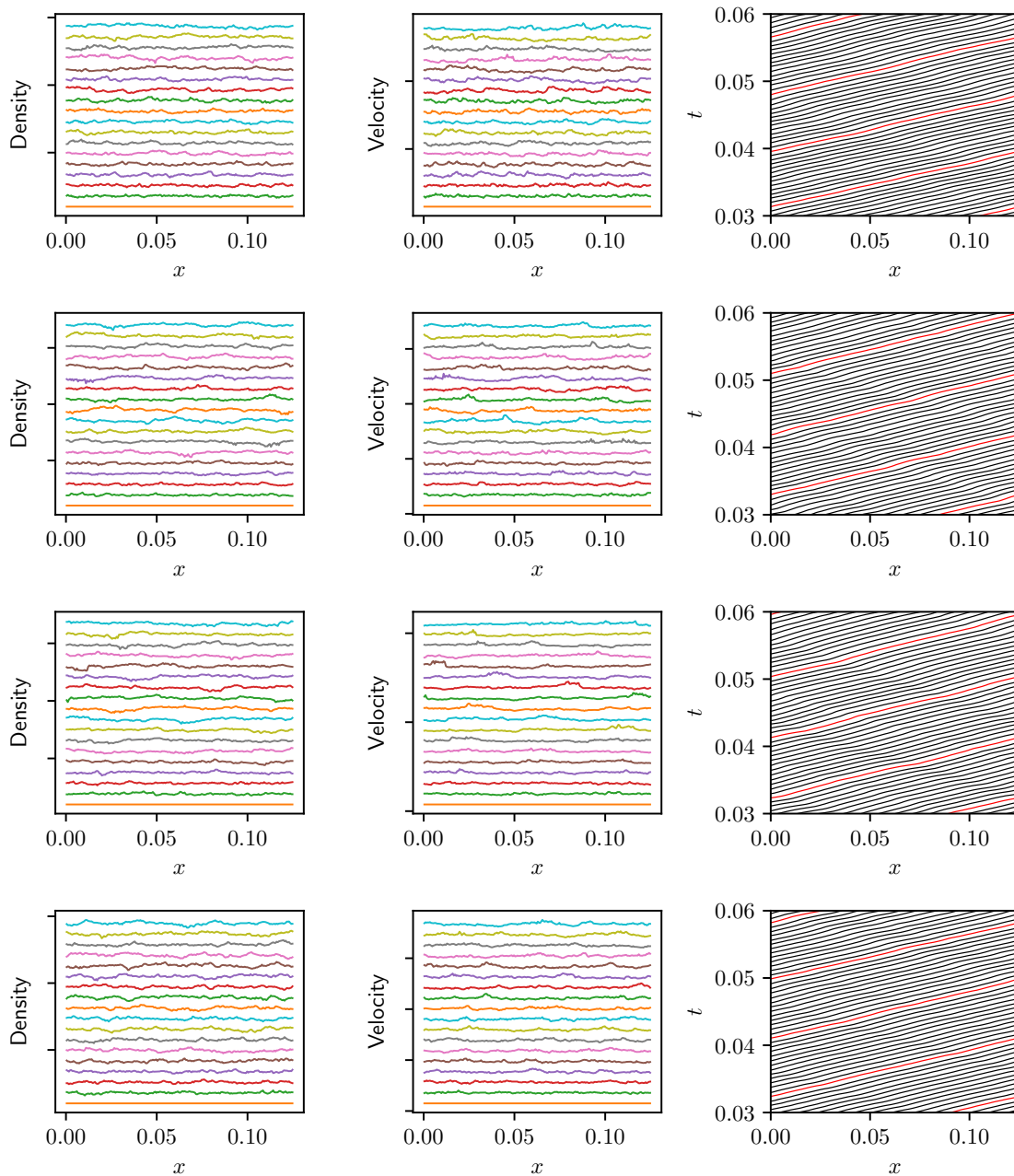


Figure 3.11: Realizations of the ringroad experiment using the LWRZ model (Equation 3.10) with variable coefficients (Equations 3.26 and 3.27). The linearized fundamental diagram (Equation 3.10) with parameters in Table 1.2 was used. The initial density is $\rho_0 = 100.0$ and $\omega = 1.0$. Each row represents an independent realization. The first column shows the density profile at the initial time, and early time, and a later (fully developed time); the second column shows the velocity profile at these times; the third column contains vehicle trajectories.

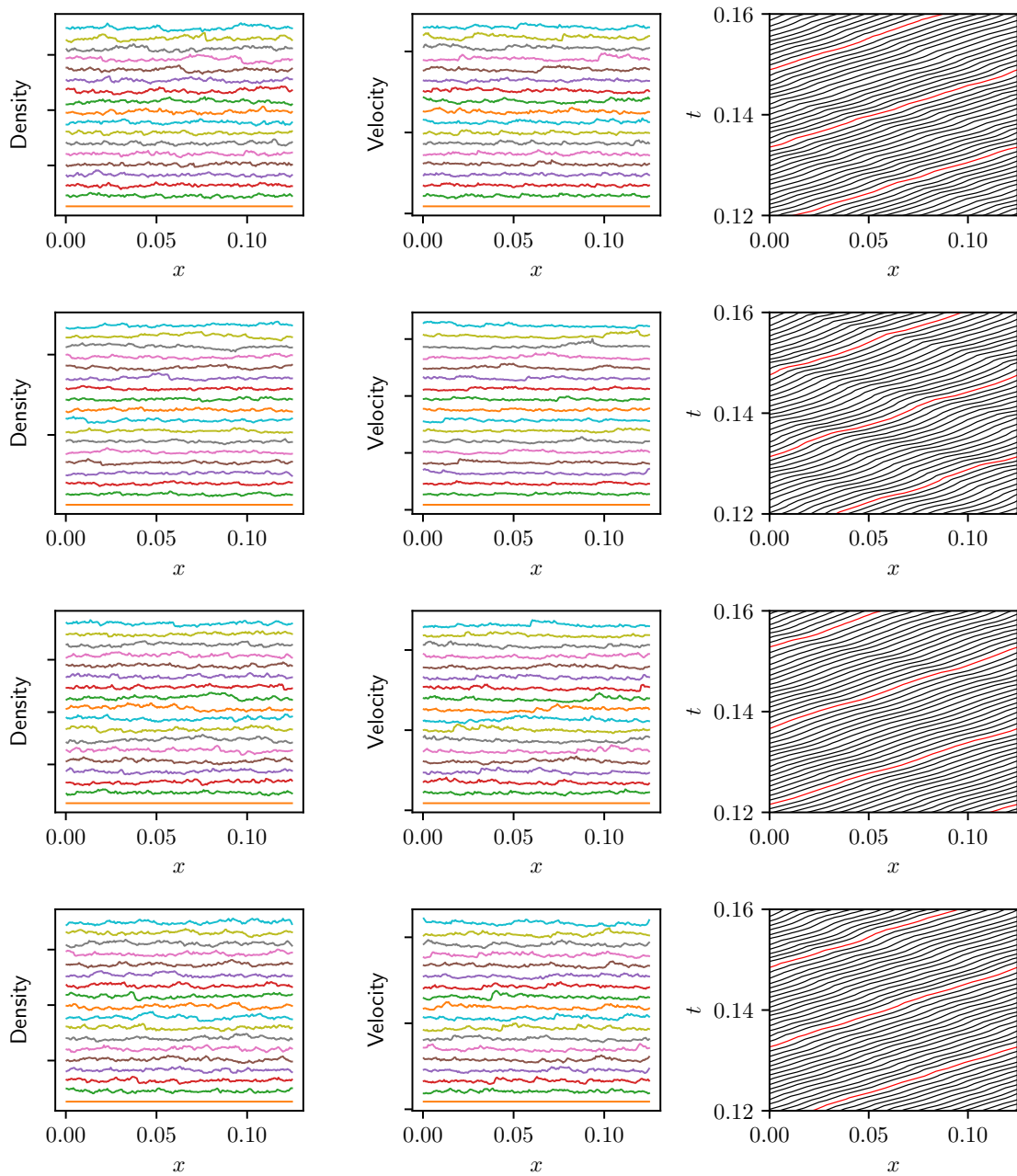


Figure 3.12: Realizations of the ringroad experiment using the LWRZ model (Equation 3.10) with variable coefficients (Equations 3.26 and 3.27). The linearized fundamental diagram (Equation 3.10) with parameters in Table 1.2 was used. The initial density is $\rho_0 = 130.0$ and $\omega = 1.0$. Each row represents an independent realization. The first column shows the density profile at the initial time, and early time, and a later (fully developed time); the second column shows the velocity profile at these times; the third column contains vehicle trajectories.

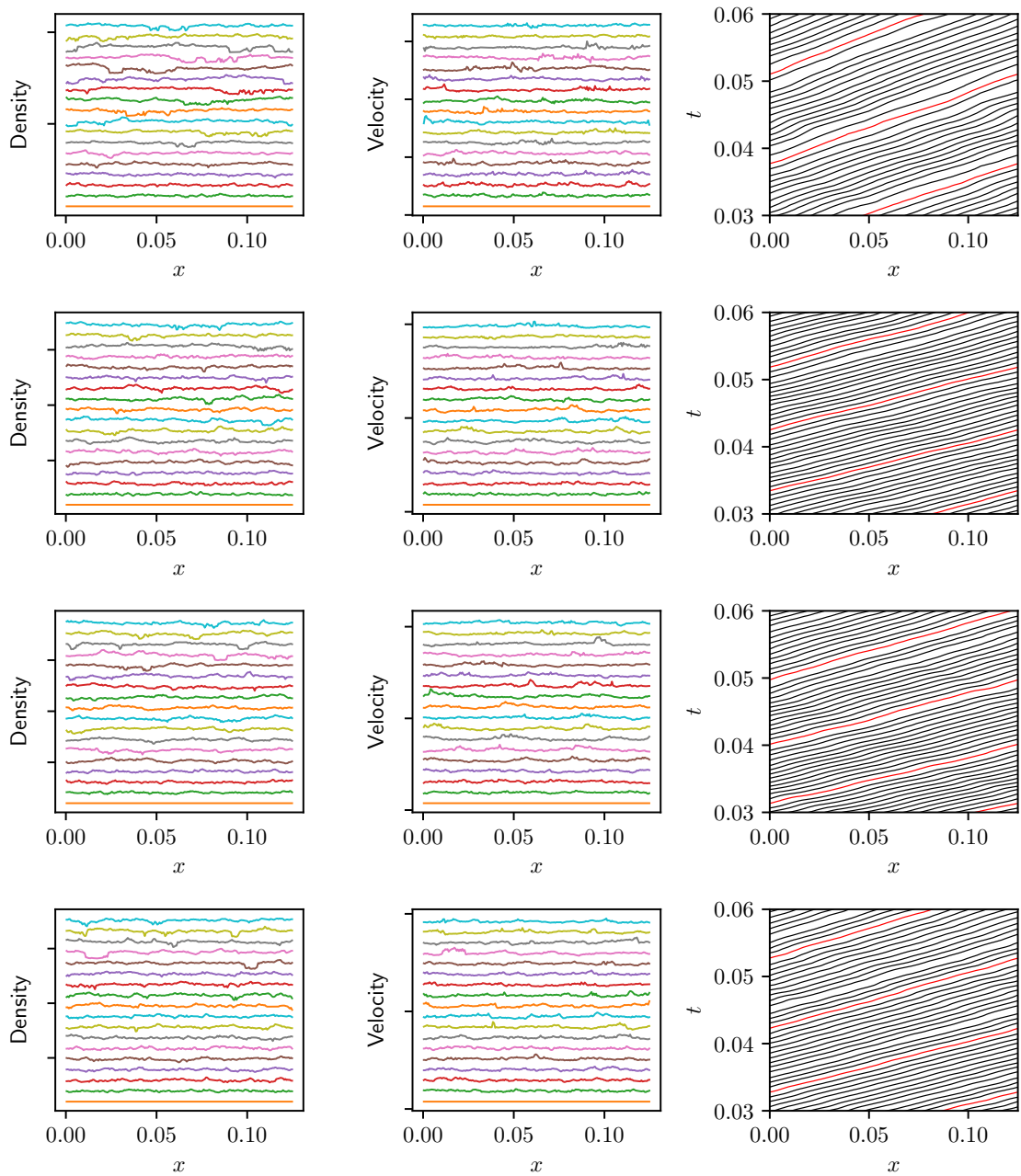


Figure 3.13: Realizations of the ringroad experiment using the LWRZ model (Equation 3.10) with variable coefficients (Equations 3.26 and 3.27). The linearized fundamental diagram (Equation 3.10) with parameters in Table 1.2 was used. The initial density is $\rho_0 = 100.0$ and $\omega = 1.2$. Each row represents an independent realization. The first column shows the density profile at the initial time, and early time, and a later (fully developed time); the second column shows the velocity profile at these times; the third column contains vehicle trajectories.

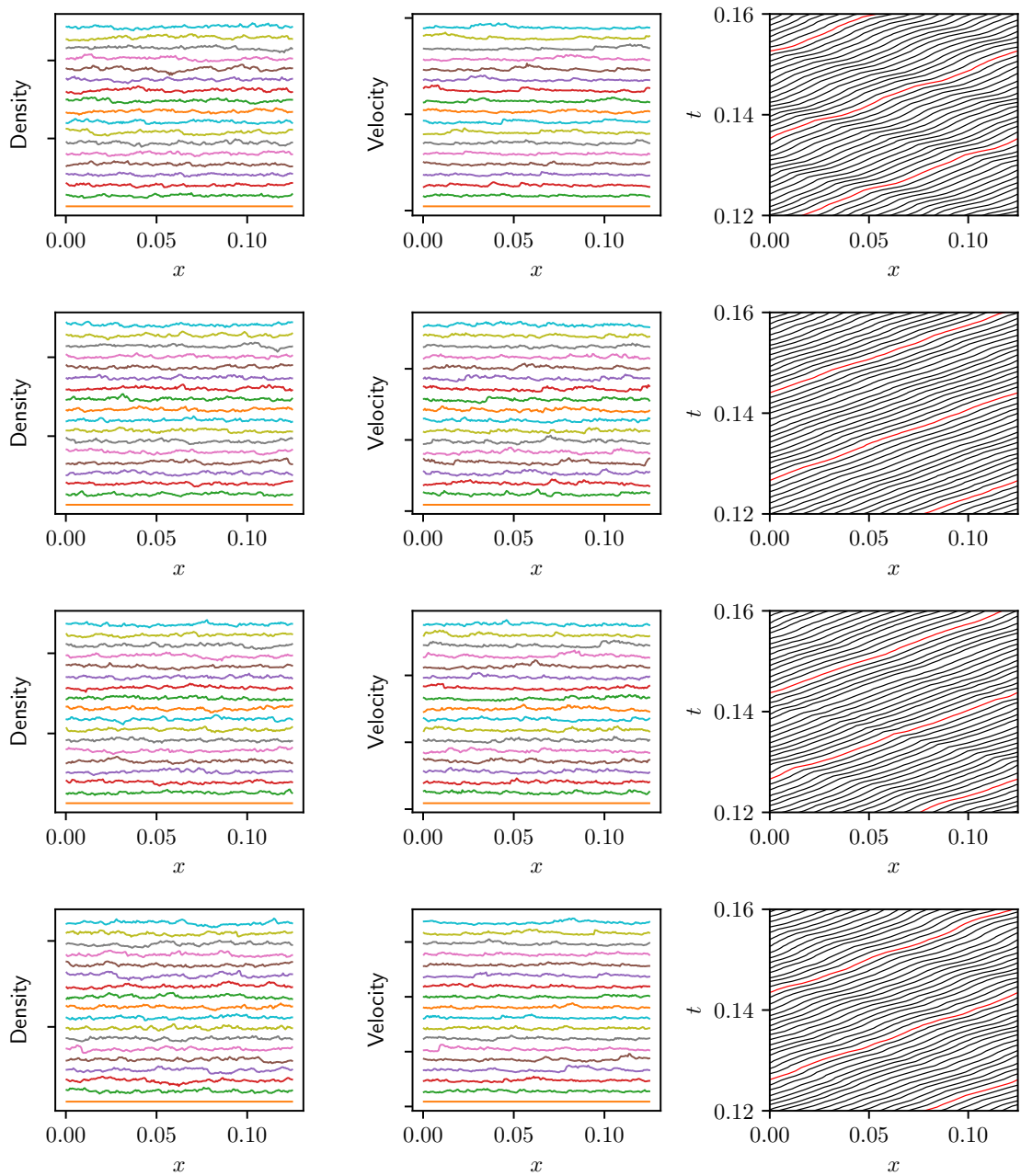


Figure 3.14: Realizations of the ringroad experiment using the LWRZ model (Equation 3.10) with variable coefficients (Equations 3.26 and 3.27). The linearized fundamental diagram (Equation 3.10) with parameters in Table 1.2 was used. The initial density is $\rho_0 = 130.0$ and $\omega = 1.2$. Each row represents an independent realization. The first column shows the density profile at the initial time, and early time, and a later (fully developed time); the second column shows the velocity profile at these times; the third column contains vehicle trajectories.

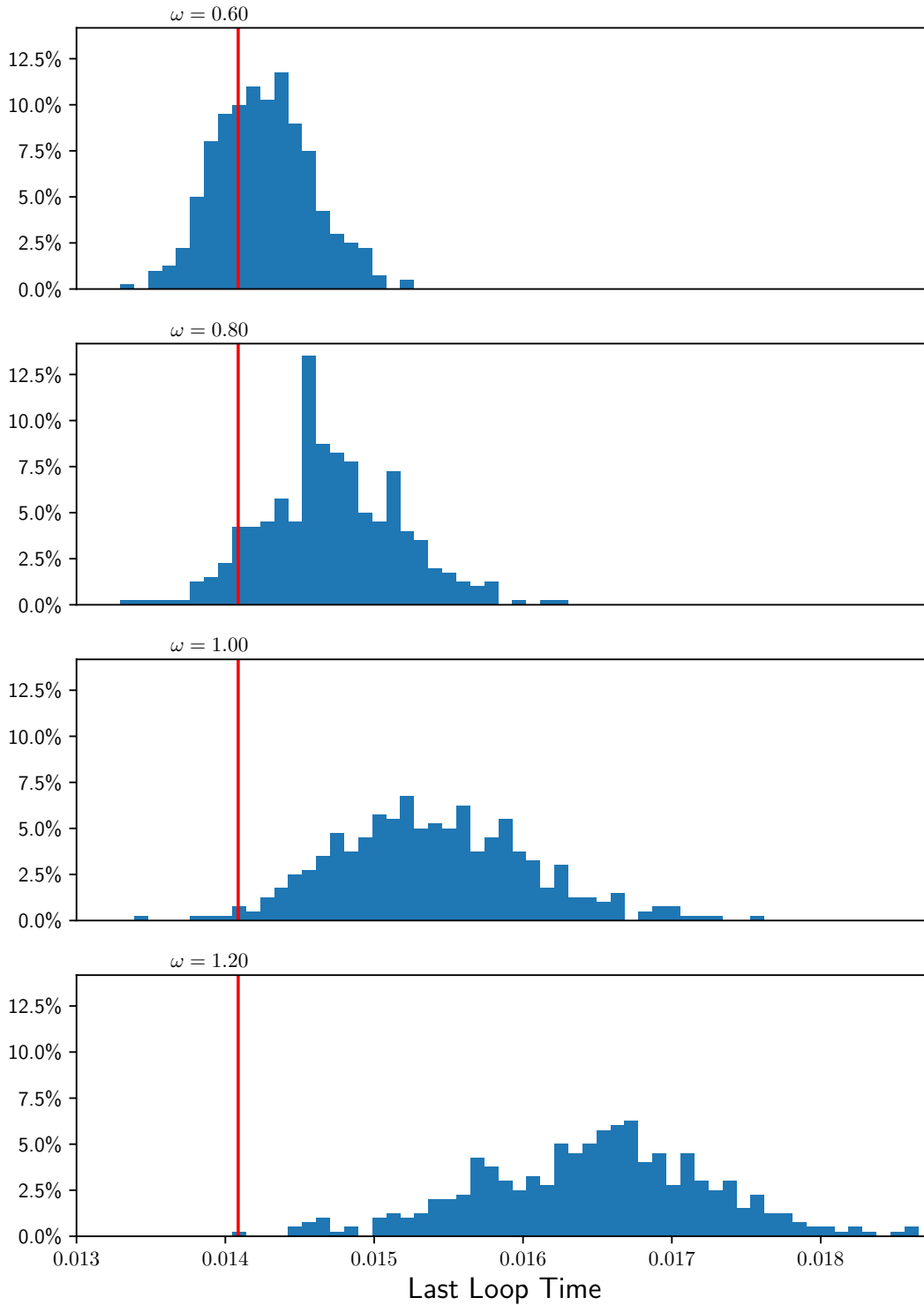


Figure 3.15: Distribution of times taken to traverse the domain immediately before $t = 0.08$ under Equation 3.10 with coefficients varied according to Equations 3.27 and 3.26. The background density is $\rho_0 = 130.0$. Each histogram is compiled from 400 realizations.

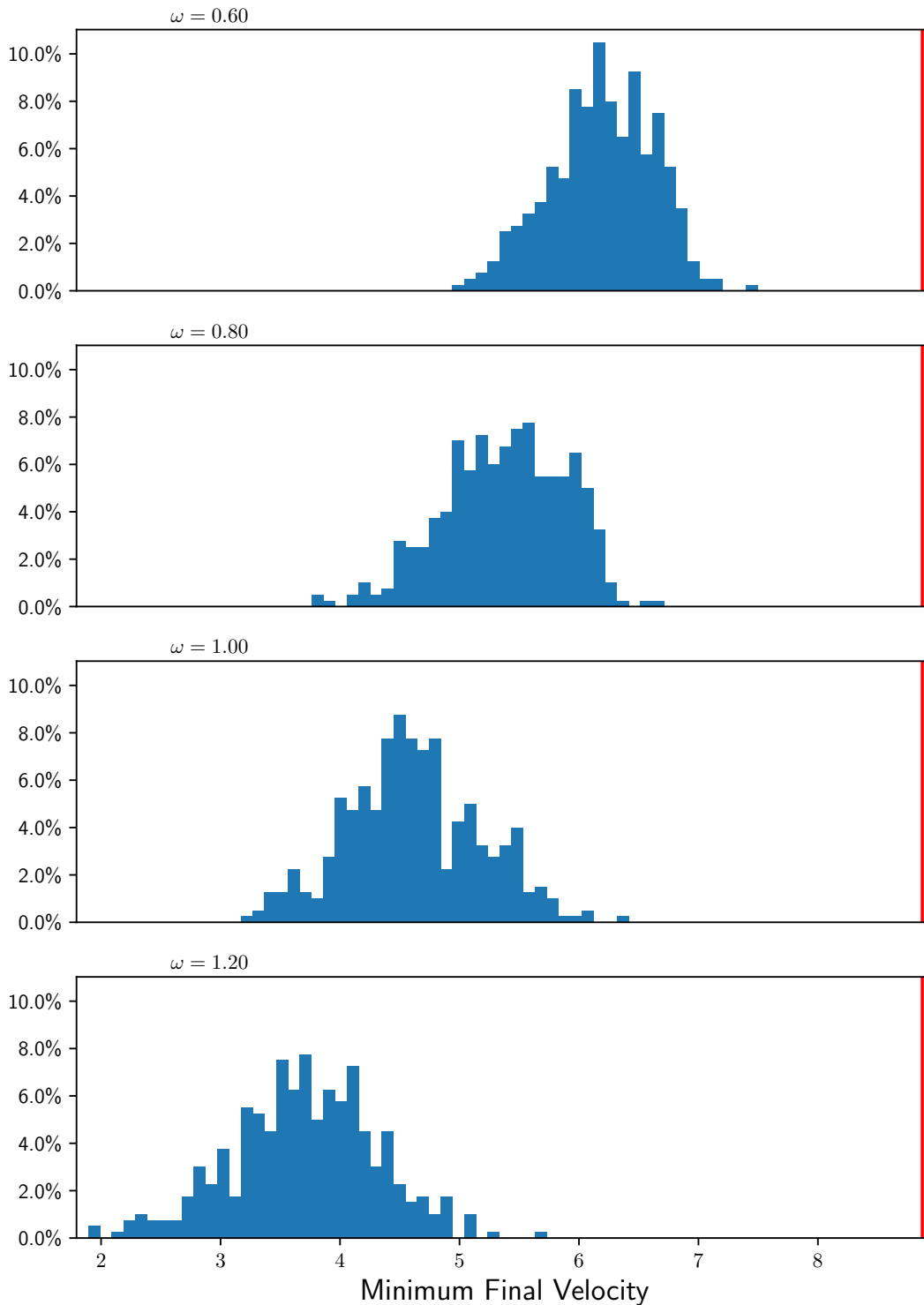


Figure 3.16: Distribution of minimum velocity across the domain at $t = 0.08$ under Equation 3.10 with coefficients varied according to Equations 3.27 and 3.26. The background density is $\rho_0 = 130.0$. Each histogram is compiled from 400 realizations.

Figures 3.12 and 3.14 demonstrate behavior at very high densities and correspond to Figures 3.6 and 3.8 in the constant coefficient case. Variable coefficients clearly produce less variation in low density regions as intended. expected. This leads to slightly more pronounced differences between the high and low density regions that develop from uniform initial conditions. The aggregated results in Figures 3.15 and 3.16 correspond to their constant coefficient counterparts, Figures 3.9 and 3.10. While the trend in transit time (Figure 3.15) is very similar, the distribution of minimum velocities is different. This may be a result of the procedure by which coefficients are varied, but may also be a result of parameters not matching exactly at this density as a result of the chosen reference density ρ_{ref} ; see Equations 3.26 and 3.27 in conjunction with Table 3.1.

3.3.3 The Speed Drop Experiment

Sample realizations of the speed drop experiment can be found in Figure 3.17. These realizations are qualitatively similar to the nominal case (Figure 1.7), with the exception of separation in the downstream (higher density) half of the domain.

Figure 3.18 shows the expected travel time from the left side of the domain to the right hand side of the domain as a function of start time. Here the ‘expected’ time is computed by taking approximate travel times of vehicles spaced ρ^{-1} apart across 40 realizations and projecting them onto a Haar basis with 2^8 basis functions. Though vehicle trajectories for individual realizations look qualitatively similar, we observe significantly increased travel time in realizations as with increased driver inhomogeneity.

3.4 Similarity to Non-Equilibrium Models

There is a difficulty in terminology that arises throughout this work resulting in the use of the terms ‘equilibrium’ and ‘non-equilibrium’ rather than referring to the number of equations (i.e. an n th order model). This may be more of a philosophical distinction than a technical one. Consider Equation 3.10, where the right hand side of the z equation is

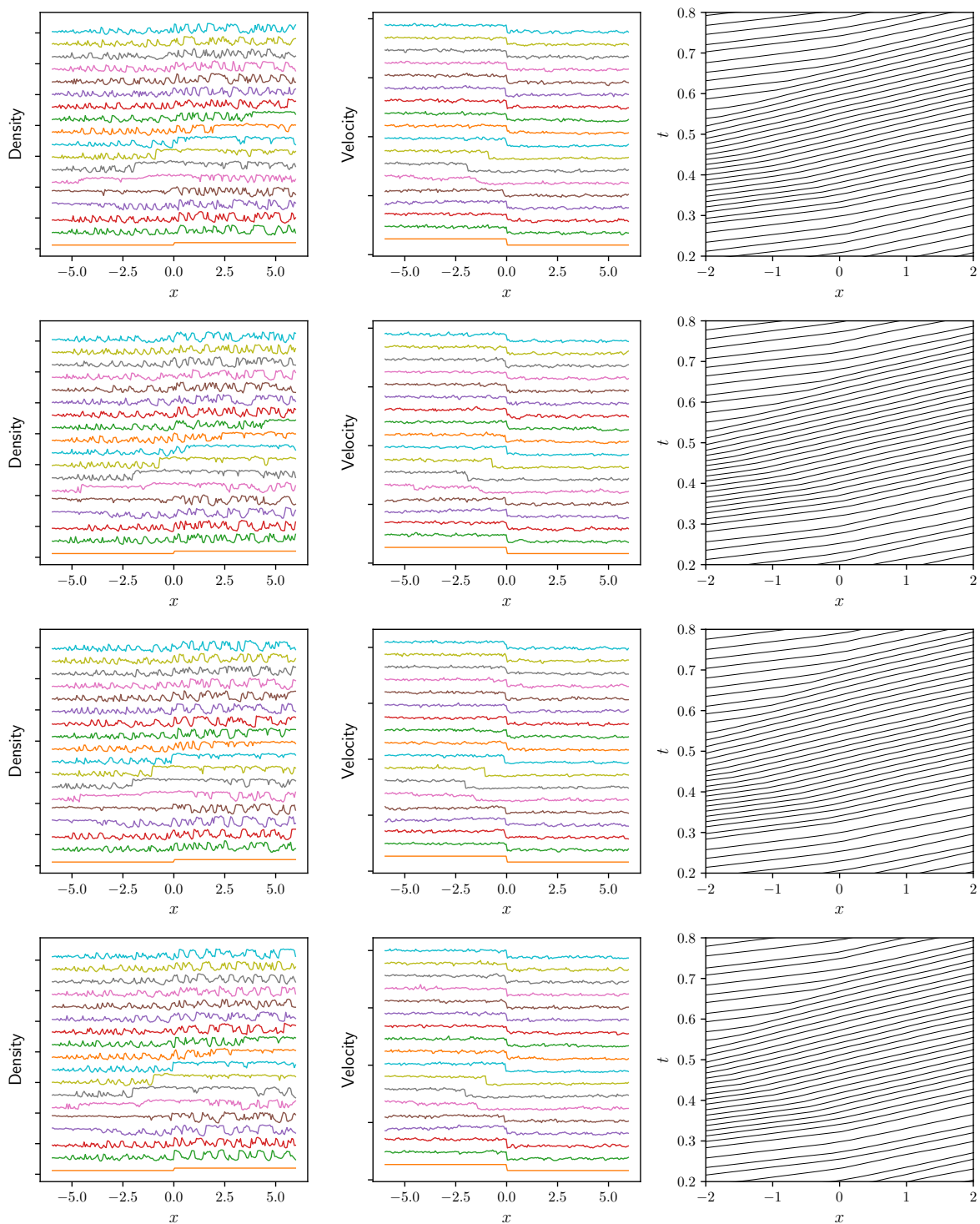


Figure 3.17: Example realizations of the speed drop experiment (Section 1.3.2) using Equation 3.10 with variable coefficients. Here $\omega = 1$.

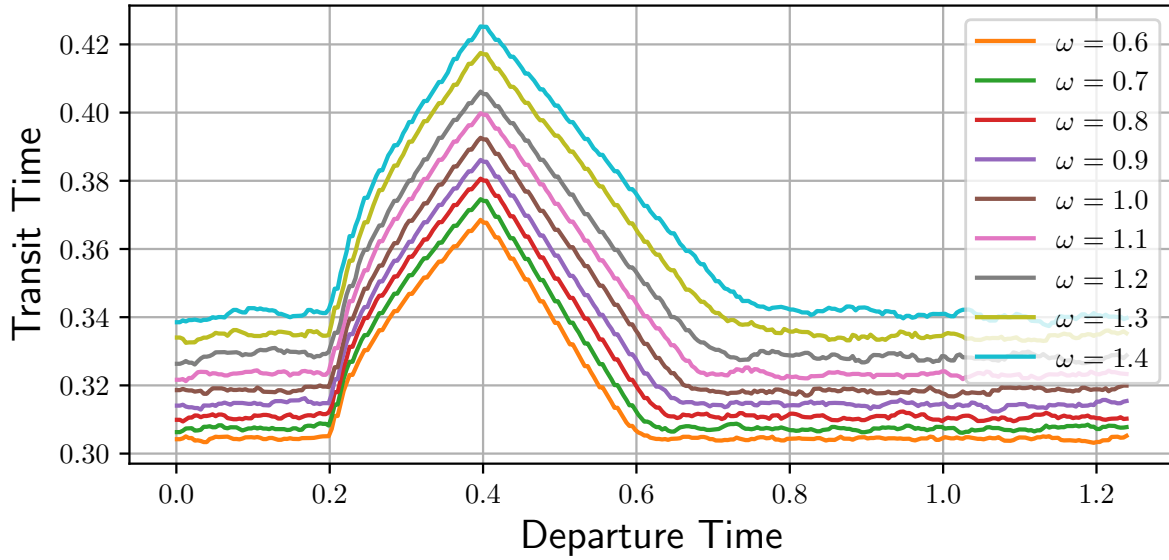


Figure 3.18: Average travel times from the inlet to the outlet of the speed drop experiment as modeled by Equation 3.10 with variable coefficients averaged across 40 realizations per value of ω .

abbreviated by s^z . For the purposes of the present discussion it does not matter whether the coefficients vary with density (Section 3.2) or not (Section 3.3). Because

$$V_t = \rho_t V_\rho + z_t V_z$$

and

$$V_x = \rho_x V_\rho + z_x V_z$$

we have

$$\begin{aligned}
V_t &= \underbrace{-(\rho V)_x}_{\rho_t} V_\rho + \underbrace{(s^z - V z_x)}_{z_t} V_z \\
&= -(\rho V)_x V_\rho - V V_z z_x + s^z V_z \\
&= -\rho V_\rho V_x - V V_\rho \rho_x - V V_z z_x + s^z V_z \\
&= -V \underbrace{(V_\rho \rho_x + V_z z_x)}_{V_x} - \rho V_\rho V_x + s^z V_z \\
&= -(V + \rho V_\rho) V_x + s^z V_z.
\end{aligned} \tag{3.31}$$

We can then introduce the variable $v = V$ and write

$$\begin{aligned}
\rho_t + (\rho v)_x &= 0 \\
v_t + (v + \rho V_\rho) v_x &= V_z s^z
\end{aligned} \tag{3.32}$$

If we use the linearized fundamental diagram (Equation 1.21), then $V(\rho, z) = V_0(\rho) + zV_1(\rho)$; this allows us to compute

$$z = \frac{v - V_0(\rho)}{V_1(\rho)}. \tag{3.33}$$

The Jacobian matrix for this system is

$$\begin{bmatrix} v & \rho \\ 0 & v + \rho V_\rho \end{bmatrix} \tag{3.34}$$

with eigenvalues $\lambda_1 = v + \rho V_\rho < \lambda_2 = v$, eigenvectors

$$\mathbf{r}_1 = \begin{bmatrix} 1 \\ V_\rho \end{bmatrix}, \quad \mathbf{r}_2 = \begin{bmatrix} 1 \\ 0 \end{bmatrix}. \tag{3.35}$$

This is remarkably similar to the non-equilibrium models of Section 4.1, especially the model by Aw, Rascle, and Zhang in Section 4.3. In light of this one could argue that this is really a non-equilibrium model with a perturbation. If this is the case, then we should more critically examine the perturbation we make in the form of a non-equilibrium model. This will be discussed in Section 5.2.

3.5 Higher Dimensional Representations of Driver Variation

It is possible that a single variable is not sufficient to capture the multitude of manners in which drivers may deviate from the mean fundamental diagram. There is no reason z needs to be a single variable. Instead we may have

$$\begin{aligned} \rho_t + (\rho V(\rho, \mathbf{z}))_x &= 0 \\ \mathbf{z}_t + V(\rho, \mathbf{z})\mathbf{z}_x &= -T\mathbf{z} + \nabla \cdot (M\nabla\mathbf{z}) + E d\mathbf{W} \end{aligned} \tag{3.36}$$

where $\mathbf{z} \in \mathbb{R}^N$, $T \in \mathbb{R}^{N \times N}$, $K \in \mathbb{R}^{N \times N}$, an $E \in \mathbb{R}^{N \times N}$. In the simplest case $T = \tau^z I$, $K = \kappa I$, and $E = \eta I$, yielding N identical processes z_1, z_2, \dots, z_N with independent source terms, but this need not be the case. Utilizing equations of the form Equation 3.36 is not substantially more difficult numerically than Equation 3.10, but finding parameters for such an equation would require a different approach for finding a fundamental diagram and coefficients.

3.6 Conclusion

In this chapter we have modified LWR (Equation 1.7) by introducing dependence upon an additional behavior parameter z in the fundamental diagram (Section 1.2). This behavior parameter is governed by a stochastic heat equation (Chapter II) coupled to the LWR system. In the second equation constant coefficients as well as coefficients that preserve a density-dependent length scale were introduced. The resulting models (Equation 3.10) are capable of evolving large stop-and-go traffic patterns, and these patterns persist over time. Realizations

demonstrate consistent qualitative behavior. Transit efficiency is, in general, decreased as inhomogeneities in behavior (as controlled by ω) increase.

CHAPTER IV

Non-Equilibrium Traffic Models

The models referred to here as ‘non-equilibrium’, correspond to ‘second order’ models in the traffic literature. In these models the velocity $v = v(x, t)$ is an additional dependent variable that does not instantaneously adapt to a mean (equilibrium) velocity for that density. The modern study of non-equilibrium macroscopic traffic models follows from Daganzo’s requirements for such models [11], Aw and Rascle’s response [2], and the following discourse [26, 68, 67]. Aw and Rascle required hyperbolicity, boundedness, anisotropy—that waves may not travel faster than traffic velocity, and wave structure—that braking must cause shock waves and acceleration must cause rarefaction waves. Shortly thereafter, Helbing developed models that include a velocity variance [24, 25]. A discussion of stability and wave speeds for non-equilibrium models followed [26, 68].

One way to arrive at an acceleration equation is to rewrite LWR (Equation 1.7) in terms of velocity. First, we compute

$$\begin{aligned}(V(\rho))_t &= V'(\rho)\rho_t \\ &= -V'(\rho)(\rho V(\rho))_x \\ &= -\rho V'(\rho)(V(\rho))_x - V(\rho) \underbrace{(V'(\rho)\rho_x)}_{(V(\rho))_x} \\ &= -(V(\rho) + \rho V'(\rho))(V(\rho))_x.\end{aligned}$$

Should the fundamental diagram have an inverse $\rho(v) = V^{-1}(v)$ (which by Section 1.2 is likely) we can obtain an analogous equation for velocity $v = V(\rho)$:

$$v_t + (v + \rho(v)V'(\rho(v)))v_x = 0. \quad (4.1)$$

Equation 4.1 is equivalent to LWR for smooth solutions, but does not ensure mass conservation in the general case. We will find that many non-equilibrium models, especially the form proposed by Zhang (see Section 4.10), closely mirror equilibrium dynamics.

Most of the models we will consider are derived from a car following analog. Most, with the notable exception of Payne and Whitham's model (Section 4.2), fit into a common framework for which much of the analysis may be shared. For this reason we will begin with a discussion of non-equilibrium models in continuum non-equilibrium models in some generality (Section 4.1), then discuss the non-equilibrium models we to be extended in Chapter V. A discussion of (microscopic) car-following models can be found in Appendix A.

4.1 General Form for Non-Equilibrium Models

Requiring adherence to some established principles of traffic modeling reduces the selection of a second order traffic model to a few constrained choices. What follows is similar in spirit to Zhang [67], but rather than setting out to find a sensible non-equilibrium traffic model, we are setting out to find the form of all sensible second order traffic models. We begin by requiring conservation of mass (Equation 1.5). Noting velocity is not a conserved quantity, requiring velocity relaxes to a fundamental diagram, and requiring the system to be hyperbolic yields the general form

$$\begin{bmatrix} \rho_t \\ v_t \end{bmatrix} + \begin{bmatrix} v & \rho \\ C & B \end{bmatrix} \begin{bmatrix} \rho_x \\ v_x \end{bmatrix} = \begin{bmatrix} 0 \\ \frac{V(\rho)-v}{\tau^v} \end{bmatrix} \quad (4.2)$$

where τ^v is a relaxation time. The wave speeds of this system are

$$\lambda_{\mp} = \frac{1}{2} \left(v + B \mp \sqrt{(v - B)^2 + 4C\rho} \right). \quad (4.3)$$

For the system to be hyperbolic, the wave speeds must be real, i.e.

$$(v - B)^2 + 4C\rho \geq 0. \quad (4.4)$$

To have no wave travel faster than the speed of traffic it is required

$$\begin{aligned} v + B + \sqrt{(v - B)^2 + 4C\rho} &\leq 2v \\ \implies \sqrt{(v - B)^2 + 4C\rho} &\leq v - B \\ \implies (v - B)^2 + 4C\rho &\leq (v - B)^2 \\ \implies 4C\rho &\leq 0 \\ \implies C &\leq 0. \end{aligned} \quad (4.5)$$

$$(4.6)$$

The combination of this fact and Equation 4.4 leads to the necessary condition

$$-\frac{(v - B)^2}{4\rho} \leq C \leq 0. \quad (4.7)$$

The author is not aware of a traffic model that is hyperbolic and satisfies the anisotropy condition for all (ρ, v) that chooses $C \neq 0$. If $C = 0$, Equation 4.5 requires

$$v - B \geq 0 \iff B \leq v. \quad (4.8)$$

With the exception of Payne and Whitham (Section 4.2), all the models we will consider

can be written in the form

$$\rho_t + (\rho v)_x = 0 \tag{4.9a}$$

$$v_t + (v - g)v_x = \frac{V(\rho) - v}{\tau^v} \tag{4.9b}$$

where $g > 0$ is a function that varies between specific non-equilibrium models. In none of the models considered here does g depend on velocity. Writing second order models in this form allows us to be more concise in our description and comparison.

Though there is no conserved analog to momentum, it is sometimes useful to have an explicit flux. Equation 4.9b corresponds to a conservation form proposed by Aw and Rascle [2] as well as Zhang [67] (see Section 4.3)

$$\begin{aligned} \rho_t + (\rho v)_x &= 0 \\ (\rho(v + p))_t + (\rho v(v + p))_x &= \rho \left(\frac{V(\rho) - v}{\tau^v} \right) \end{aligned} \tag{4.10}$$

where p , typically called ‘traffic pressure’, is given by

$$p(\rho) = \int^{\rho} \frac{g(r)}{r} dr. \tag{4.11}$$

‘Traffic pressure’ is a velocity, also sometimes called a ‘hesitation function’ [14].

4.1.1 Properties of the Hyperbolic Part

Consider the homogeneous version of Equation 4.9

$$\begin{bmatrix} \rho_t \\ v_t \end{bmatrix} + \underbrace{\begin{bmatrix} v & \rho \\ 0 & v - g \end{bmatrix}}_A \begin{bmatrix} \rho_x \\ v_x \end{bmatrix} = \begin{bmatrix} 0 \\ 0 \end{bmatrix}. \tag{4.12}$$

Eigenvalues of A are $\lambda_1 = v - g \leq \lambda_2 = v$; for any $g \geq 0$ the anisotropy condition is satisfied. The matrix of corresponding eigenvectors is given by

$$R = \begin{bmatrix} \rho & \rho \\ -g(\rho) & 0 \end{bmatrix}. \quad (4.13)$$

Again, let

$$\Lambda = \begin{bmatrix} \lambda_1 & 0 \\ 0 & \lambda_2 \end{bmatrix}. \quad (4.14)$$

Linearity of the first wave depends on the choice of g ;

$$\mathbf{r}_1 \cdot \nabla \lambda_1 = -\rho \frac{\partial g}{\partial \rho} - g + g \frac{\partial g}{\partial v}. \quad (4.15)$$

The second wave is linearly degenerate as

$$\mathbf{r}_2 \cdot \nabla \lambda_2 = 0. \quad (4.16)$$

Traffic models should produce rarefaction waves in the case of accelerating traffic and shock waves and in the case of braking [2]. Song [59] showed the condition

$$\mathbf{r}_1 \cdot \nabla \lambda_1 < 0 \quad (4.17)$$

is required for this behavior. Many of the choices for g we will consider are of the form

$$g(\rho) = a\rho^\gamma + b \quad (4.18)$$

Table 4.1: Common formulas for $g(\rho)$ for traffic models in the form of Equation 4.9.

in terms of ‘traffic pressure’	$g(\rho) = \rho p'(\rho)$
Aw and Rascle [2]	$g(\rho) = \gamma \rho^\gamma$
Zhang [67]	$g(\rho) = -\rho V'(\rho)$
Song and Karni [59]	$g(\rho) = \frac{1}{\tau v} \left(\frac{s_{\min}^i \rho^{\text{jam}}}{\rho} + \ell_c \right)$

where $\gamma \geq -1$, $a \geq 0$, and $b \geq 0$. For these choices we have

$$\mathbf{r}_1 \cdot \nabla \lambda_1 = -a(\gamma \rho^\gamma + \rho^\gamma) - b = -a(\gamma + 1)\rho^\gamma - b \quad (4.19)$$

Aw and Rascle [2] choose $\gamma > 0$ and $b = 0$ in analogy with fluid pressure. Zhang [67] presents a derivation in which $g(\rho) = -\rho V'(\rho)$; for a range of fundamental diagrams of the type in Section 1.2.3 based on the notion of maintaining a constant travel time between vehicles, this has the form of Equation 4.18. Jiang [27] chooses $a = 0$ and $b > 0$ (see Section 4.3). Song and Karni [59] choose $\gamma = -1$ with $b > 0$ (Section 4.4). All of these choices satisfy the condition in Equation 4.17. The two Riemann invariants, i.e. R_k such that $\nabla R_k \cdot \mathbf{r}_k = 0$, are

$$\begin{aligned} R_1 &= v + p \\ R_2 &= v \end{aligned} \quad (4.20)$$

where p is ‘traffic pressure’ (Equation 4.11).

4.1.2 Stability

The stability region for systems in the form of Equation 4.9 can be approximated through the dispersion relation for a linearized system [30, 27, 52]. First, we linearize our equations

around a (constant) equilibrium state

$$\begin{bmatrix} \rho \\ v \end{bmatrix} = \begin{bmatrix} \rho_e \\ v_e \end{bmatrix} + \epsilon \begin{bmatrix} \rho' \\ v' \end{bmatrix} \quad (4.21)$$

where $v_e = V(\rho_e, 0)$. We have

$$\begin{aligned} g(\rho)v_x &= \epsilon g(\rho_e)v'_x + O(\epsilon^2) \\ V(\rho, 0) - v &= \epsilon (V_\rho(\rho_e, 0)\rho' - v') + O(\epsilon^2) \\ (\rho v)_x &= \epsilon(\rho_e v'_x + v_e \rho'_x) + O(\epsilon^2) \end{aligned}$$

resulting in linearized equations

$$\rho'_t + \rho_e v'_x + v_e \rho'_x = 0 \quad (4.22a)$$

$$v'_t + (v_e - g(\rho_e))v'_x = \frac{V_\rho(\rho_e, 0)\rho' - v'}{\tau^v}. \quad (4.22b)$$

From here we will abbreviate

$$c = v_e - g(\rho_e),$$

$$V_\rho = V_\rho(\rho_e, 0).$$

and look for solutions of the form

$$\begin{bmatrix} \rho' \\ v' \end{bmatrix} = \begin{bmatrix} \rho_0 \\ v_0 \end{bmatrix} e^{\gamma t + i k x}. \quad (4.23)$$

We obtain

$$\gamma\rho_0 + \rho_e v_0 i k + v_e \rho_0 i k = 0 \quad (4.24a)$$

$$\gamma v_0 + c v_0 i k = \frac{V_\rho \rho_0 - v_0}{\tau^v}. \quad (4.24b)$$

Eliminating v_0 yields

$$\gamma^2 + \left((c + v_e) i k + \frac{1}{\tau^v} \right) \gamma + \frac{i k}{\tau^v} (v_e + V_\rho \rho_e) - c v_e k^2 = 0. \quad (4.25)$$

Note ρ_0 is eliminated. Taking $\gamma = a + i b$ and separating real (Equation 4.26a) and imaginary (Equation 4.26b) parts we obtain

$$0 = a^2 - b^2 + \frac{a}{\tau^v} - (c + v_e) k b - c v_e k^2 \quad (4.26a)$$

$$0 = 2ab + (c + v_e) k a + \frac{b}{\tau^v} + \frac{k}{\tau^v} \underbrace{(v_e + V_\rho \rho_e)}_q. \quad (4.26b)$$

Following [30] we take $|a| \rightarrow 0$ to find the boundary of the stability region. Equation 4.26b in the $|a| \rightarrow 0$ limit yields $b = -kq$, which we substitute into Equation 4.26a:

$$\frac{\rho_0}{\rho_e} = -\frac{V_\rho(\rho_e)\rho_0}{g(\rho_e)}. \quad (4.27)$$

In this step we divide by k^2 ; this excludes the unperturbed case from any determination of instability. See [27] for a similar stability condition. Surprisingly, this condition does not depend on τ^v or ρ_0 ! The numerator of this fraction is $V_\rho(\rho_e)\rho_0 \approx V(\rho_e + \rho_0, 0) - V(\rho_e, 0)$ and the denominator is the wave speed relative to traffic. Loosely speaking, the relative size of the perturbation must be bounded by the response in the fundamental diagram relative to the backward wave speed. A less general result of this type was presented and demonstrated in [27]. A numerical demonstration requires a particular choice of $g(\rho)$; this is postponed until Section 4.4.

4.2 Payne

One of the earliest (1971) second order models derived for traffic flow was proposed by Payne [52]. Payne presented a Taylor expansion of the optimal velocity car-following model (Equation A.2 in Appendix A)

$$\ddot{x}_n = \frac{V((x_{n+1} - x_n)^{-1}) - \dot{x}_n}{T} \quad (4.28)$$

about the point $x = (x_n + x_{n+1})/2$ resulting in the continuum model

$$\rho_t + (\rho v)_x = 0 \quad (4.29a)$$

$$v_t + \frac{V'(\rho)}{2\rho T} \rho_x = \frac{V(\rho) - v}{T}. \quad (4.29b)$$

Interestingly this is an example of a case in which A in Equation 4.2 is nonzero. For hyperbolicity we require (see Equation 4.4)

$$-\frac{V'(\rho)}{2T} \leq \left(\frac{v}{2}\right)^2. \quad (4.30)$$

Because $V'(\rho) \leq 0$, the validity of the model is restricted to a region in the (ρ, v) plane. However, where the model is hyperbolic, it does satisfy the anisotropy condition as

$$\frac{v}{2} \pm \sqrt{\left(\frac{v}{2}\right)^2 + \frac{V'(\rho)}{2T}} \leq v \quad (4.31)$$

($V'(\rho) \leq 0$). Some later works (e.g. the aforementioned [30]) replace $V'(\rho)/(2T)$ with a constant. This simplifies some of the analysis as the resulting equation in terms of ρv becomes linear and the region in which the system is hyperbolic becomes easier to identify. Some later authors (including [30] among others) also included viscous terms in the velocity equation.

4.3 Aw, Rascle, and Zhang

Aw and Rascle [2] arrive at Equation 4.10 using an analogy to fluid pressure, initially presenting it in the non-conservative form

$$(v + p)_t + v(v + p)_x = 0 \quad (4.32)$$

where the velocity $p = p(\rho)$ is called a ‘traffic pressure.’ Zhang [67] obtains nearly the same model by beginning with the proportional control car-following model (Equation A.1 in Appendix A)

$$\ddot{x}_n = \frac{\dot{x}_{n+1} - \dot{x}_n}{T} \quad (4.33)$$

and asserting that the ‘traffic sound speed’ is $g(\rho) = -\rho V'(\rho)$ as it is in the equilibrium case (Equation 1.10). Moreover, Zhang asserts

$$V'(\rho) = -\frac{1}{\rho^2 T}. \quad (4.34)$$

The family of fundamental diagrams in which a constant time headway or constant time to traverse the intervehicle space is maintained (e.g. Section 1.2.3) have the form

$$V(\rho) = \frac{a}{\rho} - b \quad (4.35)$$

where $a > 0$ and $b \geq 0$. Zhang’s proposed wave speed (Equation 4.34) is consistent with this family of fundamental diagrams. From Equation 4.11 we obtain the corresponding traffic pressure $p(\rho) = -V(\rho)$. Both authors present a model in which the deviation from some density dependent velocity is advected (Equation 4.32). Aw and Rascle chose to advect deviations from a traffic ‘pressure’ $p(\rho) = \rho^\gamma$, but did not claim this was necessarily the correct relation. Zhang chose to advect deviations from the equilibrium velocity (fundamental diagram). Aw and Rascle impose $p \sim \rho^\gamma$ as $\rho \rightarrow 0$ and $\rho p'' + 2p' > 0$ (convexity of ρp); this

condition is not met for constant sound speed.

It could also be argued that the models of Chapter III are in this same spirit. Not only is z an advected variable representing deviation from mean or equilibrium behavior, but it was shown in Section 3.4 that, for certain forms of $V(\rho, z)$, very similar equations are obtained. The possibility of relaxation toward an equilibrium velocity was acknowledged but not explored by Aw and Rascle. The omission of relaxation toward an equilibrium velocity was intentional by Zhang, as it allows propagation of non-decaying non-equilibrium structures [67]. We will include a relaxation toward the equilibrium velocity in all non-equilibrium models.

4.4 Song and Karni

Jiang [27, 28] proposed the ‘full velocity difference’ car-following model discussed in Appendix A along with the corresponding continuum model that is the topic of this section. The approach taken by Jiang arrives at the model

$$\rho_t + (\rho v)_x = 0 \tag{4.36a}$$

$$v_t + (v - c_0)v_x = \frac{V(\rho) - v}{\tau v} \tag{4.36b}$$

whereas Song [58, 59] arrived at

$$\rho_t + (\rho v)_x = 0 \tag{4.37a}$$

$$v_t + \left(v - \frac{h(\rho)}{\tau h} \right) v_x = \frac{V(\rho) - v}{\tau v} \tag{4.37b}$$

where headway $h(\rho)$ is given by

$$h(\rho) = \frac{s_{\min}^i \rho^{\text{jam}}}{\rho} + \ell_c \tag{4.38}$$

where s_{\min}^i is the minimum *intervehicle* spacing, ℓ_c is the length of a vehicle, and τ^h is a reaction time. Equation 4.36 is an instance of Equation 4.9 with

$$g(\rho) = \frac{1}{\tau^h} \left(\frac{\rho^{\text{jam}} s_{\min}^i}{\rho} + \ell_c \right). \quad (4.39)$$

Equation 4.37 is based on a Taylor expansion of Equation 4.36 [58, 59]. Here we will repeat that derivation with attention given to additional terms. Assume there is some smooth extension of the discrete velocities v_{n+1} and v_n such that $v_n = v(x_n(t), t)$. If we expand the velocity difference between the two vehicles we obtain

$$\begin{aligned} v_{n+1} - v_n &= \left(v_n + h\partial_x v_n + \frac{h^2}{2}\partial_{xx} v_n + \frac{h^3}{6}\partial_{xxx} v_n + \dots \right) - v_n \\ &= h\partial_x v_n + \frac{h^2}{2}\partial_{xx} v_n + \frac{h^3}{6}\partial_{xxx} v_n + \dots \end{aligned} \quad (4.40)$$

where $h = x_{n+1} - x_n$. An evolution equation for the velocity equation can then be found by setting

$$\begin{aligned} \partial_t v + v\partial_x v &\approx \ddot{x}_n \\ &\approx \frac{V(h) - \dot{x}_n}{T} + \frac{\dot{x}_{n+1} - \dot{x}_n}{\tau} \\ &\approx \frac{V(h) - \dot{x}_n}{T} + \frac{1}{\tau} \left(h\partial_x v_n + \frac{h^2}{2}\partial_{xx} v_n + \frac{h^3}{6}\partial_{xxx} v_n + \dots \right) \end{aligned}$$

Song and Karni defined h in a manner not exactly equal to $x_{n+1} - x_n = \frac{1}{\rho}$ (Equation 4.38). Headway is by definition the distance from one vehicle to the next including the length of one of the two vehicles; the corresponding macroscopic quantity is ρ^{-1} . While Equation 4.38 is not a correct formula for headway in the strict sense it may very well be an excellent representation of *perceived* headway, and produces sensible results in the macroscopic context. If h is taken to be the true headway ρ^{-1} , then the viscosity varies as ρ^{-2} . This mirrors the viscous scaling from Section 3.3. Using the relationship given by Equation 4.38, the viscosity

Table 4.2: Parameters used for the model proposed by Song and Karni (Equation 4.37) and its stochastic counterparts (Equation 5.1).

τ^v	0.00125
s_{\min}^i	0.000833
ℓ_c	0.0025
ρ^{jam}	300.0
τ^h	0.000125

Table 4.3: Parameters used for the fundamental diagram given by Equation 1.18 in Figure 4.1. These parameters are similar to those used in [27, 59].

v_{\max}	60.0
ρ^{jam}	300.0
c	0.25
w	0.06
k	3.72×10^{-6}

still increases dramatically at low densities.

As an illustration of the stability result in Section 4.1.2, Figure 4.1 shows the quantity

$$\rho_e + \frac{g(\rho_e)}{V_\rho(\rho_e)}$$

evaluated at a variety of densities using the parameters in Table 4.2. A positive value represents a prediction of instability from the linearized analysis (Equation 4.27). Figures 4.2 through 4.4 show corresponding solutions with periodic boundary conditions and a set of small initial disturbances; these are analogs to the figures shown in Jiang [27]. The numerical solutions provide evidence that the linearized analysis is predictive of the development of wave structures. This does not necessarily mean the linearized analysis is predictive of the stochastic modifications of the model to come later, but it does inform our choices in

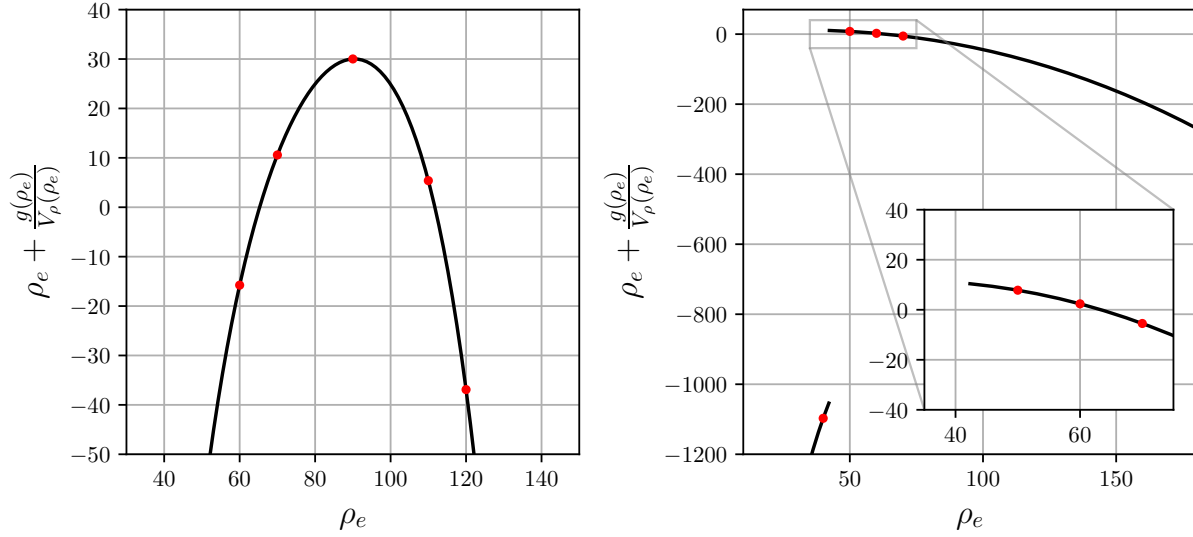


Figure 4.1: Evaluation of $\rho_e + \frac{g(\rho_e)}{V_\rho(\rho_e)}$ for a variety of densities ρ_e , $g(\rho)$ given in Equation 4.39, and fundamental diagrams given by Equation 1.18 (left) and Equation 1.21 (right). Parameters can be found in Tables 4.3, 1.2, and 4.2. The densities appearing in Figure 4.2, Figure 4.3, and Figure 4.4 are marked with red dots.

that regard.

4.5 Numerical Considerations

To compute numerical solutions, we use a linearized Riemann solver. An approximate solution to the linearized Riemann problem [39, 41] is

$$\hat{\mathbf{w}}\left(\frac{x}{t}\right) = \mathbf{u}_l + \sum_{\hat{\lambda}_p \leq \frac{x}{t}} \alpha_p \hat{\mathbf{r}}_p \quad (4.41)$$

where

$$\mathbf{u}_r - \mathbf{u}_l = \sum_p \alpha_p \hat{\mathbf{r}}_p. \quad (4.42)$$

For Equation 4.9 wave strengths α are

$$\boldsymbol{\alpha} = \begin{bmatrix} \alpha_1 \\ \alpha_2 \end{bmatrix} = \underbrace{\begin{bmatrix} 0 & -\frac{1}{g} \\ \frac{1}{\rho} & \frac{1}{g} \end{bmatrix}}_{R^{-1}} \begin{bmatrix} \Delta\rho \\ \Delta v \end{bmatrix} = \begin{bmatrix} -\frac{\Delta v}{g} \\ \frac{\Delta\rho}{\rho} + \frac{\Delta v}{g} \end{bmatrix}. \quad (4.43)$$

The simple average

$$\begin{bmatrix} \bar{\rho} \\ \bar{v} \end{bmatrix} = \frac{1}{2} \left(\begin{bmatrix} \rho_L \\ v_L \end{bmatrix} + \begin{bmatrix} \rho_R \\ v_R \end{bmatrix} \right) \quad (4.44)$$

satisfies

$$\bar{v}\Delta\rho + \bar{\rho}\Delta v = \rho_L v_L - \rho_R v_R, \quad (4.45)$$

preserving the jump condition in density. Because there is no physically conserved quantity involving velocity, there is no reason to preserve any particular jump condition in that field. For all non-equilibrium models in this thesis a simple average will be used.

For the figures in this chapter a second order scheme

$$\begin{aligned} U_j^{n+1} = & U_j^n - \frac{k}{h} \left(R_{j-\frac{1}{2}} \Lambda_{j-\frac{1}{2}}^+ \left(\boldsymbol{\alpha}_{j-\frac{1}{2}} - h\boldsymbol{\beta}_{j-\frac{1}{2}} \right) + R_{j+\frac{1}{2}} \Lambda_{j+\frac{1}{2}}^- \left(\boldsymbol{\alpha}_{j+\frac{1}{2}} - h\boldsymbol{\beta}_{j+\frac{1}{2}} \right) \right) \\ & - \frac{k}{2h} \left(R_{j+\frac{1}{2}} |\Lambda_{j+\frac{1}{2}}| \left(1 - \frac{k}{h} |\Lambda_{j+\frac{1}{2}}| \right) \Phi_{j+\frac{1}{2}} \boldsymbol{\alpha}_{j+\frac{1}{2}} \right. \\ & \left. - R_{j-\frac{1}{2}} |\Lambda_{j+\frac{1}{2}}| \left(1 - \frac{k}{h} |\Lambda_{j+\frac{1}{2}}| \right) \Phi_{j-\frac{1}{2}} \boldsymbol{\alpha}_{j-\frac{1}{2}} \right) \end{aligned} \quad (4.46)$$

where

$$\Phi_{j+\frac{1}{2}} = \begin{bmatrix} \phi_{j+\frac{1}{2},1} & 0 \\ 0 & \phi_{j+\frac{1}{2},2} \end{bmatrix}, \quad (4.47)$$

$$\phi_{j+\frac{1}{2},i} = \begin{cases} \phi\left(\frac{\alpha_{j+\frac{1}{2},i}}{\alpha_{j-\frac{1}{2},i}}\right) & \text{if } \lambda_{j+\frac{1}{2},i} > 0 \\ \phi\left(\frac{\alpha_{j+\frac{1}{2},i}}{\alpha_{j+\frac{3}{2},i}}\right) & \text{if } \lambda_{j+\frac{1}{2},i} < 0 \end{cases}, \quad (4.48)$$

$\alpha_{j+\frac{1}{2},i}$ and $\lambda_{j+\frac{1}{2},i}$ are linearized wave strengths and eigenvalues in the i -th field (i.e. components of $\boldsymbol{\alpha}_{j+\frac{1}{2}}$ and $\Lambda_{j+\frac{1}{2}}$ respectively), $\Lambda_{j+\frac{1}{2}}^+$ (resp. $\Lambda_{j+\frac{1}{2}}^-$) are the element wise maximum (resp. minimum) of $\Lambda_{j+\frac{1}{2}}$ and zero, $|\Lambda_{j+\frac{1}{2}}| = \Lambda_{j+\frac{1}{2}}^+ - \Lambda_{j+\frac{1}{2}}^-$, $\boldsymbol{\beta}_{j+\frac{1}{2}}$ is the projection of the source terms onto the eigenvectors

$$R_{j+\frac{1}{2}}\boldsymbol{\beta}_{j+\frac{1}{2}} = \frac{1}{2} \left(\begin{bmatrix} 0 \\ \frac{V(\rho_j)-v_j}{\tau^v} \end{bmatrix} + \begin{bmatrix} 0 \\ \frac{V(\rho_{j+1})-v_{j+1}}{\tau^v} \end{bmatrix} \right), \quad (4.49)$$

and $\phi(r)$ is the van Leer limiter

$$\phi(r) = \frac{r + |r|}{1 + |r|}. \quad (4.50)$$

4.6 Generalized Second Order Models (GSOM)

Lebacque [37] proposed a framework for the Generic Second Order Model (GSOM), prescribing conservation of mass and advection of an unspecified quantity I :

$$\begin{aligned} \rho_t + (\rho v)_t &= 0 \\ (\rho I)_t + (\rho v I)_x &= 0 \\ v &= \mathcal{F}(\rho, I). \end{aligned} \quad (4.51)$$

For example, the ARZ model (Section 4.3) falls under this framework for $I = v + p(\rho)$ and $\mathcal{F}(\rho, I) = I - p(\rho)$. Though not the intent of this formulation, equilibrium models can be written this way with $\mathcal{F}(\rho, I) = V(\rho)$. It is not specified whether I must be a present driver state or a behavior parameter. For example, in [15, 14], this additional property was representative of the maximum velocity parameterizing a class of fundamental diagrams. The models of Chapter III are in this spirit where $I = z$, $\mathcal{F}(\rho, I) = V(\rho, I)$, and additional source terms and viscosity exist. Another more subtle difference between the models in Chapter III and the GSOM models is that ρI is not conserved in Chapter III; this leaves us free to choose shock speeds other than the one imposed by Equation 4.51. We have chosen to make the meaning of z almost entirely arbitrary as long as it is a monotone change in driver behavior, but other authors have introduced stochastic source terms to the conservation equation for I in other ways [5, 33, 55]. The present work differs in that we argue a more careful selection of stochastic process including viscosity (Chapter II) is required, there is no reason to be concerned with conserving the driver dependent quantity, and the model is improved by making the behavior of the stochastic process dependent upon density (Section 3.3).

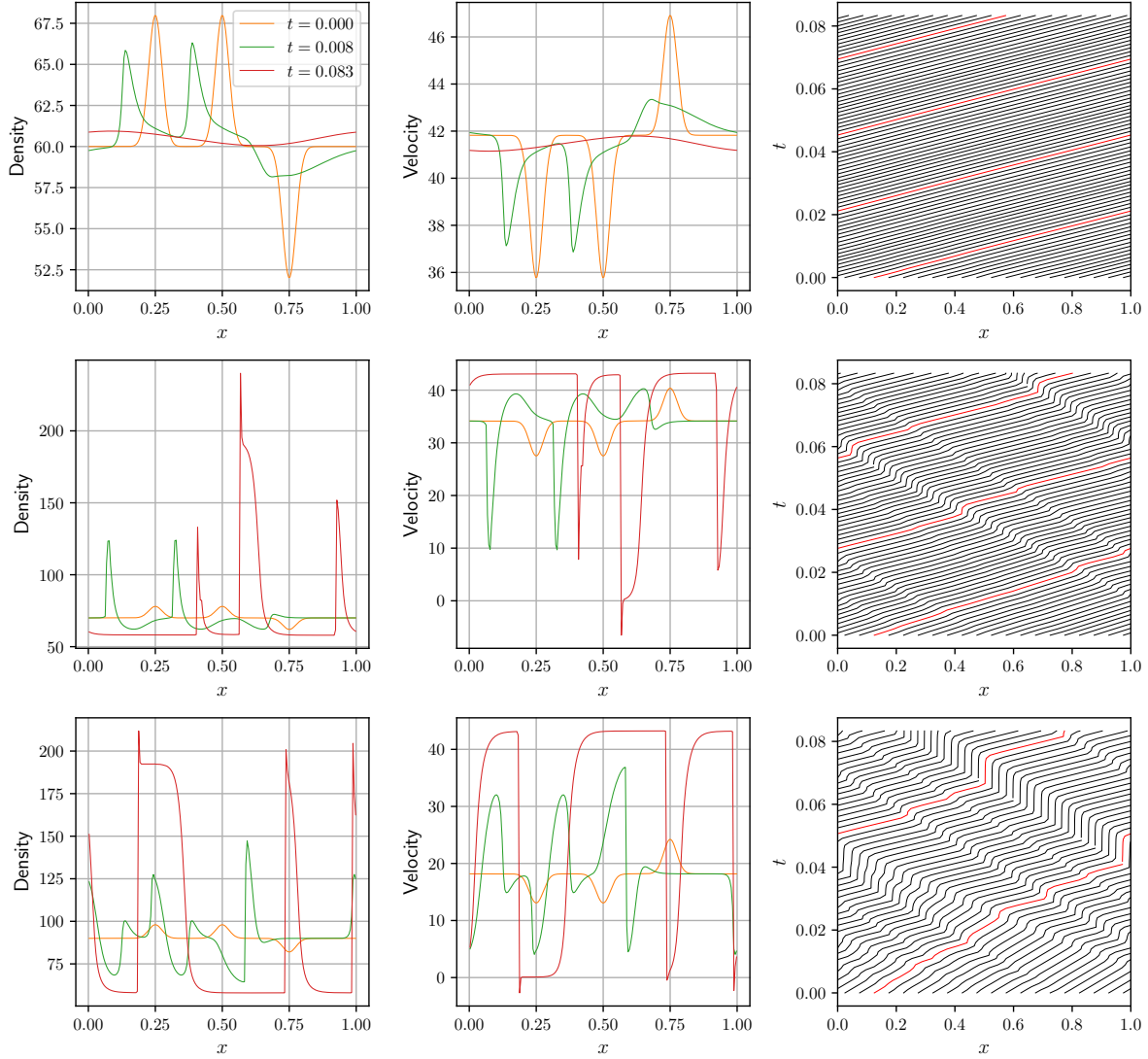


Figure 4.2: Numerical solutions to Equation 4.37 using the fundamental diagram found in Kerner [30] (Equation 1.18), parameters in Tables 4.2 and 4.3, and a small initial disturbance. The mean densities from top to bottom are $\rho_0 = 60.0$, $\rho_0 = 70.0$, and $\rho_0 = 90.0$. Solutions for higher densities are shown in Figure 4.3.

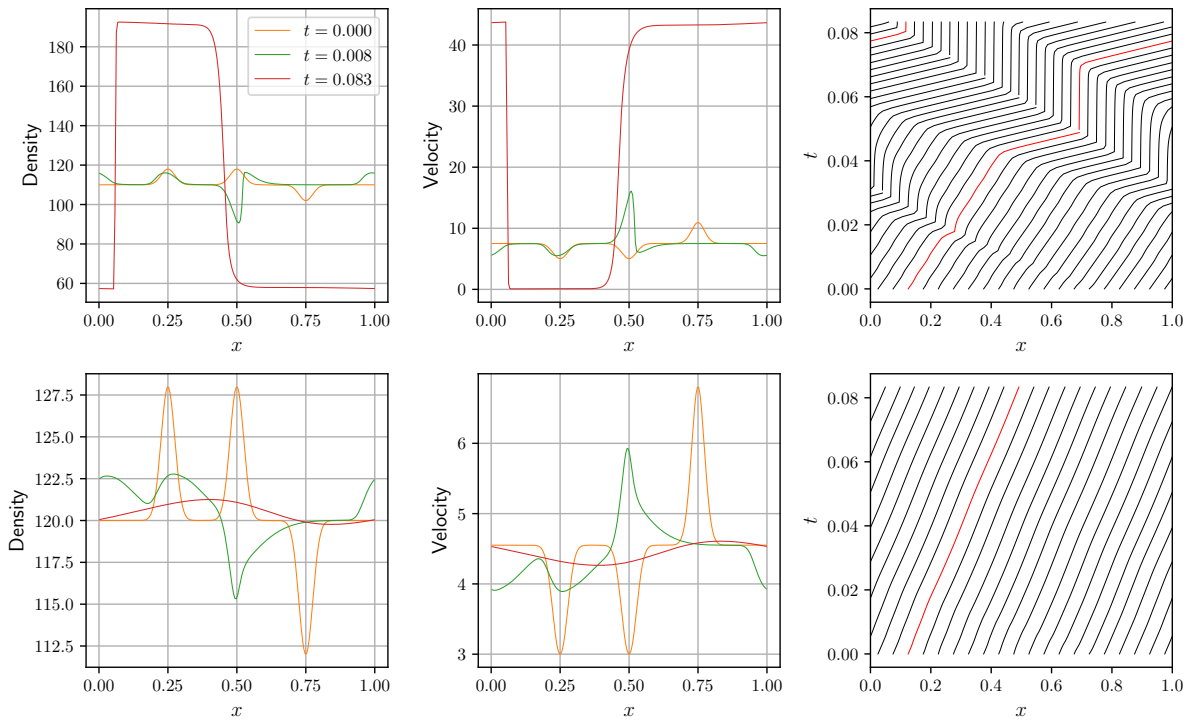


Figure 4.3: Numerical solutions to Equation 4.37 using the fundamental diagram found in Kerner [30] (Equation 1.18), parameters in Tables 4.2 and 4.3, and a small initial disturbance. The mean densities are $\rho_0 = 110.0$ (top) and $\rho_0 = 120.0$ (bottom). For lower densities see Figure 4.2.

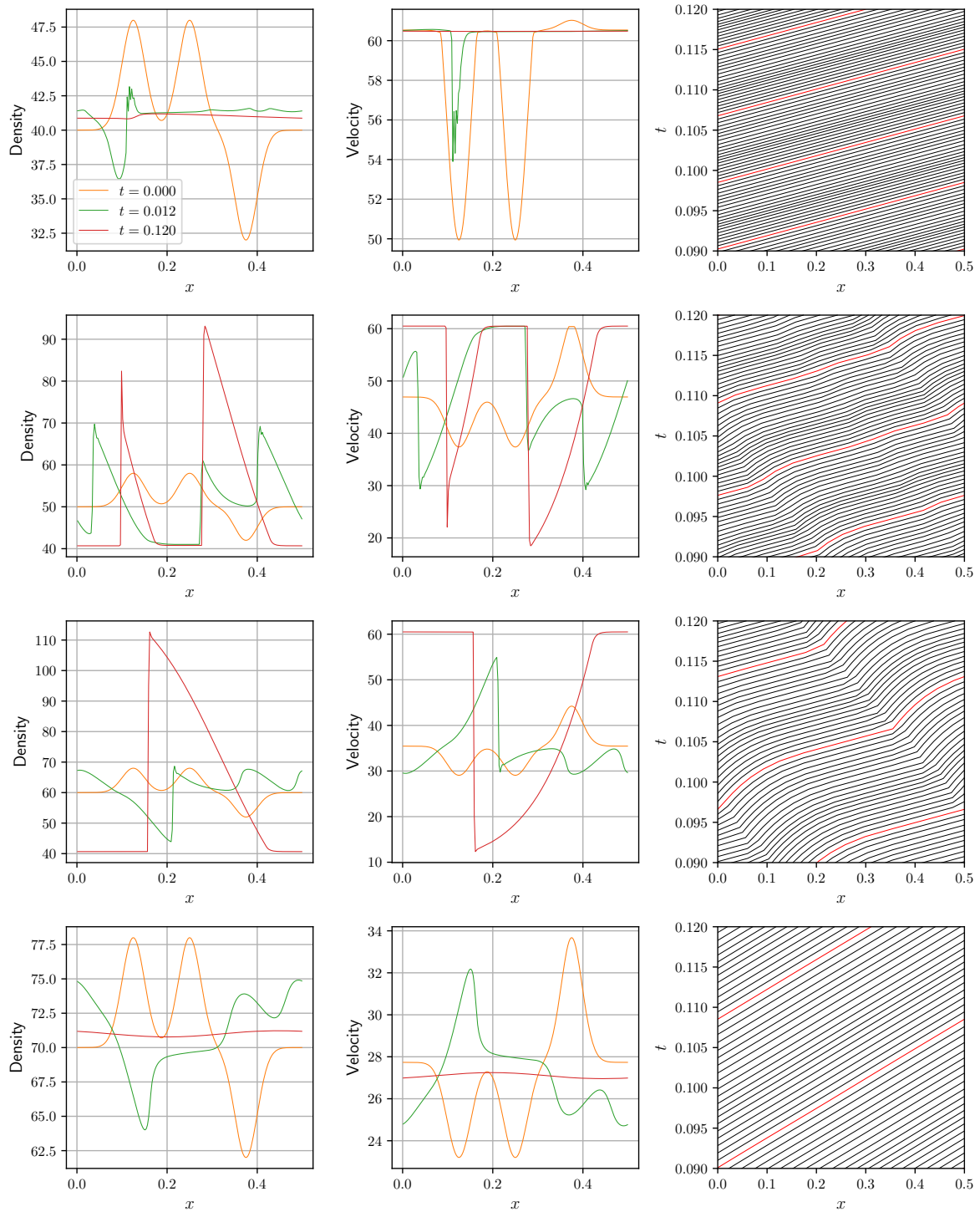


Figure 4.4: Numerical solutions to Equation 4.37 using the linearized fundamental diagram (Equation 1.21), parameters in Tables 4.2 and 1.2, and a small initial disturbance. The mean densities from top to bottom are $\rho_0 = 40.0$, $\rho_0 = 50.0$, $\rho_0 = 60.0$, $\rho_0 = 70.0$, $\rho_0 = 80.0$.

CHAPTER V

Stochastic Non-Equilibrium Traffic Models

We will consider two approaches to introducing stochasticity into non-equilibrium traffic models. The first is to couple an auxiliary equation describing dynamics of a behavior parameter z in a manner very similar to Chapter III. This method is far simpler for the non-equilibrium models we will consider, as the fundamental diagram only appears as a source term. The second system that will be considered is a result of perturbing the acceleration directly. In Chapter III we required an auxiliary equation to ensure conservation of mass. Because no momentum-like quantity is truly conserved, perturbing velocity directly is considered. The difference between these approaches is subtle, but important. In the first case we assume drivers have behavior that can be modeled as a stochastic process, and this behavior influences the equilibrium behavior (i.e. the fundamental diagram) for that driver. In the second case, we assume that acceleration is *directly* subject to white-noise perturbations.

Other authors have introduced a stochastic white noise to non-equilibrium traffic models. Khoshyaran et al [33] introduced a perturbation directly to acceleration in the Lagrangian frame. Because there is no viscous regularization it is unclear if the discretization of this method maintains consistent statistics under mesh refinement, but because it is discretized in the Lagrangian frame the method of lines discretization could be viewed as a car-following model of the form discussed in Appendix A. Gerster et al [19] considered (stochastic) param-

eter variation in ARZ. This work characterizes the distribution of solutions across possible parameter configurations and yields a method for quantifying parameter sensitivity, but not variation of parameters across a single realization. The goal of this chapter is to propose a set of models that provide consistent statistics under mesh refinement and demonstrate richer phenomena than their deterministic counterparts. To this end we will first introduce an auxiliary equation to the model proposed by Song and Karni [59] mirroring Section 3.2 and Section 3.3. A direct perturbation to velocity will be considered in Section 5.2.

5.1 Stochastic Second-Order Models with an Auxiliary z Equation

Consider the model

$$\rho_t + (\rho v)_x = 0 \quad (5.1a)$$

$$v_t + (v - g(\rho))v_x = \frac{V(\rho, \omega z) - v}{\tau^v} \quad (5.1b)$$

$$z_t + vz_x = \kappa z_{xx} - \frac{z}{\tau^z} + \eta \xi \quad (5.1c)$$

This equation mirrors Equation 4.9. A parameter $\omega \approx 1$ is again included so that the influence of the magnitude of response of the equilibrium velocity to changes in the parameter z can be observed. Unless otherwise stated, $\omega = 1$. We will discuss results for κ , τ^z , and η constant and for coefficients varied as a function of density in a manner analogous to Section 3.3.

The system (Equation 5.1) takes the form

$$\begin{bmatrix} \rho_t \\ v_t \\ z_t \end{bmatrix} + \underbrace{\begin{bmatrix} v & \rho & 0 \\ 0 & v - g(\rho) & 0 \\ 0 & 0 & v \end{bmatrix}}_A \begin{bmatrix} \rho_x \\ v_x \\ z_x \end{bmatrix} = \begin{bmatrix} 0 \\ \frac{V(\rho, \omega z) - v}{\tau^v} \\ \kappa z_{xx} - \frac{z}{\tau^z} + \eta \xi \end{bmatrix}. \quad (5.2)$$

The matrix A has eigenvalues $\lambda_1 = v - g(\rho) < \lambda_2 = \lambda_3 = v$, satisfying the anisotropy condition, and eigenvectors

$$R = [\mathbf{r}_1, \mathbf{r}_2, \mathbf{r}_3] = \begin{bmatrix} \rho & \rho & 0 \\ -g(\rho) & 0 & 0 \\ 0 & 0 & 1 \end{bmatrix}. \quad (5.3)$$

This system has one genuinely nonlinear wave (corresponding to $\lambda_1 = v - g(\rho)$) and two linearly degenerate waves (corresponding to $\lambda_2 = \lambda_3 = v$). The third equation (governing the dynamics of the driver variation parameter z) is coupled to the deterministic model only through the relaxation to the fundamental diagram and the advection of z . For the work in this chapter we will only consider $g(\rho)$ as given by Equation 4.39. To preserve hyperbolicity R (Equation 5.3) must be full rank; this requires $g(\rho) \neq 0$. We will impose this condition upon $g(\rho)$ in general. The ‘traffic principles’ satisfied by this non-equilibrium model, like acceleration and deceleration causing rarefaction waves and shock waves respectively, the anisotropy condition, and behavior at very high densities follow from the deterministic version (Equation 4.37).

Unlike the equilibrium models discussed in Chapter III, emergence of large congestion patterns like stop-and-go traffic does occur in deterministic non-equilibrium models without additional ‘driver variation’ variable z . In Chapter III the possibility of large structures spontaneously appearing was of interest. Here, large structures are expected for small perturbations of the underlying deterministic model; the question of interest is how these structures are different from the deterministic case. Following Section 3.10, we introduce density dependent coefficients $\kappa = \kappa(\rho)$ and $\eta = \eta(\rho)$ in the right hand side of Equation 5.1c. In general, the effects also mirror that of Section 3.3; the stop-and-go structures that develop are more pronounced.

5.1.1 Numerical Approximation

The numerical handling of Equation 5.1 is a combination of the handling of the deterministic equation (Section 4.5) and the handling of the source terms in the equilibrium models (Section 3.2.3). A first order operator splitting is used to split Equation 5.1 into

$$u_t + Au_x = \begin{bmatrix} 0 \\ \frac{V(\rho, \omega z) - v}{\tau^v} \\ 0 \end{bmatrix} \quad (5.4a)$$

$$u_t = \kappa z_{xx} - \frac{z}{\tau^z} + \eta \xi \quad (5.4b)$$

The first half step is discretized using a Roe-type scheme (see e.g. [41]) with a flux limiter. The second half step uses backward Euler for relaxation terms, forward Euler for the integral of noise, and an explicit forward time central space step for diffusive terms.

In the first half step, we project state differences and the relaxation to the velocity specified by the fundamental diagram onto eigenvectors:

$$\alpha_{j+\frac{1}{2}} = R_{j+\frac{1}{2}}^{-1} \begin{bmatrix} \Delta \rho \\ \Delta v \\ \Delta z \end{bmatrix} = \begin{bmatrix} -\frac{\Delta v}{g(\rho_{j+\frac{1}{2}})} \\ \frac{\Delta \rho}{\rho_{j+\frac{1}{2}}} + \frac{\Delta v}{g(\rho_{j+\frac{1}{2}})} \\ \Delta z \end{bmatrix} \quad (5.5)$$

$$\beta_{j+\frac{1}{2}} = R_{j+\frac{1}{2}}^{-1} \begin{bmatrix} 0 \\ \frac{1}{2} \left(\frac{V(\rho_j, \omega z_j) - v_j}{\tau^v} + \frac{V(\rho_{j+1}, \omega z_{j+1}) - v_{j+1}}{\tau^v} \right) \\ 0 \end{bmatrix} \quad (5.6)$$

Letting Λ , Λ^+ , and Λ^- be as they were in Section 3.2.3 and Section 4.5 and $|\Lambda| = \Lambda^+ - \Lambda^-$,

the first half step is given by

$$\begin{aligned}
U_j^* = U_j^n &- \frac{k}{h} \left(R_{j-\frac{1}{2}} \Lambda_{j-\frac{1}{2}}^+ \left(\boldsymbol{\alpha}_{j-\frac{1}{2}} - h\boldsymbol{\beta}_{j-\frac{1}{2}} \right) + R_{j+\frac{1}{2}} \Lambda_{j+\frac{1}{2}}^- \left(\boldsymbol{\alpha}_{j+\frac{1}{2}} - h\boldsymbol{\beta}_{j+\frac{1}{2}} \right) \right) \\
&- \frac{k}{2h} \left(R_{j+\frac{1}{2}} |\Lambda_{j+\frac{1}{2}}| \left(1 - \frac{k}{h} |\Lambda_{j+\frac{1}{2}}| \right) \Phi_{j+\frac{1}{2}} \boldsymbol{\alpha}_{j+\frac{1}{2}} \right. \\
&\quad \left. - R_{j-\frac{1}{2}} |\Lambda_{j-\frac{1}{2}}| \left(1 - \frac{k}{h} |\Lambda_{j-\frac{1}{2}}| \right) \Phi_{j-\frac{1}{2}} \boldsymbol{\alpha}_{j-\frac{1}{2}} \right)
\end{aligned} \tag{5.7}$$

where $\Phi_{j+\frac{1}{2}}$ and its constituent parts are as they were in the deterministic case (Equation 4.47, Equation 4.48, and Equation 4.50).

The right hand side of the z equation is advanced per Section 3.2.3, again using the standard forward time central space scheme for diffusion and backward Euler for relaxation. The latter part of a timestep is then given by

$$\rho_j^{n+1} = \rho_j^* \tag{5.8a}$$

$$z_j^{n+1} = z_j^* - \frac{kz_j^*}{\tau z + k} + \kappa \frac{k}{h^2} (z_{j-1}^* - 2z_j^* + z_{j+1}^*) + \sqrt{\frac{k}{h}} \eta \xi_j^n \tag{5.8b}$$

where ξ_j^n are i.i.d. standard normal variables.

5.1.2 Ringroad

Throughout the present work an effort is made to use a consistent set of parameters, thus arguing that the results demonstrate the range of differences between models rather than the effects of different parameters. Accordingly, Figure 5.1 and Figure 5.2 show sample realizations of Equation 5.1 with constant values of κ and η with the same fundamental diagram (Equation 1.21) and parameters (Table 3.1, Table 4.1, and Table 1.2) used in previous chapters. Figures 5.1 and 5.2 have mean densities $\rho_0 = 50.0$ and $\rho_0 = 60.0$ respectively. In both of these cases the linear stability analysis predicts instability (see Figure 4.1). The qualitative behavior shown in Figure 5.1 and Figure 5.2 is nearly identical to the deterministic

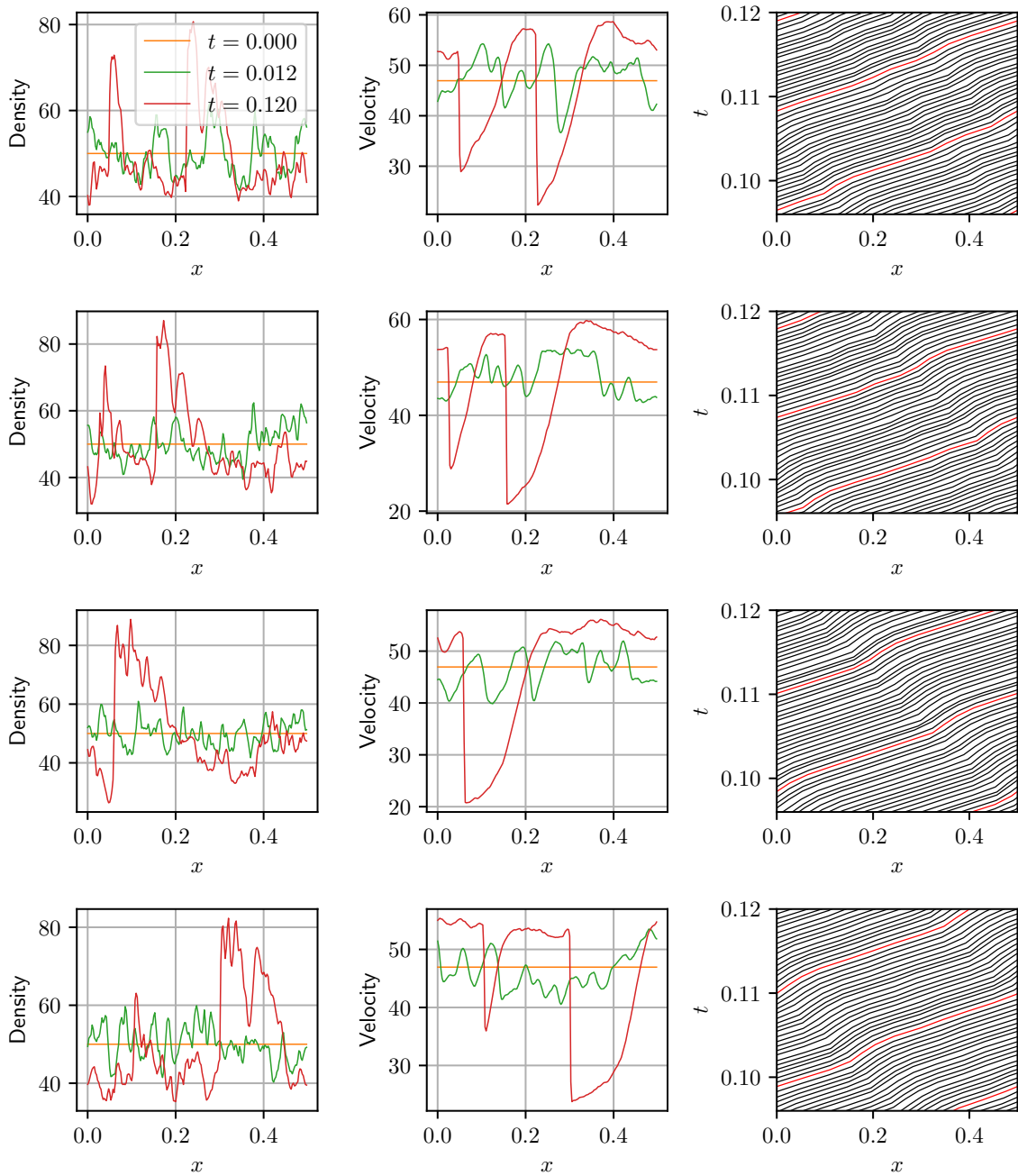


Figure 5.1: Example realizations of the ringroad experiment using Equation 5.1 with constant coefficients η and κ with an initial uniform density of 50.0.

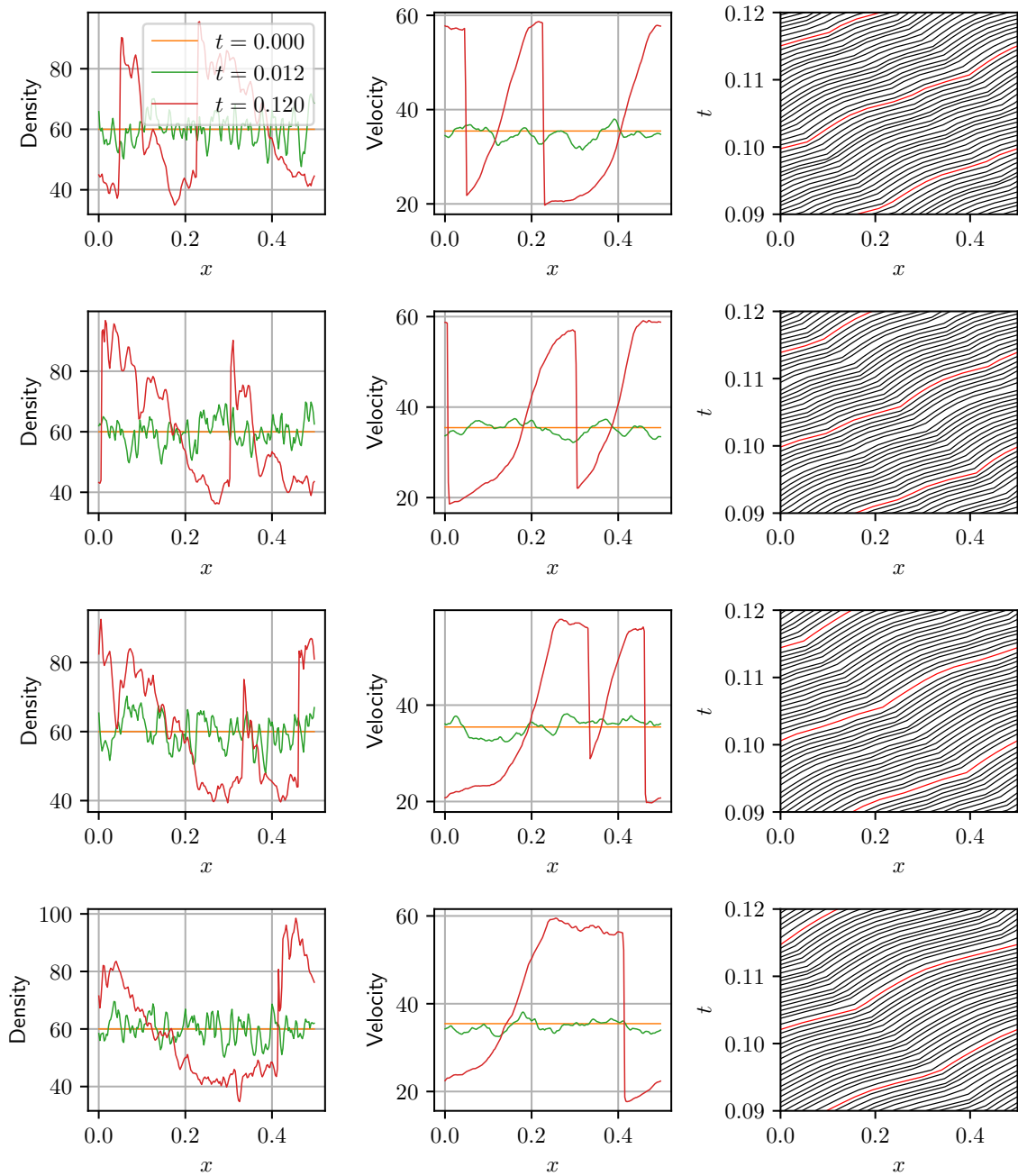


Figure 5.2: Example realizations of the ringroad experiment using Equation 5.1 with constant coefficients η and κ with an initial uniform density of 60.0.

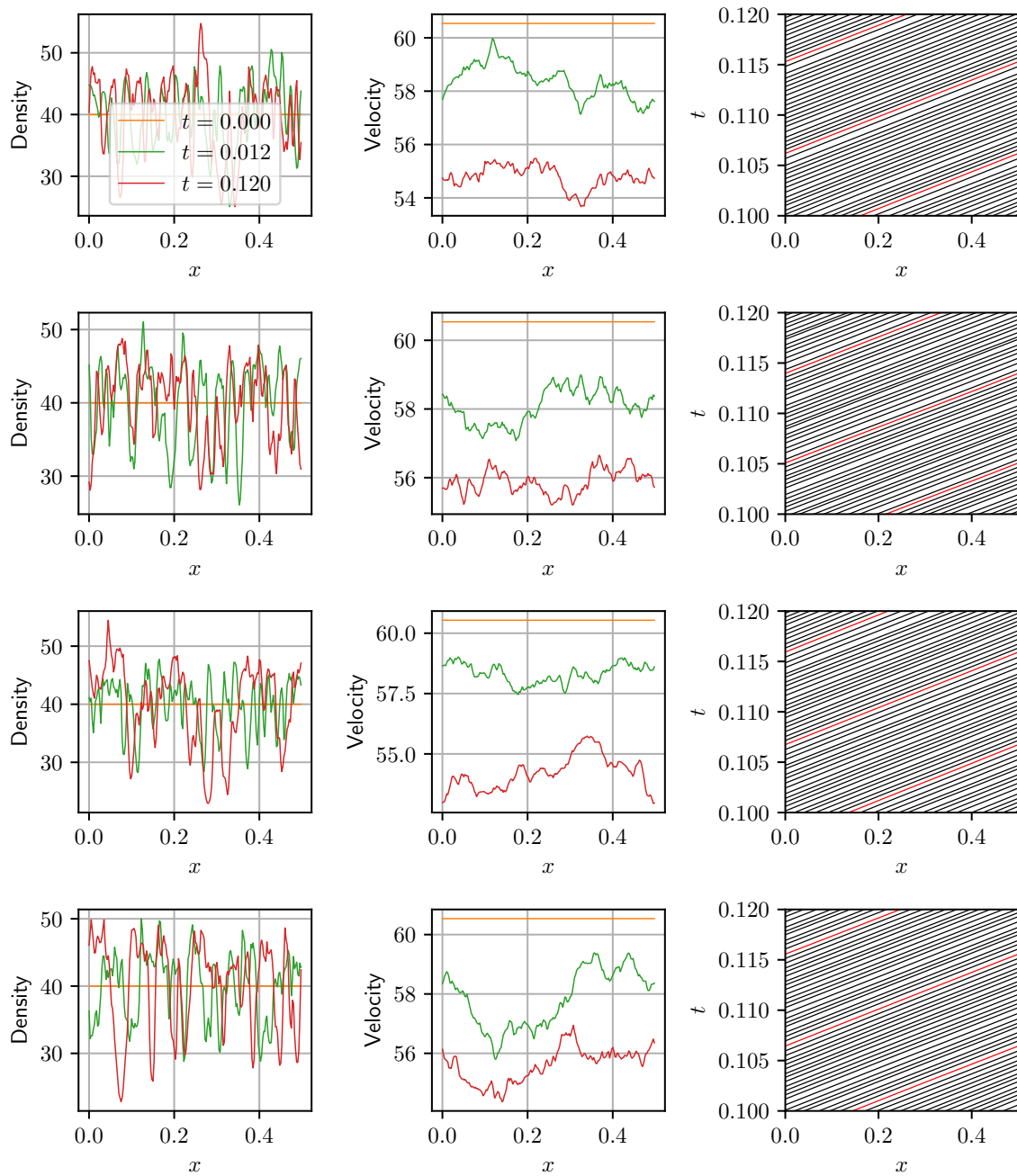


Figure 5.3: Example realizations of the ringroad experiment using Equation 5.1 with variable coefficients (Equation 3.25) with an initial uniform density of 40.0.

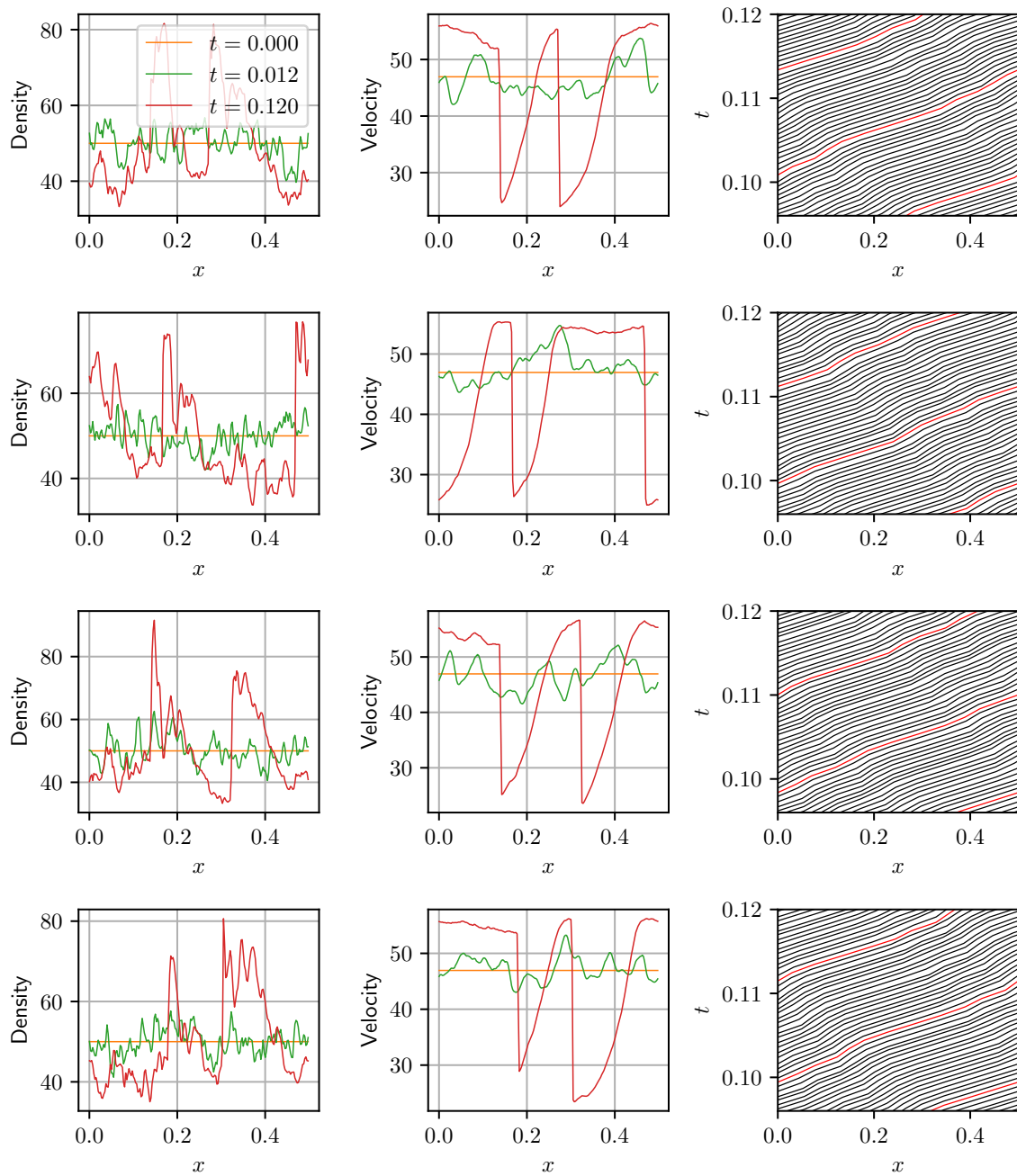


Figure 5.4: Example realizations of the ringroad experiment using Equation 5.1 with variable coefficients (Equation 3.25) with an initial uniform density of 50.0.

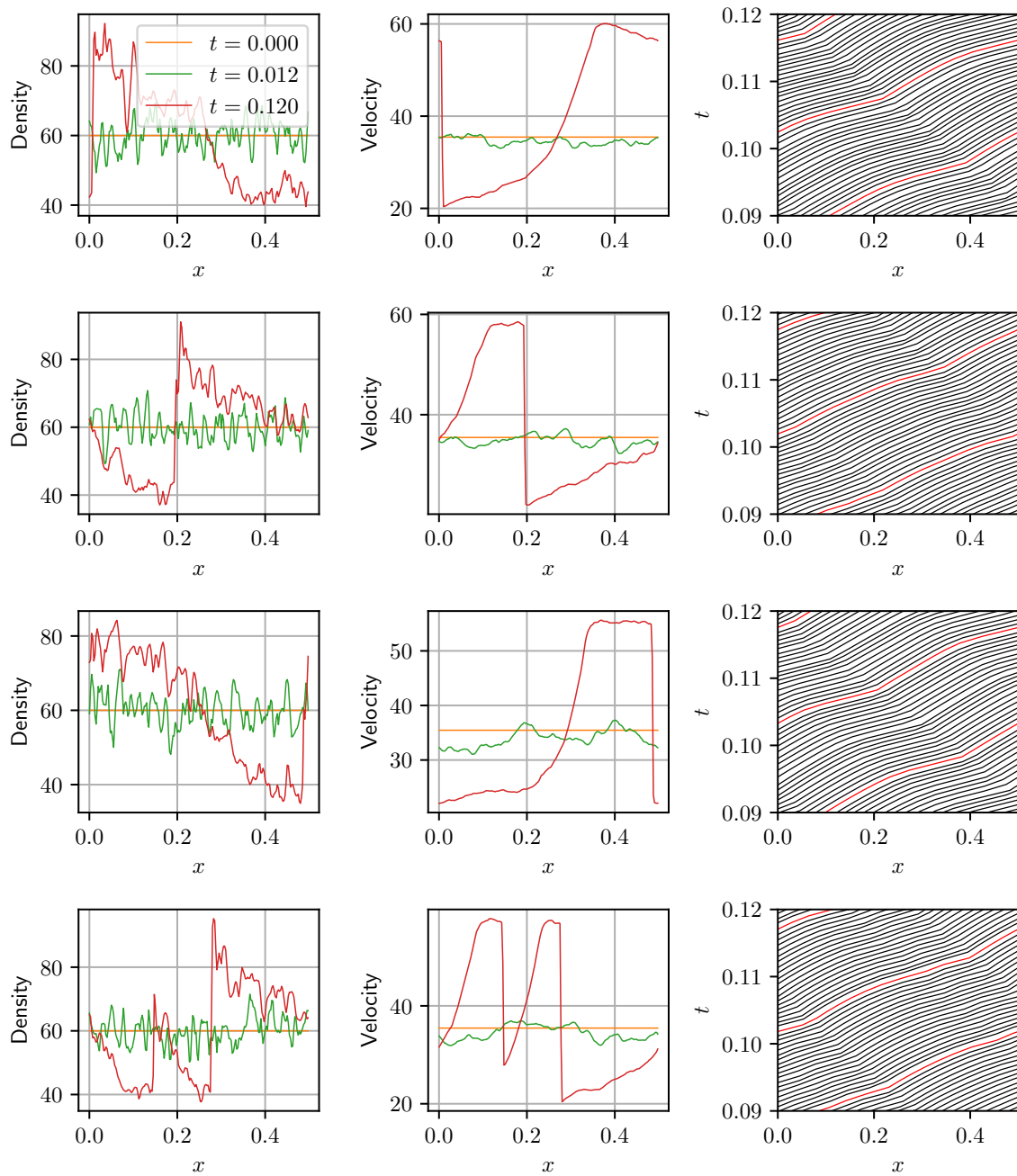


Figure 5.5: Example realizations of the ringroad experiment using Equation 5.1 with variable coefficients (Equation 3.25a) with an initial uniform density of 60.0.

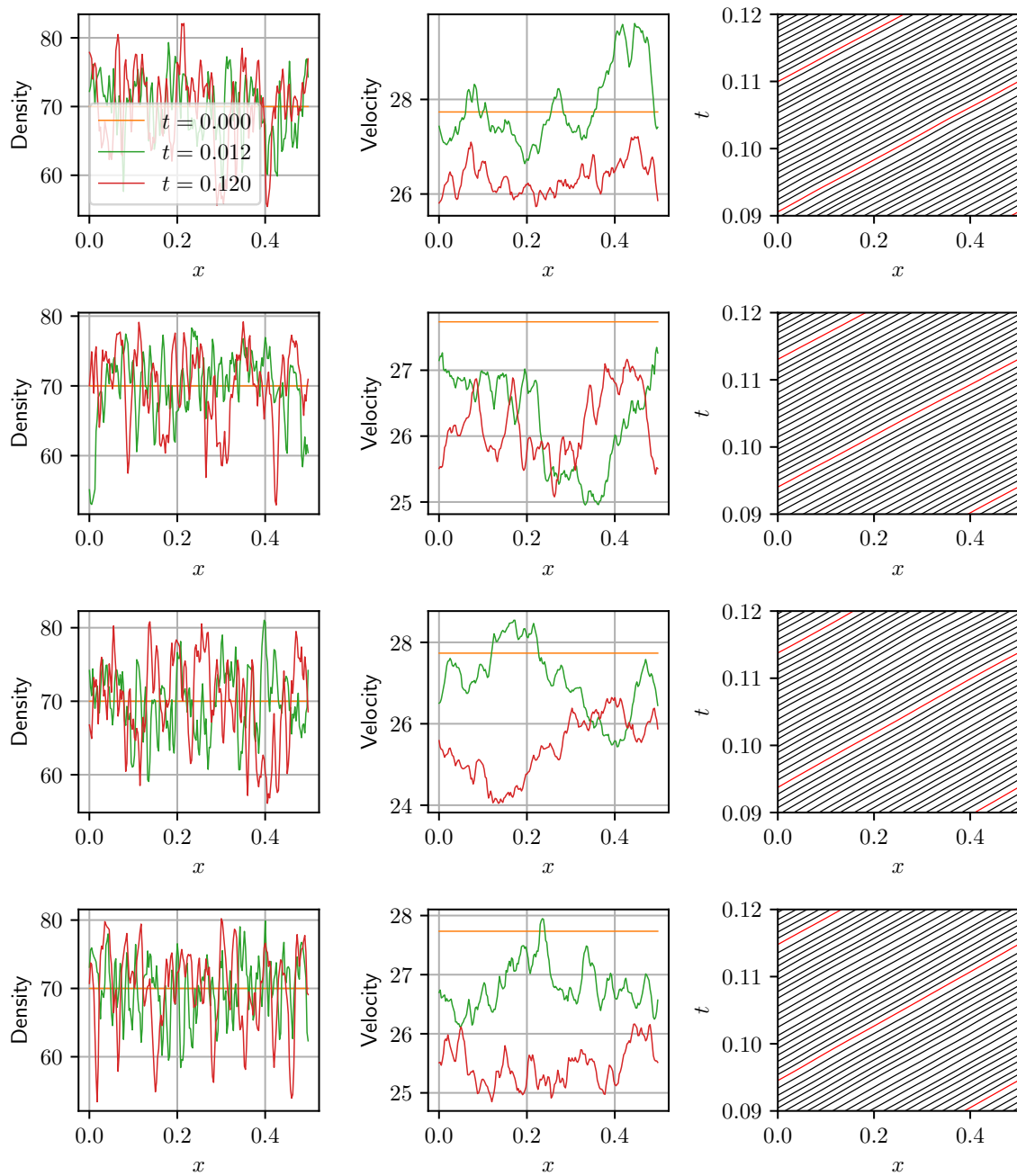


Figure 5.6: Example realizations of the ringroad experiment using Equation 5.1 with variable coefficients (Equation 3.25a) with an initial uniform density of 70.0.

case with an initial perturbation (Figure 4.4). As was the case in previous chapters, multiple realizations in each case have been shown to give some demonstration of how self consistent (or inconsistent) the results obtained are. Like the models considered in Chapter III, realizations are surprisingly consistent.

As was the case throughout Chapter III, the introduction of density dependent viscosity coefficients results in qualitatively similar results that are slightly more pronounced; example realizations at each of the densities shown in Figures 4.1 and 4.4 are shown in Figures 5.3 through 5.6. Outside of the unstable region (Figure 5.3 and Figure 5.6) behavior largely mirrors what was seen in Chapter III for densities that did not yield instability; the overall velocity decreases due to the limiting effects of the slowest driver and small variations in density occur. A surprising result at a high density (outside the range in which instability is expected) can be found in Figure 5.6; here an unstable stop and go pattern evolves in one case but not others. It was observed in Chapter III that the introduction of noisy source terms may lead to persistent phenomena not present otherwise, and it is observed here, if rarely.

One means of measuring the frequency of this type of phenomena is through a Monte-Carlo method (again following Chapter III). In Figure 5.7 the range of velocities across the domain after some evolution from an unperturbed initial condition is presented. In addition, the velocity range computed from the deterministic case with a perturbed initial condition (Figure 4.4) is represented (vertical red lines). Though the transition between stability and instability roughly matches what is predicted by the linearized analysis, it is of note that the distribution of solutions in the noisy case is not, in general, centered around the nominal (noise free) case. Here we demonstrate that the range of velocities present is less sensitive to density than the deterministic equation.

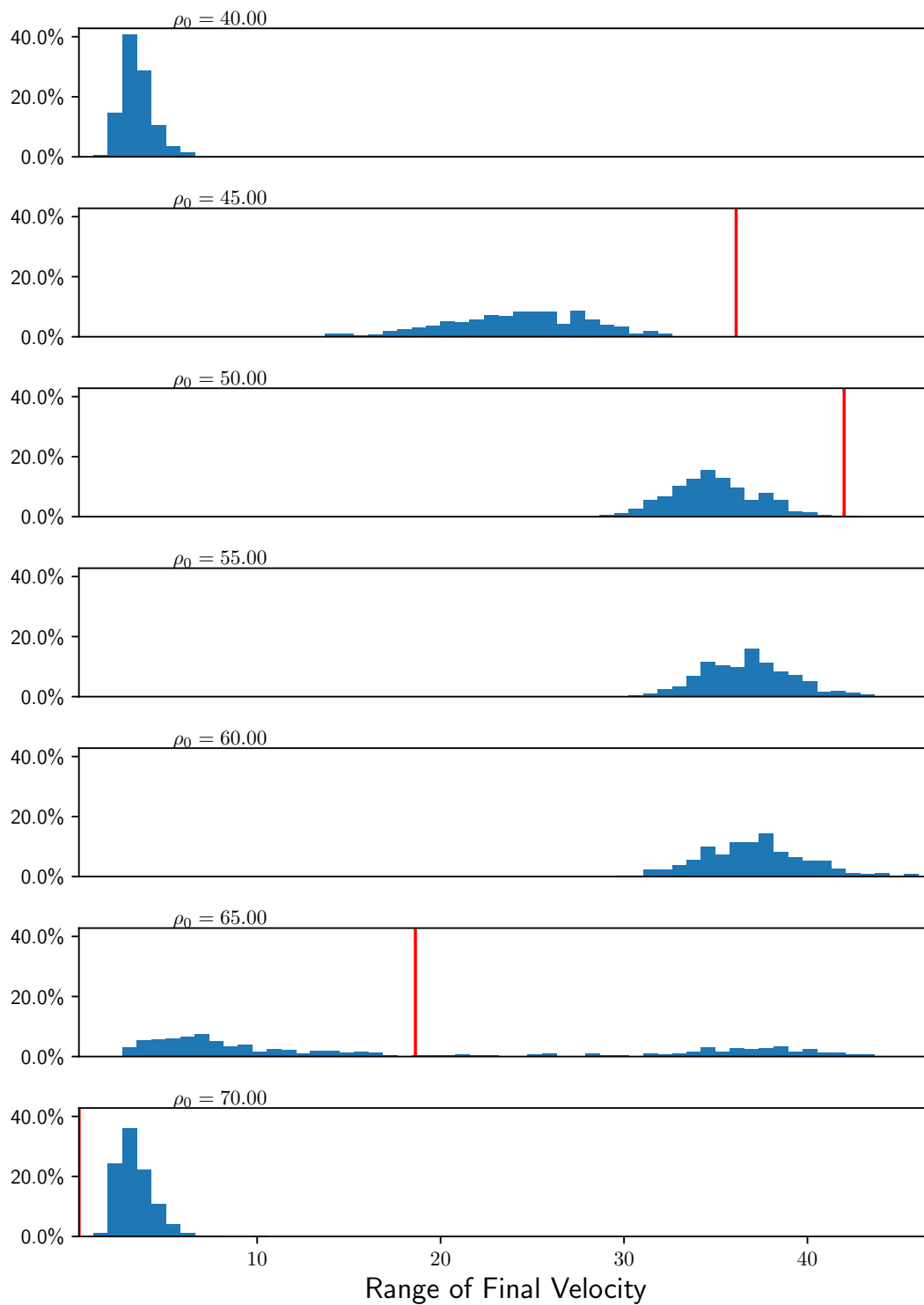


Figure 5.7: Distribution of velocity range at $t = 0.12$ for the ringroad experiment under Equation 5.1 with variable coefficients. Red vertical lines represent the velocity at this time under the deterministic equations with an initial density perturbation per Figure 4.4.

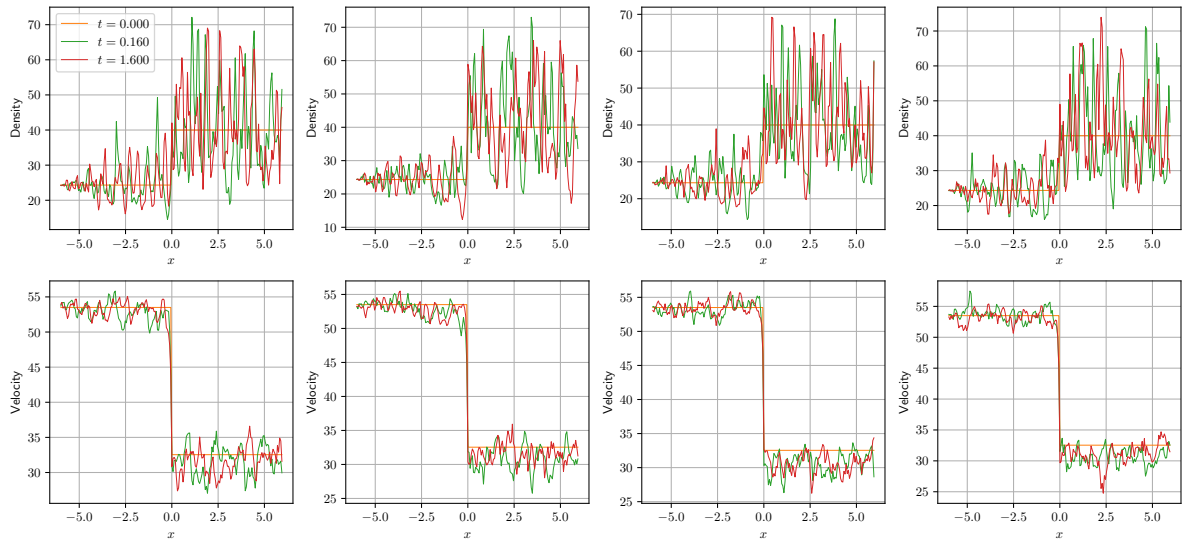


Figure 5.8: For example realizations of the ‘speed drop’ experiment under Equation 5.1 and $\omega = 1.0$.

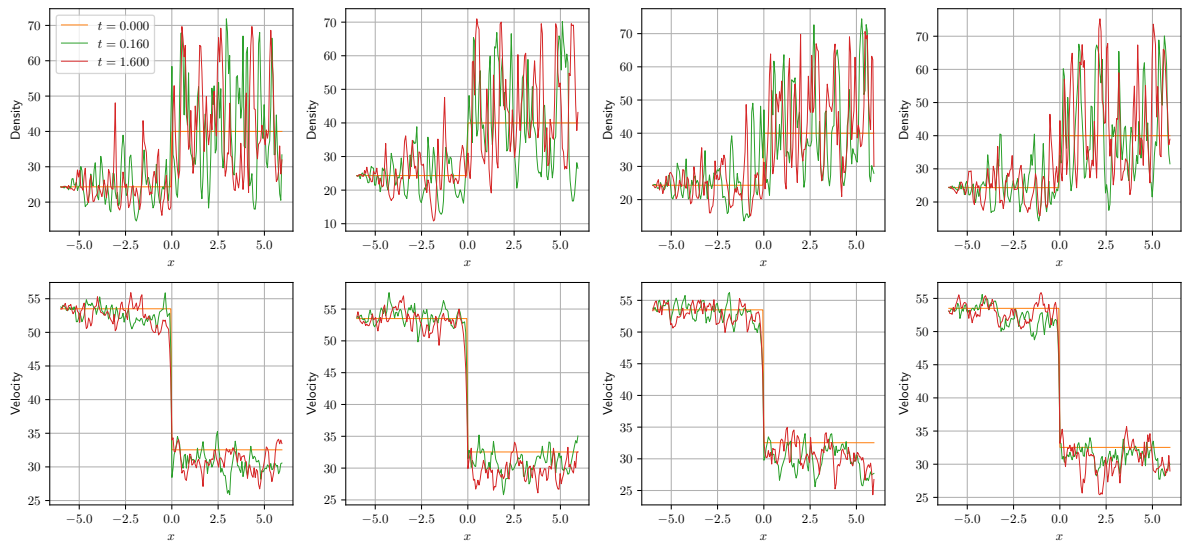


Figure 5.9: Speed drop experiment under Equation 5.1 and $\omega = 1.2$.

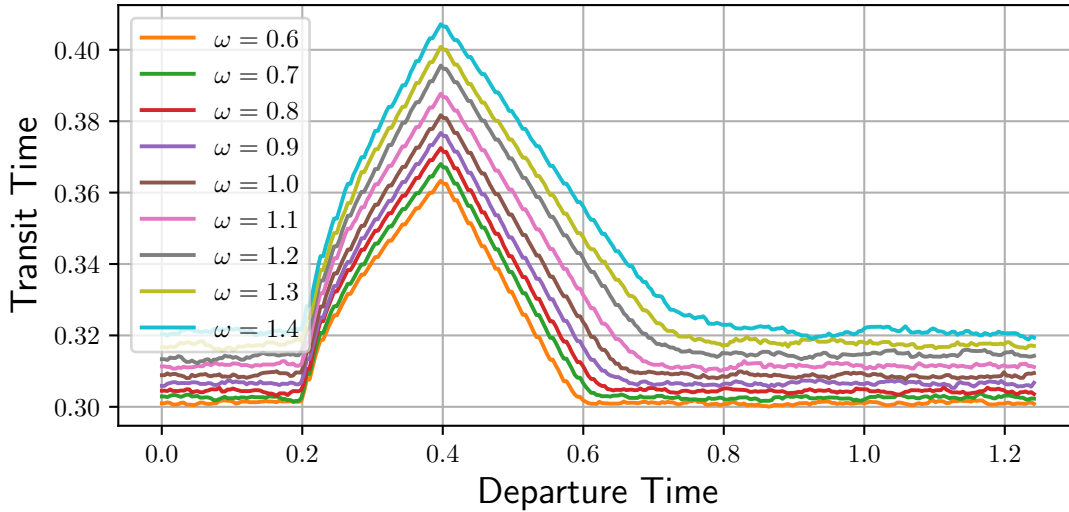


Figure 5.10: Travel times in the speed drop experiment as a function of start time for selected values of ω , averaged over several realizations.

5.1.3 Speed drop

In the interest of space we will discuss the speed drop experiment only in the case of variable coefficients (i.e. Equation 5.1 with Equations 3.25a, 3.25b, and 3.25c). We present example realizations (Figure 5.8) with parameters used previously (Tables 3.1, 1.2, and 4.2) and examples with the effect of the noise on the fundamental diagram amplified by 20% (Figure 5.9). Note Figures 5.8 and 5.9 show variation in space at the same scale as other figures throughout this thesis; the length scale of the speed drop case is far longer than that of the cases with periodic boundary conditions. As was the case in Chapter III, little can be qualitatively concluded from individual realizations in this case. However, as shown in Figure 5.10, the time taken to traverse the domain increases dramatically as ω is increased.

5.2 Stochastic Second-Order Models with Direct Noise

We have introduced noise to both equilibrium and non-equilibrium models through an auxiliary advection diffusion equation with forcing. This auxiliary equation was used because doing so allowed for coefficients in the z equation to be controlled (before coupling to velocity)

through known relations and because doing so provided a model that largely inherited the desirable properties for traffic models from existing deterministic equations. In this section we explore an alternative approach in which source terms are introduced directly to the velocity equation. Throughout we will utilize insights gathered from the auxiliary equation approach. For one, we have argued a viscous term is necessary. We further argued that to vary on the length scale equal to driver spacing the viscous term should behave like ρ^{-2} . Finally, by neglecting the coupling to velocity we have obtained proposed formulae for the coefficients in the auxiliary noise equation. All of these observations would be far less clear without the auxiliary equation approach and are used in this section.

First, let us begin with the model proposed by Song and Karni [59] (Equation 4.37) with a viscous term and white noise added to the velocity equation:

$$\begin{aligned} \rho_t + (\rho v)_x &= 0 \\ v_t + (v - g(\rho))v_x &= \frac{V(\rho) - v}{\tau v} + \kappa(\rho) v_{xx} + \eta(\rho)\xi \end{aligned} \tag{5.9}$$

where $g(\rho)$ is given by Equation 4.39. The components of the stochastic heat equation (Equation 2.4) that we based the preceding work on has three terms: a relaxation to equilibrium, a viscous regularization, and a white noise. Equation 4.37 was introduced by Song [59] with a viscous term (though it was ultimately discarded) and that term grew like ρ^{-2} for large densities. The viscosity present here does not serve the purpose the original viscosity served however, and we will choose a new viscous coefficient. Further, the coefficients κ and η will need to not only depend on ρ to reflect the proper length scales but also need to be chosen in a manner such that negative velocities are avoided.

Regardless of the choices made to specify coefficients in Equation 5.9, direct introduction of noise is expected to produce density and velocity fields somewhat less smooth than the model with an auxiliary equation (Equation 5.1) as density and velocity are computed from one fewer integrals of white noise. Further, this approach requires the inclusion of viscosity in the velocity equation, whereas it is typically desired for PDE traffic models to be hyper-

bolic (e.g. [2, 18]). On the other hand, this formulation does not require a parameterized family of fundamental diagrams $V(\rho, z)$. Regardless of any other parameter related concerns, trading a function $V : \mathbb{R}^2 \rightarrow \mathbb{R}$ in which the second input dimension is impossible to measure directly for a function $V : \mathbb{R} \rightarrow \mathbb{R}$ that is relatively straightforward to measure is an immense simplification.

For the results shown in this section we have chosen to use a viscosity coefficient of the form

$$\kappa(\rho) = \frac{\kappa_0}{\rho^2} \quad (5.10)$$

This form allows the viscosity coefficient as well as additional spatial statistics to be controlled, and provides the same density scaling argued for previously (Equation 3.25). We will, however, keep the same τ^v as the unperturbed case, simplifying the parameters in this case substantially. Because τ^v is obtained from another source, we only impose a pointwise scale and a length scale, and Equation 3.7 becomes

$$\sigma^2 = \frac{(\eta')^2}{4} \sqrt{\frac{\tau^v}{\kappa'}} \quad (5.11a)$$

$$\sigma_x^2 = \frac{(\eta')^2}{4} \sqrt{\frac{\tau^v}{\kappa'}} \exp\left(-(\tau^v \kappa' \rho_{\text{ref}}^2)^{-\frac{1}{2}}\right) \quad (5.11b)$$

where the η and κ are related to η' and κ' by

$$\eta = \eta' \sqrt{\frac{\rho_{\text{ref}}}{\rho}}, \quad (5.12a)$$

$$\kappa = \kappa' \left(\frac{\rho_{\text{ref}}}{\rho}\right)^2. \quad (5.12b)$$

(These are identical to Equations 3.26 and 3.27.) A physical length scale can then be

Table 5.1: Parameters used for demonstrations of Equation 5.9.

σ	2.0
σ_x	0.02
ρ_{ref}	105.6
ρ_{floor}	2.0

introduced resulting in coefficients

$$\kappa' = \frac{1}{\tau^v} \left(2\rho_{\text{ref}} \log \left(\frac{\sigma_x}{\sigma} \right) \right)^{-2} \quad (5.13a)$$

$$\eta' = 2\sigma \left(\frac{\kappa'}{\tau^v} \right)^{-\frac{1}{4}}. \quad (5.13b)$$

These values of κ and η produce the desired length scale of variation at (any) constant density, but behavior with coupling to a system of equations is uncertain. It is, however, assumed the coefficients arising from these relations result in the correct order of magnitude. As a final note, we have suggested that decreasing the coefficients from which σ^2 and σ_x^2 are computed when velocity is small to avoid negative velocities may be necessary. For the results that follow this was not done and does not appear to be required even for high densities.

5.2.1 Numerical Approach

Computations in this section follow a scheme almost identical to that of Section 5.1.1. The hyperbolic part is advanced by Equation 5.7 where $R_{j+\frac{1}{2}}$, $\Lambda_{j+\frac{1}{2}}$, $\alpha_{j+\frac{1}{2}}$, $\beta_{j+\frac{1}{2}}$, and $\Phi_{j+\frac{1}{2}}$ are as they were in Section 4.4. The latter half step is computed by Equation 5.8, but the source and viscosity terms are applied to velocity rather than the auxiliary z variable. κ_j and η_j are of course computed from Equations 3.26, 3.27, 5.13a, and 5.13b.

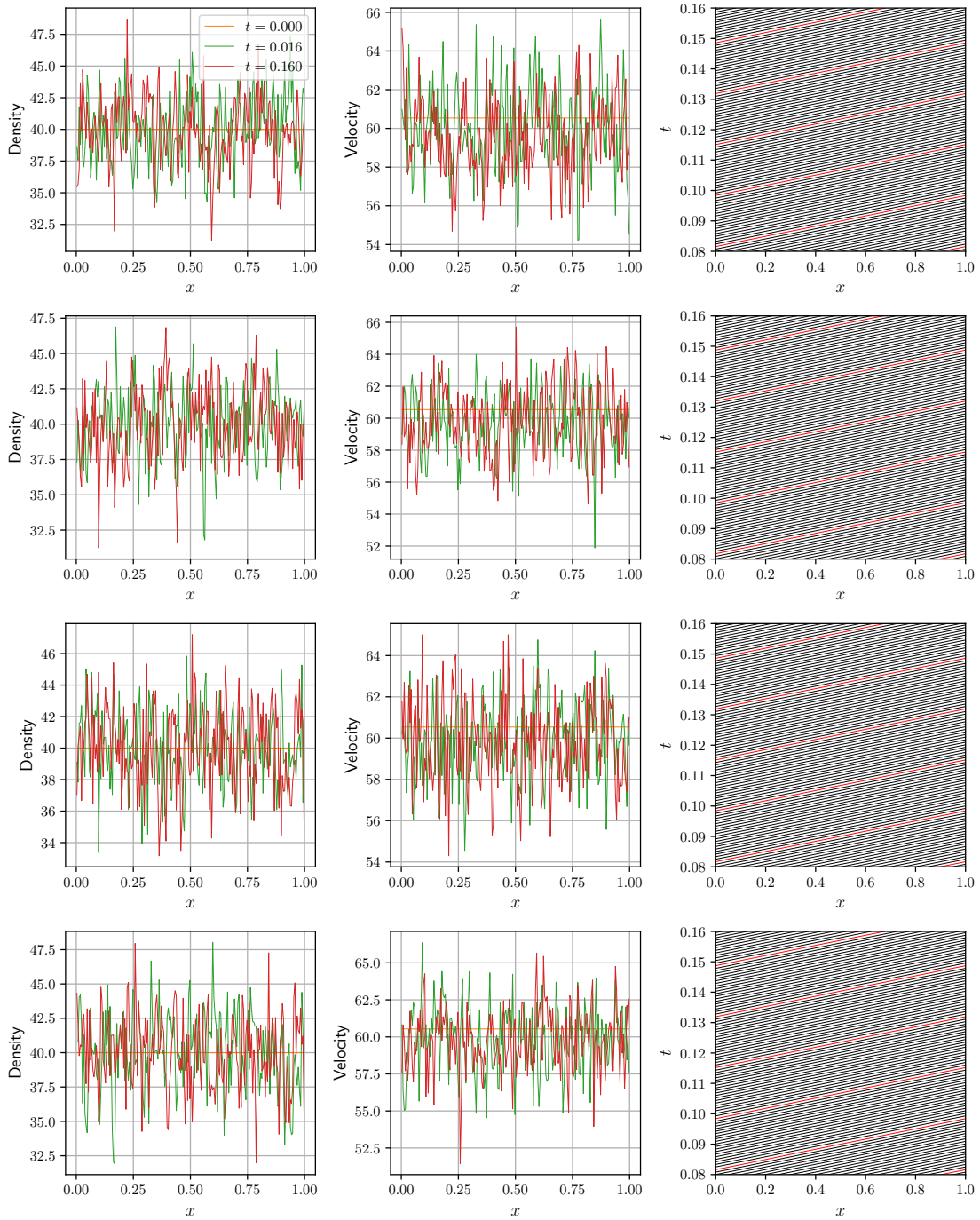


Figure 5.11: Example realizations of the ringroad experiment under Equation 5.9 with parameters in Table 4.2 and Table 5.1 and initial uniform density of $\rho_0 = 40.0$.

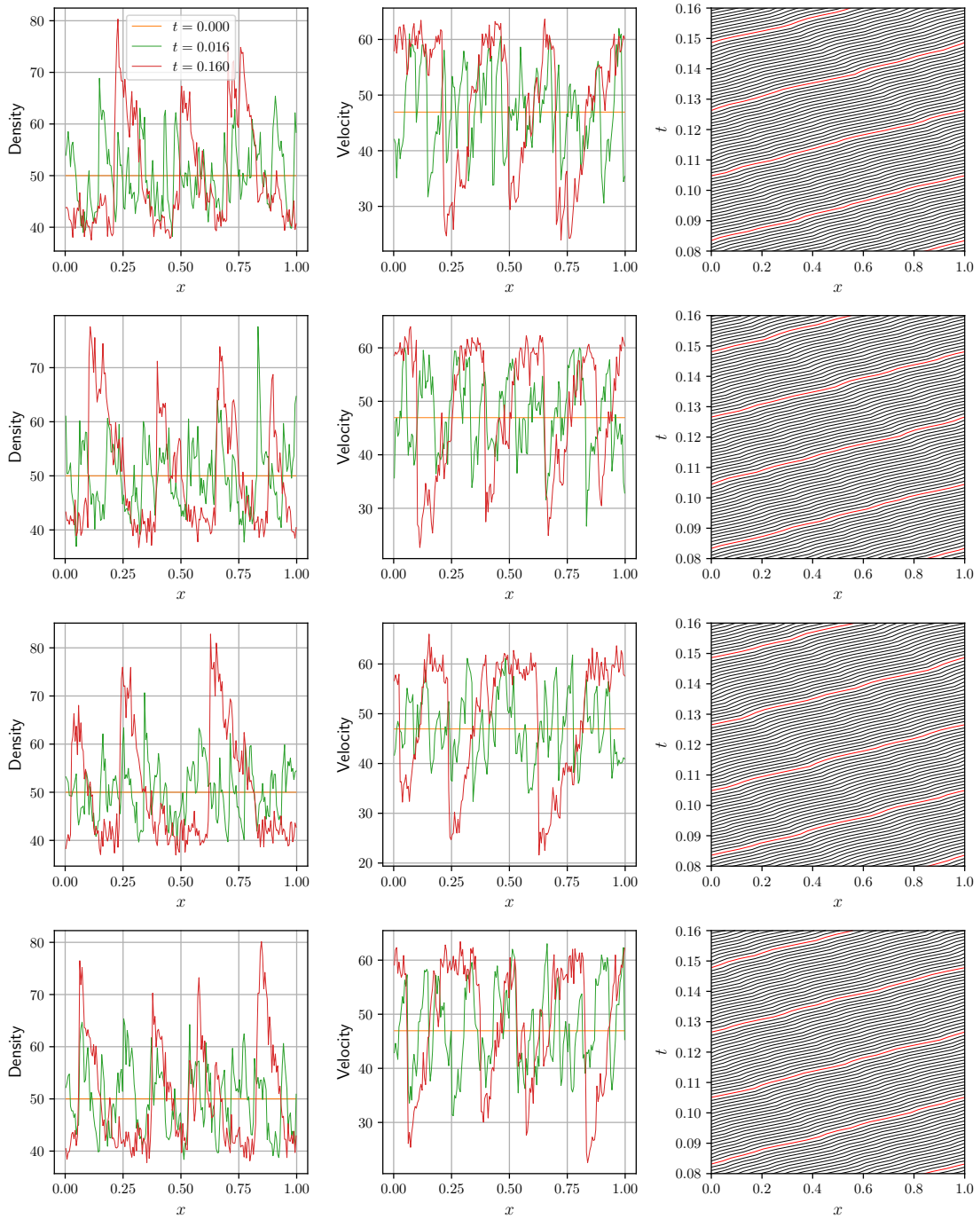


Figure 5.12: Example realizations of the ringroad experiment under Equation 5.9 with parameters in Table 4.2 and Table 5.1 and initial uniform density of $\rho_0 = 50.0$.

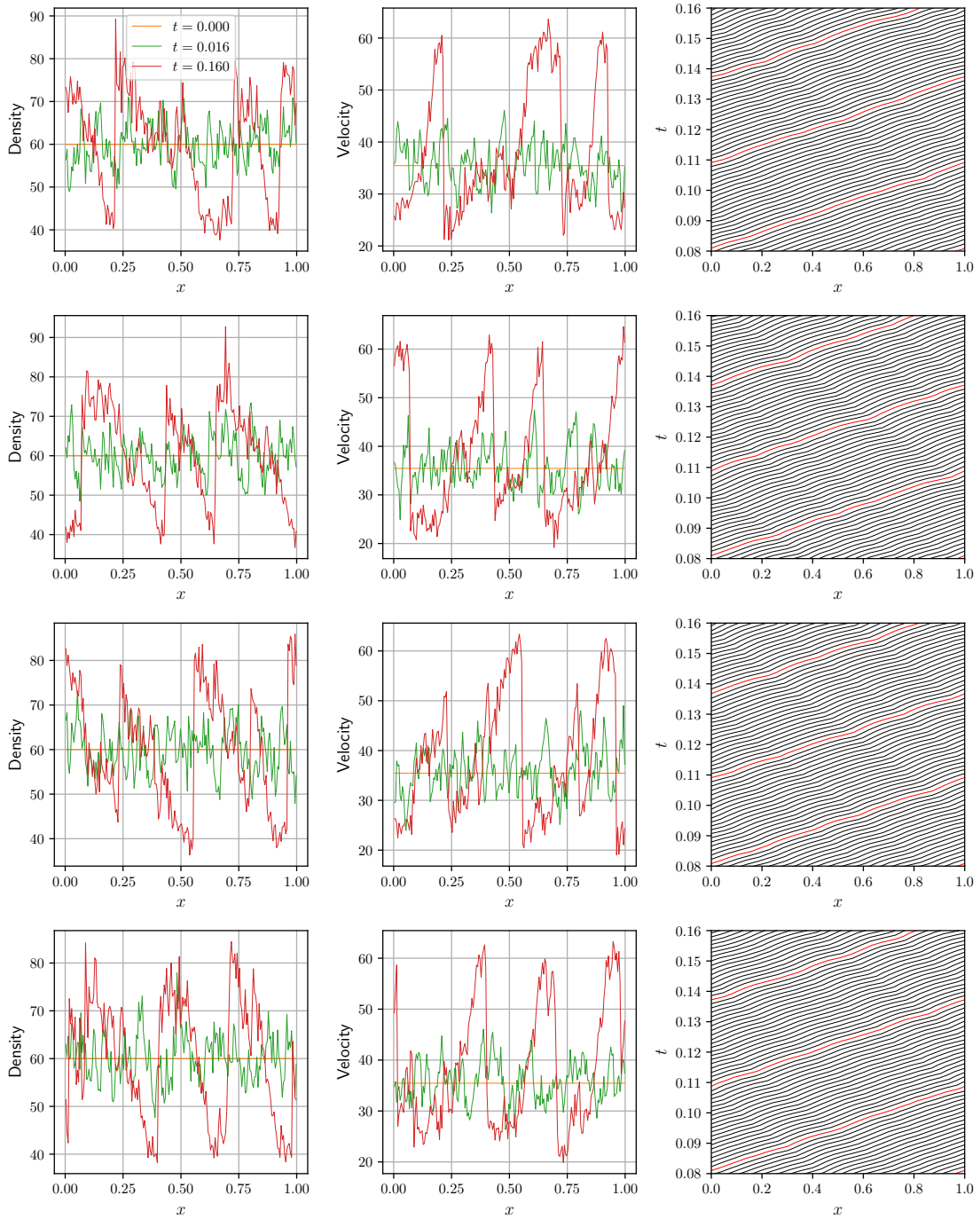


Figure 5.13: Example realizations of the ringroad experiment under Equation 5.9 with parameters in Table 4.2 and Table 5.1 and initial uniform density of $\rho_0 = 60.0$.

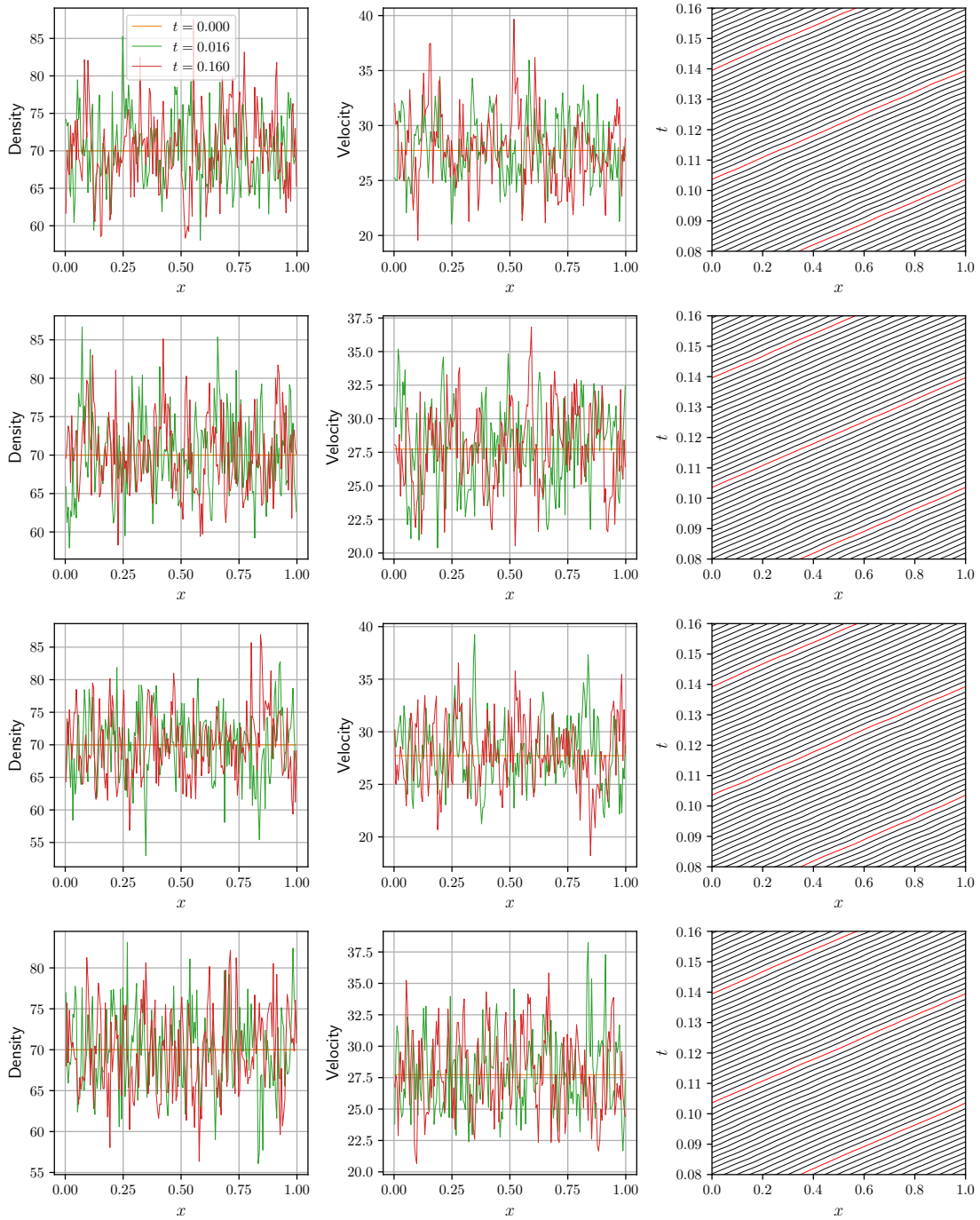


Figure 5.14: Example realizations of the ringroad experiment under Equation 5.9 with parameters in Table 4.2 and Table 5.1 and initial uniform density of $\rho_0 = 70.0$.

5.2.2 Ringroad

Direct addition of noise into the velocity equation, in the context of the ringroad experiment, resembles the addition of noise through an auxiliary equation (Section 5.1.2). Figures 5.11 through 5.14 show example realizations of the ringroad experiment at the four densities shown in Figure 4.1. Linearized analysis of the unperturbed equation predicts the four densities will result in stable, unstable, unstable, and stable behavior respectively. This prediction does hold true for the system with direct noise.

The same comparison of the deterministic case (Equation 4.37) to the case with noise at varied densities that was made previously (Figure 5.7) may be made here as well, and is shown in Figure 5.15. While every attempt has been made to utilize equivalent parameters throughout, there is not a clear method by which parameter sets may be made truly equivalent across the models in question. For example, comparing the width of the distributions in Figures 5.7 and 5.15 is not a meaningful exercise. None of the differences between the two formulations in this chapter effect the predicted stability range. It is interesting that the transition between stable and unstable patterns is different between the two models. It is not clear whether the transition between stability and instability both at the lower and higher end of the unstable interval is fundamentally different (see $\rho_0 = 45.0$ in Figure 5.7 and $\rho_0 = 65.0$ in Figure 5.15) between the two cases or if the density values at which data was gathered represent different parts of the transition region. In either case, at the transition region between the two densities at the higher end of the interval enables a wide range of possible amplitudes. While the evidence gathered here is not sufficient to assert the transition at the two ends of the unstable interval demonstrate different behavior, the nature of the fundamental diagram in question (Figure 4.1) certainly poses that question. In either case the distribution of the range of velocities in the unstable region is very similar throughout the middle of the unstable region, and in neither case do the centers of those distributions match the unperturbed case.

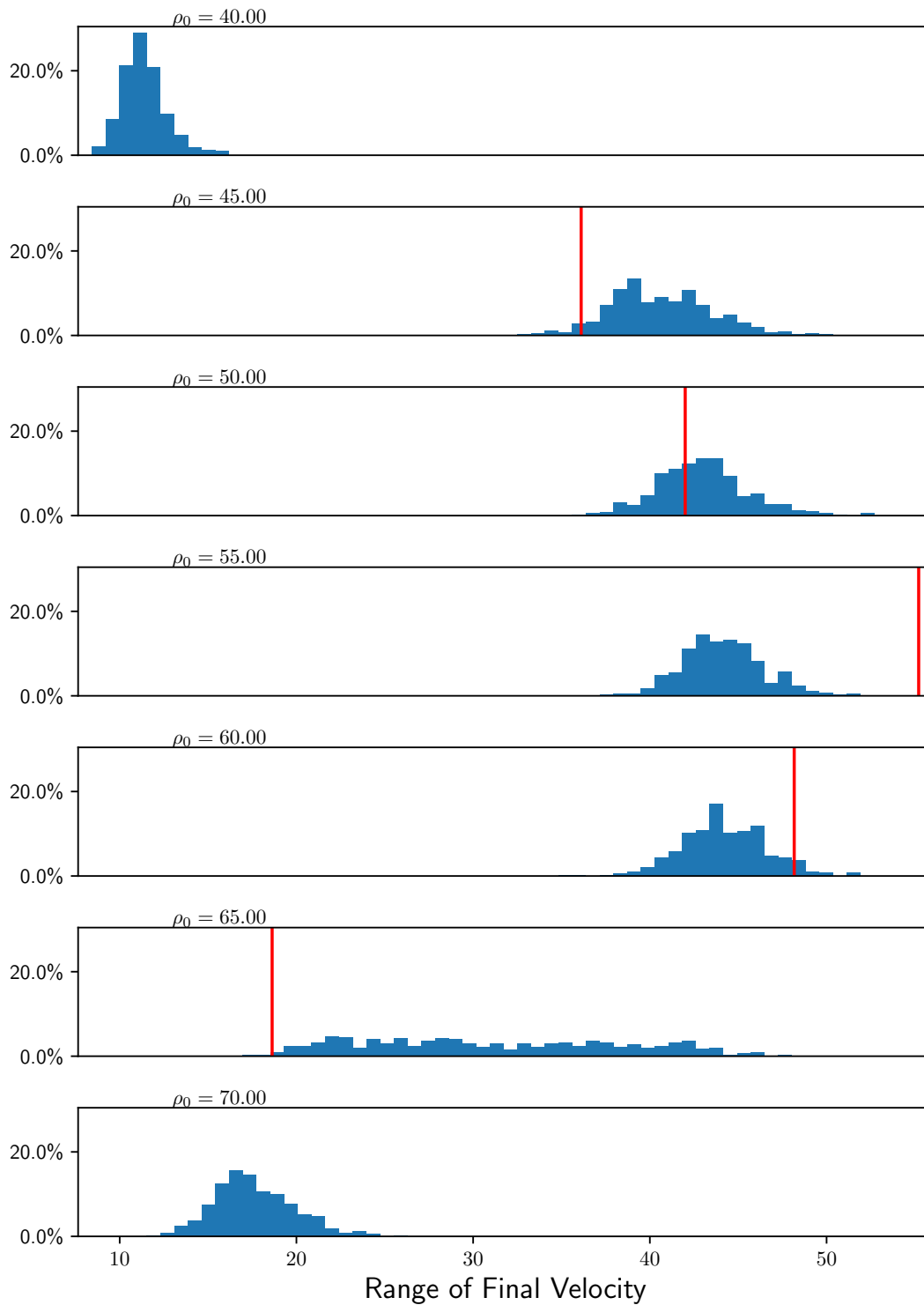


Figure 5.15: Distribution of velocity range at $t = 0.16$ for the ringroad experiment under Equation 5.9 with variable coefficients. Red vertical lines represent the velocity at this time under the deterministic equations with an initial density perturbation per Figure 4.4.

5.3 Conclusion

In this chapter two approaches were taken toward extending non-equilibrium models to include random driver inhomogeneities. First, an auxiliary equation for a behavior variable z was introduced in Section 5.1, directly mirroring Chapter III. In this case the velocity field is smoother as it depends on white noise through two integrals instead of one. Section 3.4 discusses the similarities the additional z equation coupled to LWR has with non-equilibrium models. In the non-equilibrium context these effects are modeled explicitly. In Chapter III the fundamental diagram most accurately represents deviations of the velocity from equilibrium, whereas in the non-equilibrium case the fundamental diagram describes driver behavior in the absence of non-equilibrium effects. In the latter half of this chapter (Section 5.2), terms similar to those appearing on the right hand side of Equation 2.16 are placed in the acceleration equation directly. In this formulation the types of deviations that may exist in acceleration are determined by the choice of process, allowing less flexibility than the case in which acceleration depends on an additional variable through a chosen function. It also avoids the need for an extended fundamental diagram depending on some parameter z and the difficulty of separating intention (as expressed by a tertiary equation) from action (i.e. acceleration)—the the largest problems with the auxiliary equation.

CHAPTER VI

Conclusion

The addition of stochastic variation to macroscopic traffic modeling with PDE is a difficult task for a variety of reasons, progress toward some of which have been resolved in this thesis. The precise nature of the process underlying variation between drivers is unknown, so the criterion for choosing a stochastic model becomes consistency with what is known about traffic flow and convenience. In particular, though we do not expect a behavior parameter to necessarily be correlated between drivers, because drivers occupy space on the roadway, the process we choose must however be correlated in space such that the statistics over the part of road dominated by one driver are consistent in distribution from one driver to the next. In Chapter II a stochastic heat equation (with linear forcing) was proposed as the underlying stochastic process. This has the advantage of being a process that is relatively well understood in isolation and is posed in the language of PDE. In particular, beginning with a well-defined process ensures that, at a minimum, the stochastic modification and the system to be modified make sense in isolation; the mathematical and modeling uncertainty only lies in the coupling of them. Though the coupled system is mathematically complex, numerical simulation to first order through Monte Carlo methods is relatively straightforward. Numerical simulation allows us to examine individual cases as well as aggregates of certain statistics and evaluate whether this may be an appropriate model for driver inhomogeneity and driver variability over time.

The primary disadvantages of using a stochastic heat equation as an underlying process are a lack of hyperbolicity and an inability to strictly enforce uncorrelated behavior between drivers. We argue the loss of hyperbolicity is not detrimental its intended purpose in traffic modeling, and that it is required for a well-defined process in a continuous space dimension. The inability to strictly enforce uncorrelated behavior between drivers is not a problem inherent in this approach, but a problem inherent in macroscopic modeling in general. Because mean quantities (e.g. traffic density rather than vehicle position) are considered, there is no discrete difference between drivers to begin with. Macroscopic models provide mean quantities over the correct length scales, and this remains the case under the proposed modifications.

6.1 Equilibrium Models

Chapter III focuses on the coupling of LWR to an equation describing a driver dependent property. The resulting system does not explicitly model for acceleration and deceleration. We refer to these models as ‘equilibrium’ models, as the velocity is always in equilibrium with some function of density and the additional parameter z . It is not appropriate to call these ‘first order’ models, as there is a second equation, and, in the unforced case, a connection between these models and ‘second order’ models may be drawn (Section 3.4). The coupling between the two does require a fundamental diagram that depends on both density and the driver dependent parameter ($V(\rho, z)$ rather than $V(\rho)$), and the difficulty inherent in finding such a fundamental diagram is a key limitation to this approach.

These models demonstrate a variety of behavior not seen in equilibrium models. In particular, spontaneous formations of moving jams are formed, and once formed persist for significant periods of time. In addition, nontrivial distributions of certain aggregate parameters were obtained. Of particular note is that the distributions of many aggregate parameters do not remain centered around the nominal value, suggesting that the introduction of driver variation fundamentally changes (rather than symmetrically perturbs) the underlying LWR

model. This suggests the modifications made here do indeed model additional phenomena that may be present in traffic flow as opposed to quantifying uncertainty in a nominal prediction. Though decreased throughput due to inhomogeneity is intuitive in the context of traffic flow, it is unexpected in the context of perturbed PDE models, especially those based on models that cannot demonstrate this phenomenon alone.

6.2 Non-Equilibrium Models

Chapter V has two parts: one in which the ‘auxiliary equation’ approach used for equilibrium models in Chapter III is applied to a non-equilibrium model (Section 5.1) and a fundamentally different approach in which the type of perturbation present in the auxiliary equation is applied directly to the dynamics of acceleration (Section 5.2). The former presents phenomena that are in many ways similar to the equilibrium case. The density and velocity profiles obtained are far smoother; they represent one more integral of white noise than the equilibrium case. Further, it is worth noting non-equilibrium models can evolve large stop-and-go phenomena from small perturbations to initial conditions, making the presence of these structures less surprising. The interesting difference between the nominal and stochastically extended case lies in the size of evolved disturbance as a function of density; these do not directly mirror the unperturbed model (see Figure 5.7). Like the equilibrium case, these models require an extended fundamental diagram, something extremely difficult to obtain in practice.

The introduction of a stochastic perturbation directly into acceleration dynamics is a more invasive modification with less smooth solutions. At this cost a two parameter ‘extended’ fundamental diagram is no longer needed. The numerical results show the same well-defined structures as in the case of the auxiliary equation, though superficially not as smooth. Distributions of aggregate properties do not mirror the dynamics of the unperturbed models, as was the case for the other modified models. These models with ‘direct noise’ are likely the most promising path forward, as the the number of parameters that

must be chosen is far smaller, but solutions continue to demonstrate novel behavior.

6.3 Future Directions

This thesis proposes novel models for incorporating driver variation into macroscopic traffic models and demonstrates that they offer behavior not present in other modeling approaches. However, additional work is required for practical use of these models.

For models with an auxiliary z equation, (i.e. Equations 3.10 and 5.1), the most pressing concern is the requirement of accurate fundamental diagrams depending on this additional property. It is possible that the appropriate extended fundamental diagram may be different in the case of the equilibrium and non-equilibrium models; the differences in quantitative behavior between the two under the same fundamental diagram suggests as much.

Regardless of whether an auxiliary z equation is utilized, most practical traffic systems consist of road networks; the introduction of junctions/intersections into these models is required to model these systems. Though guidance may be taken from existing literature, compatibility conditions on z are, at this point, unclear. In addition, the methods used to approximate the distributions of the desired quantities in these models are unsophisticated and inefficient. For any type of real-time prediction faster approximation methods would be required. However, the present models with the present numerical approach may, should they prove to be accurate given the appropriate parameters, still serve a design purpose, be used as a noisy model in the development of control systems, or be used as training data for building machine-learning predictions.

APPENDICES

APPENDIX A

Car-Following Models

Car following models prescribe dynamics for discrete vehicle positions $x_n(t)$. In the present work we will adopt the convention that vehicles move strictly in the positive direction and are numbered such that $x_n(t) < x_{n+1}(t)$. In [28] Jiang proposed a model combining proportional control models [6] of the form

$$\ddot{x}_n = \frac{\dot{x}_{n+1} - \dot{x}_n}{T} \quad (\text{A.1})$$

and optimal velocity models

$$\ddot{x}_n = \frac{V((x_{n+1} - x_n)^{-1}) - \dot{x}_n}{\tau} \quad (\text{A.2})$$

to obtain so-called ‘full velocity difference’ models

$$\ddot{x}_n = \frac{V((x_{n+1} - x_n)^{-1}) - \dot{x}_n}{\tau} + \frac{\dot{x}_{n+1} - \dot{x}_n}{T} \quad (\text{A.3})$$

where τ and T are (positive) constants. Equation A.1 is a simplification of those in [6]; it is however the starting point used by Jiang [28]. It is common in the context of car following models to write the fundamental diagram as a function of spacing $s_n = x_{n+1} - x_n$. To remain

consistent with the fundamental diagrams discussed in Section 1.2, we will write

$$V(s_n^{-1}) = W(s_n). \quad (\text{A.4})$$

Jiang simultaneously published a continuum model based on Equation A.3; this was later expanded upon by [59, 58] to obtain the model we will focus on in Section 4.4.

Because we will be perturbing continuum models based upon this equation, stability of this model is of particular interest, especially as it relates to stability results for the related continuum model discussed in Section 4.1.2. Wang [66] derived a gain function for Equation A.3 in the special case in which the fundamental diagram is linear in vehicle spacing. The approach taken here allows for a general form of the fundamental diagram.

For simplicity, assume a periodic domain and define $W(s) = V(s^{-1})$ where s is vehicle spacing (recall this includes the length of the car). Let $x_{N+1}(t) = x_1(t) + L$ to obtain periodicity and let $d_n(t) = x_{n+1}(t) - x_n(t)$. What follows is nearly identical when done in terms of vehicle position $x_n(t)$, but writing it in terms of vehicle distances makes the conclusions more straightforward. If this analysis is carried out in terms of position, we are required to assume unperturbed forward motion can be identified with the zero eigenvalue, but the author is not able to prove this is the case. Writing the system in terms of vehicle spacing still precludes us from asserting stability through our linearized analysis as there are zero eigenvalues present. We have

$$\ddot{d}_n = f_n(d_n, d_{n+1}, \dot{d}_n, \dot{d}_{n+1}) = \frac{W(d_{n+1}) - W(d_n) - \dot{d}_n}{\tau} + \frac{\dot{d}_{n+1} - \dot{d}_n}{T}. \quad (\text{A.5})$$

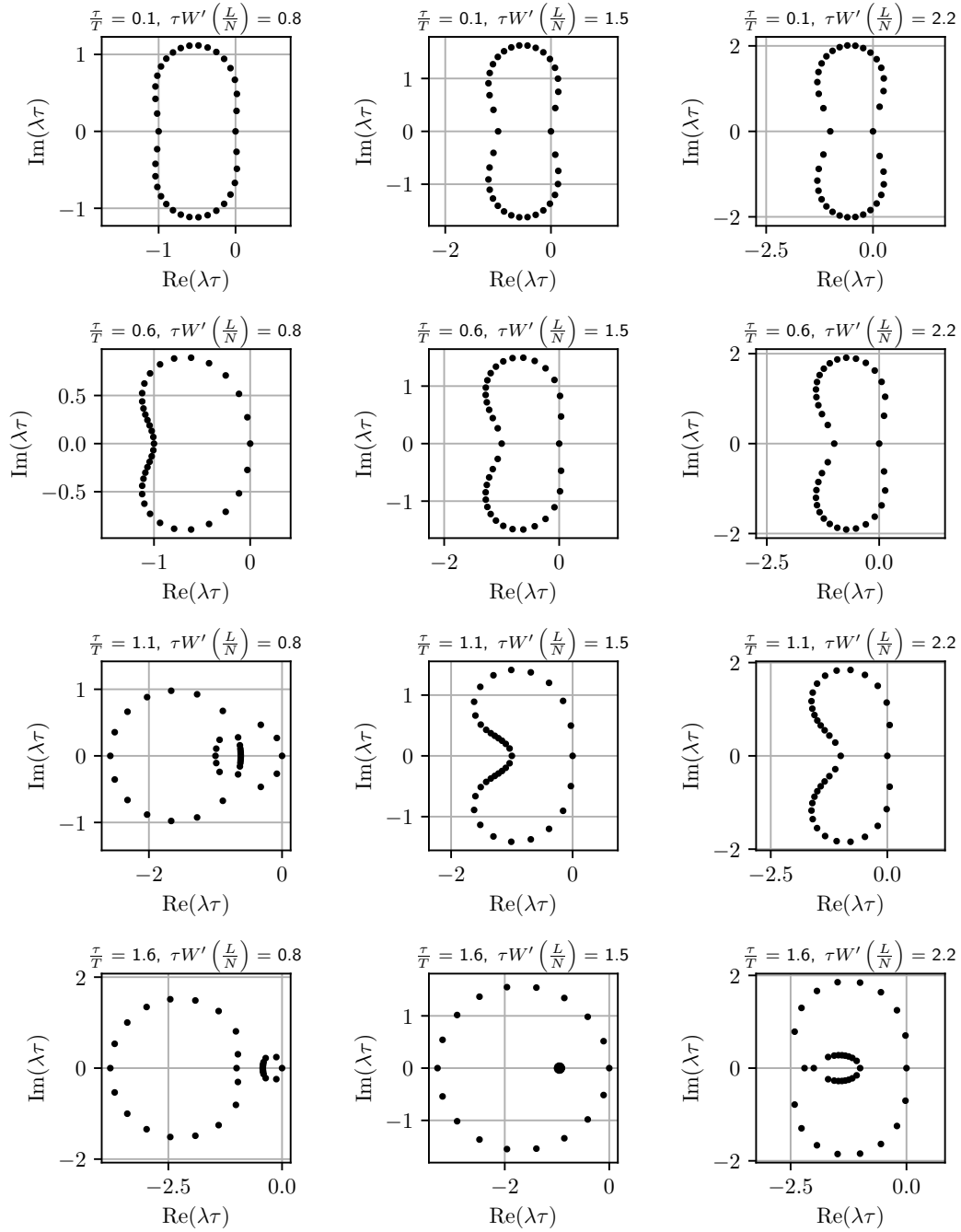


Figure A.1: Example non-dimensional eigenvalues of the Jacobian (Equation A.9) evaluated at the steady state of equidistant vehicles.

Using

$$\begin{aligned}\frac{\partial f_n}{\partial d_n} &= -\frac{W'(d_n)}{\tau} \\ \frac{\partial f_n}{\partial d_{n+1}} &= \frac{W'(d_{n+1})}{\tau} \\ \frac{\partial f_n}{\partial \dot{d}_n} &= -\left(\frac{1}{\tau} + \frac{1}{T}\right) \\ \frac{\partial f_n}{\partial \dot{d}_{n+1}} &= \frac{1}{T}\end{aligned}$$

Let $g_n = \frac{W'(d_n)}{\tau}$ and $\alpha = \frac{1}{\tau} + \frac{1}{T}$. Note that $g_n \geq 0$. Then, choosing a point $(\mathbf{d}^0, \dot{\mathbf{d}}^0)$, we have

$$\mathbf{f} = \underbrace{\mathbf{f}(\mathbf{d}, \dot{\mathbf{d}})}_{\mathbf{f}^0} + \begin{bmatrix} \frac{\partial \mathbf{f}}{\partial \mathbf{d}} & \frac{\partial \mathbf{f}}{\partial \dot{\mathbf{d}}} \end{bmatrix} \begin{bmatrix} \mathbf{d} - \mathbf{d}^0 \\ \dot{\mathbf{d}} - \dot{\mathbf{d}}^0 \end{bmatrix} + \mathcal{O}\left(\|\mathbf{x} - \mathbf{x}^0\|^2 + \|\dot{\mathbf{x}} - \dot{\mathbf{x}}^0\|^2\right) \quad (\text{A.6})$$

where

$$\frac{\partial \mathbf{f}}{\partial \mathbf{d}} = \begin{bmatrix} -g_1 & g_2 & & & \\ & -g_2 & \ddots & & \\ & & \ddots & g_N & \\ g_1 & & & -g_N & \end{bmatrix} \quad \text{and} \quad \frac{\partial \mathbf{f}}{\partial \dot{\mathbf{d}}} = \begin{bmatrix} -\alpha & T^{-1} & & & \\ & -\alpha & \ddots & & \\ & & \ddots & T^{-1} & \\ T^{-1} & & & -\alpha & \end{bmatrix} \quad (\text{A.7})$$

In light of this, the ODE

$$\frac{d}{dt} \begin{bmatrix} \mathbf{d} \\ \dot{\mathbf{d}} \end{bmatrix} = \begin{bmatrix} \dot{\mathbf{d}} \\ \mathbf{f} \end{bmatrix} \quad (\text{A.8})$$

has the Jacobian

$$\begin{bmatrix} 0 & I \\ \frac{\partial \mathbf{f}}{\partial \mathbf{d}} & \frac{\partial \mathbf{f}}{\partial \dot{\mathbf{d}}} \end{bmatrix}. \quad (\text{A.9})$$

Using the decomposition typically found in the context of the Schur complement

$$\begin{bmatrix} -\lambda I & I \\ \frac{\partial \mathbf{f}}{\partial \mathbf{d}} & \frac{\partial \mathbf{f}}{\partial \dot{\mathbf{d}}} - \lambda I \end{bmatrix} = \begin{bmatrix} I & 0 \\ -\frac{1}{\lambda} \frac{\partial \mathbf{f}}{\partial \dot{\mathbf{d}}} & I \end{bmatrix} \begin{bmatrix} -\lambda I & 0 \\ 0 & -\lambda I + \frac{\partial \mathbf{f}}{\partial \dot{\mathbf{d}}} - \frac{1}{\lambda} \frac{\partial \mathbf{f}}{\partial \mathbf{d}} \end{bmatrix} \begin{bmatrix} I & -\frac{1}{\lambda} \\ 0 & I \end{bmatrix} \quad (\text{A.10})$$

the characteristic polynomial is

$$p(\lambda) = (-\lambda)^N \det \left(-\lambda I + \frac{\partial \mathbf{f}}{\partial \dot{\mathbf{d}}} - \frac{1}{\lambda} \frac{\partial \mathbf{f}}{\partial \mathbf{d}} \right). \quad (\text{A.11})$$

At this point we evaluate at the steady state

$$\begin{bmatrix} d_1^0 \\ d_2^0 \\ \vdots \\ d_N^0 \\ \dot{d}_1^0 \\ \dot{d}_2^0 \\ \vdots \\ \dot{d}_N^0 \end{bmatrix} = \begin{bmatrix} \frac{L}{N} \\ \frac{L}{N} \\ \vdots \\ \frac{L}{N} \\ 0 \\ 0 \\ \vdots \\ 0 \end{bmatrix}$$

and observe that

$$-\lambda I + \frac{\partial \mathbf{f}}{\partial \mathbf{d}} \Big|_{(\mathbf{d}^0, \mathbf{d}^0)} - \frac{1}{\lambda} \frac{\partial \mathbf{f}}{\partial \mathbf{d}} \Big|_{(\mathbf{d}^0, \mathbf{d}^0)} \quad (\text{A.12})$$

is circulant, i.e. it is of the form

$$\begin{bmatrix} a_1 & a_N & \cdots & a_2 \\ a_2 & a_1 & \cdots & a_3 \\ \vdots & \vdots & \ddots & \vdots \\ a_N & a_{N-1} & \cdots & a_1 \end{bmatrix}.$$

It is well known circulant matrices are diagonalizable by the Discrete Fourier Transform (DFT). We then have

$$p(\lambda) = \prod_{j=0}^{N-1} \left(\lambda^2 + \left(\alpha - \frac{\omega_j}{T} \right) \lambda - g \cdot (1 - \omega_j) \right) \quad (\text{A.13})$$

where $\omega_j = \exp\left(\frac{2\pi i j}{N}\right)$, with roots

$$\lambda_{j,k} = \frac{1}{2} \left(-\alpha + \frac{\omega_j}{T} - (-1)^k \sqrt{\left(\alpha - \frac{\omega_j}{T} \right)^2 - 4g \cdot (1 - \omega_j)} \right). \quad (\text{A.14})$$

Given explicit formulas for eigenvalues (Equation A.14), it is possible to identify regions in which instability is expected (Figure A.1). This informs our selection of parameters if we wish to show stop and go phenomena in car-following models. Determining whether car-following stability can also inform behavior of the continuum models directly derived from those car-following models (e.g. Section 4.4) remains an open question.

Both Wang [66] and Laval [36] introduce stochastic perturbations to car-following models, including the optimal velocity model. Wang [66] proposed a variety of stochastic modifications to car-following models. In contrast to the model that will be discussed here

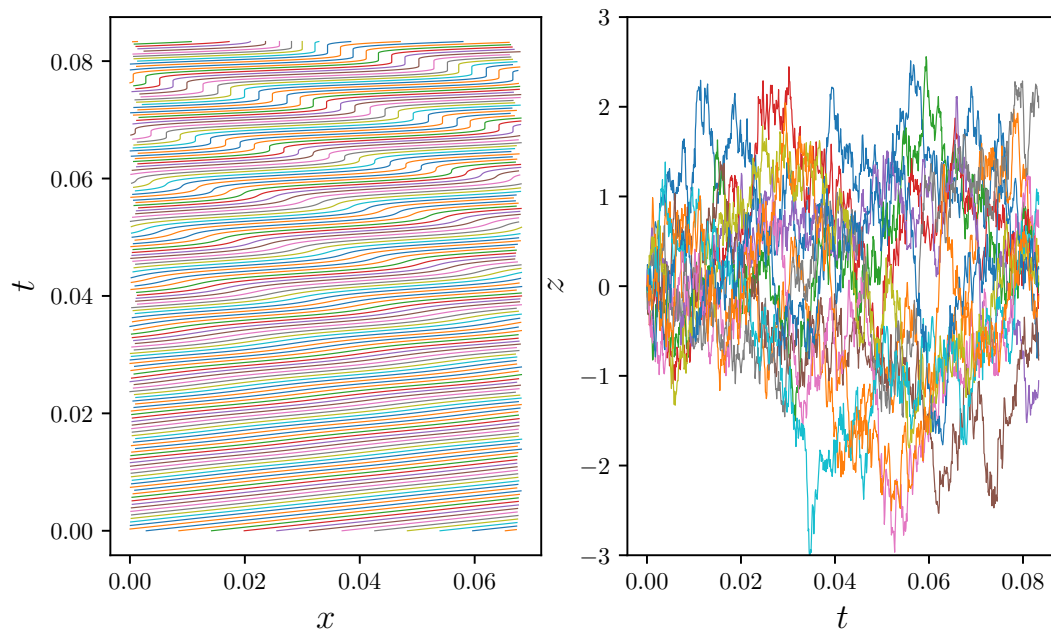


Figure A.2: An example realization of the car-following model Equation A.19. The left shows vehicle trajectories exhibiting development of stop and go waves whereas the right shows the corresponding behavioral ‘ z_n ’ variables.

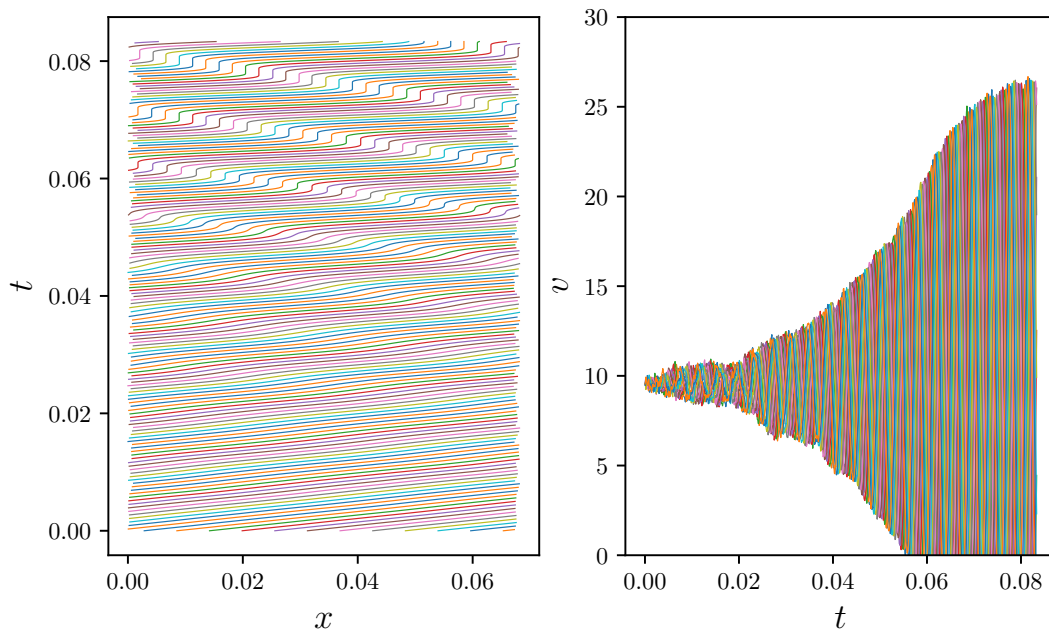


Figure A.3: An example realization of the car-following model Equation A.20. The left shows vehicle trajectories exhibiting development of stop and go patterns whereas the right shows the corresponding velocities (v_n).

(Equation A.16), all of the stochastic modifications proposed by Wang et al were direct perturbations of kinematic quantities rather than auxiliary ‘behavior’ equations. Laval [36] used the optimal velocity model

$$\begin{aligned} dx_n &= \dot{x}_n dt \\ d\dot{x}_n &= \left(\frac{V((x_{n+1} - x_n)^{-1}) - \dot{x}_n}{\tau} \right) dt + \eta dW_n \end{aligned} \quad (\text{A.15})$$

to obtain traffic waves that resemble the congestion waves seen in traffic data. We will discuss this approach applied to a modified ‘full velocity difference model’ (Equation 4.36) as an analog to stochastic continuum models discussed in Section 5.2.

In Chapter III we added an additional equation for a behavior variable z . In Section 3.3 we chose coefficients in the spirit of having z vary on the scale of an individual vehicle. Here we can choose processes that are truly independent for each vehicle by introducing N independent Ornstein-Uhlenbeck processes $z_n(t)$, one for each vehicle; this is very similar to the approach used for pedestrian traffic models in [62]:

$$\begin{aligned} dx_n &= \dot{x}_n dt \\ d\dot{x}_n &= \left(\frac{V(((x_{n+1} - x_n)\rho^{\text{jam}})^{-1}, z_n) - \dot{x}_n}{\tau} + \frac{\dot{x}_{n+1} - \dot{x}_n}{T} \right) dt \\ dz_n &= -\frac{z}{\tau^z} dt + \eta dW_n \end{aligned} \quad (\text{A.16})$$

where W_n are independent and identically distributed (i.i.d.) Weiner processes. In this case, the independent stochastic processes are entirely unaffected by the vehicles around them, and therefore the velocities prescribed by the fundamental diagram are not tempered to the same extent by nearby vehicles. In this formulation faster vehicles and slower vehicles will readily collide for a wide variety of parameters. In addition, this formulation allows for negative velocities to be attained. For example, in a moment in which $\dot{x}_n = 0$ and $\dot{x}_{n+1} \approx 0$

we can easily have z_n such that

$$\frac{V(((x_{n+1} - x_n)\rho^{\text{jam}})^{-1}, z_n)}{\tau} \leq \frac{\dot{x}_{n+1}}{T}. \quad (\text{A.17})$$

One strategy for addressing this problem is to utilize a different value of T for either sign of $\dot{x}_{n+1} - \dot{x}_n$ and/or a different value of τ for either sign of $V((x_{n+1} - x_n)^{-1}) - \dot{x}_n$. A discussion of this can be found in [28]. A version of this idea,

$$\begin{aligned} dx_n &= \dot{x}_n dt \\ d\dot{x}_n &= \max\left(\frac{V(((x_{n+1} - x_n)\rho^{\text{jam}})^{-1}, z_n) - \dot{x}_n}{\tau}, 0\right) dt + \min\left(\frac{\dot{x}_{n+1} - \dot{x}_n}{T}, 0\right) dt \\ dz_n &= -\frac{z}{\tau z} dt + \eta dW_n \end{aligned} \quad (\text{A.18})$$

was considered and yielded similar results. A simpler but less elegant solution that guarantees no negative velocities is to simply ignore negative velocities:

$$\begin{aligned} dx_n &= \max(\dot{x}_n, 0) dt \\ d\dot{x}_n &= \left(\frac{V(((x_{n+1} - x_n)\rho^{\text{jam}})^{-1}, z_n) - \dot{x}_n}{\tau} + \frac{\dot{x}_{n+1} - \dot{x}_n}{T}\right) dt \\ dz_n &= -\frac{z}{\tau z} dt + \eta dW_n. \end{aligned} \quad (\text{A.19})$$

When implemented with periodic boundary conditions and in the correct regime, clear stop and go patterns develop (Figure A.2). These models are in many ways analogs to what is presented in Chapter V.

An alternative is to introduce noise directly to the velocities:

$$\begin{aligned} dx_n &= \max(\dot{x}_n, 0) dt \\ d\dot{x}_n &= \left(\frac{V(((x_{n+1} - x_n)\rho^{\text{jam}})^{-1}) - \dot{x}_n}{\tau} + \frac{\dot{x}_{n+1} - \dot{x}_n}{T}\right) + \eta dW_n. \end{aligned} \quad (\text{A.20})$$

This approach is simpler on its face but contains parameters that are much more difficult

to interpret and determine appropriate values for. This is largely a consequence of the stochastic process no longer being independent of the traffic dynamics—the relaxation terms depend on the current state of traffic. This approach results in very similar stop-and-go patterns (Figure A.3).

BIBLIOGRAPHY

BIBLIOGRAPHY

- [1] Timur Alperovich and Alexandros Sopasakis. “Stochastic Description of Traffic Flow”. en. In: *Journal of Statistical Physics* 133.6 (Dec. 2008), pp. 1083–1105. ISSN: 0022-4715, 1572-9613.
- [2] A. Aw and M. Rascle. “Resurrection of ”Second Order” Models of Traffic Flow”. en. In: *SIAM Journal on Applied Mathematics* 60.3 (Jan. 2000), pp. 916–938. ISSN: 0036-1399, 1095-712X.
- [3] Werner Brilon and Jan Lohoff. “Speed-flow Models for Freeways”. en. In: *Procedia - Social and Behavioral Sciences* 16 (2011), pp. 26–36. ISSN: 18770428.
- [4] S.C. Calvert. “Stochastic Macroscopic Analysis and Modelling for Traffic Management”. en. PhD thesis. Delft University of Technology, 2016.
- [5] Simeon Calvert et al. “Vehicle Specific Behaviour in Macroscopic Traffic Modelling through Stochastic Advection Invariant”. en. In: *Transportation Research Procedia* 10 (2015), pp. 71–81. ISSN: 23521465.
- [6] Robert E. Chandler, Robert Herman, and Elliott W. Montroll. “Traffic Dynamics: Studies in Car Following”. en. In: *Operations Research* 6.2 (Apr. 1958), pp. 165–184. ISSN: 0030-364X, 1526-5463.
- [7] Alina Chertock et al. “Pedestrian Flow Models with Slowdown Interactions”. en. In: *Mathematical Models and Methods in Applied Sciences* 24.02 (Feb. 2014), pp. 249–275. ISSN: 0218-2025, 1793-6314.
- [8] Kang-Ching Chu, Romesh Saigal, and Kazuhiro Saitou. “Real-Time Traffic Prediction and Probing Strategy for Lagrangian Traffic Data”. en. In: *IEEE Transactions on Intelligent Transportation Systems* 20.2 (Feb. 2019), pp. 497–506. ISSN: 1524-9050, 1558-0016.
- [9] Kang-Ching Chu, Romesh Saigal, and Kazuhiro Saitou. “Stochastic Lagrangian Traffic flow modeling and real-time traffic prediction”. en. In: *2016 IEEE International Conference on Automation Science and Engineering (CASE)*. Fort Worth, TX, USA: IEEE, Aug. 2016, pp. 213–218. ISBN: 978-1-5090-2409-4.
- [10] Kang-Ching Chu et al. “Validation of stochastic traffic flow model with microscopic traffic simulation”. en. In: Trieste, Italy: IEEE, Aug. 2011, p. 6.
- [11] Carlos F. Daganzo. “Requiem for second-order fluid approximations of traffic flow”. en. In: *Transportation Research Part B: Methodological* 29.4 (Aug. 1995), pp. 277–286. ISSN: 01912615.

- [12] Giacomo Dimarco and Andrea Tosin. “The Aw-Rascle traffic model: Enskog-type kinetic derivation and generalisations”. en. In: *Journal of Statistical Physics* 178.1 (Jan. 2020). arXiv: 1906.10665, pp. 178–210. ISSN: 0022-4715, 1572-9613.
- [13] Lawrence C Evans. *Partial Differential Equations*. Second. Vol. 19. Graduate Studies in Mathematics. American Mathematical Society, 2010. ISBN: 978-0-8218-4974-3.
- [14] Shimao Fan. “Data-Fitted Generic Second Order Macroscopic Traffic Flow Models”. en. Dissertation. Temple University, June 2013.
- [15] Shimao Fan, Michael Herty, and Benjamin Seibold. “Comparative model accuracy of a data-fitted generalized Aw-Rascle-Zhang model”. en. In: *arXiv:1310.8219 [physics]* (June 2014). arXiv: 1310.8219.
- [16] Shimao Fan and Benjamin Seibold. “A comparison of data-fitted first order traffic models and their second order generalizations via trajectory and sensor data”. en. In: *arXiv:1208.0382 [physics]* (June 2013). arXiv: 1208.0382.
- [17] Akiko Fukuda, Etsuo Segawa, and Sennosuke Watanabe. “Cellular automata traffic flow model derived through the ultradiscrete limit of the correlated random walk”. en. In: *arXiv:2104.14009 [math-ph]* (Apr. 2021). arXiv: 2104.14009.
- [18] Mauro Garavello, Ke Han, and Benedetto Piccoli. *Models for Vehicular Traffic on Networks*. American Institute of Mathematical Sciences, 2016.
- [19] Stephan Gerster, Michael Herty, and Elisa Iacomini. “Stability analysis of a hyperbolic stochastic Galerkin formulation for the Aw-Rascle-Zhang model with relaxation”. en. In: *arXiv:2102.09359 [cs, math]* (Feb. 2021). arXiv: 2102.09359.
- [20] Paola Goatin and Elena Rossi. “A multi-lane macroscopic traffic flow model for simple networks”. en. In: *arXiv:1904.04535 [math]* (Apr. 2019). arXiv: 1904.04535.
- [21] Harold Greenberg. “An Analysis of Traffic Flow”. en. In: *Operations Research* 7.1 (Feb. 1959), pp. 79–85. ISSN: 0030-364X, 1526-5463.
- [22] Bruce D Greenshields. “A Study of Traffic Capacity”. In: *Proceedings of the Fourteenth Annual Meeting*. Vol. 14. Washington, DC: Highway Research Board, Dec. 1935, pp. 448–477.
- [23] Martin Hairer. *An Introduction to Stochastic PDEs*. en. July 2009.
- [24] Dirk Helbing. “Improved fluid-dynamic model for vehicular traffic”. In: *Physical Review E* 51.4 (1995), p. 3164.
- [25] Dirk Helbing. “Traffic and related self-driven many-particle systems”. In: *Reviews of modern physics* 73.4 (2001), p. 1067.
- [26] Dirk Helbing and Anders Johansson. “On the Controversy around Daganzo’s Requiem for and Aw-Rascle’s Resurrection of Second-Order Traffic Flow Models”. en. In: *The European Physical Journal B* 69.4 (June 2009). arXiv: 0805.3402, pp. 549–562. ISSN: 1434-6028, 1434-6036.
- [27] Rui Jiang, Qing-Song Wu, and Zuo-Jin Zhu. “A new continuum model for traffic flow and numerical tests”. en. In: *Transportation Research Part B: Methodological* 36.5 (June 2002), pp. 405–419. ISSN: 01912615.

- [28] Rui Jiang, Qingsong Wu, and Zuojin Zhu. “Full velocity difference model for a car-following theory”. en. In: *Physical Review E* 64.1 (June 2001), p. 017101. ISSN: 1063-651X, 1095-3787.
- [29] B. S. Kerner. “Experimental Features of Self-Organization in Traffic Flow”. en. In: *Physical Review Letters* 81.17 (Oct. 1998), pp. 3797–3800. ISSN: 0031-9007, 1079-7114.
- [30] B. S. Kerner and P. Konh user. “Cluster effect in initially homogeneous traffic flow”. en. In: *Physical Review E* 48.4 (Oct. 1993), R2335–R2338. ISSN: 1063-651X, 1095-3787.
- [31] Boris S. Kerner. *The Physics of Traffic*. Ed. by J. A. Scott Kelso. Understanding Complex Systems. Berlin, Heidelberg: Springer Berlin Heidelberg, 2004. ISBN: 978-3-540-40986-1.
- [32] Davar Khoshnevisan. *Analysis of Stochastic Partial Differential Equations*. en. Vol. 119. CBMS Regional Conference Series in Mathematics. Providence, Rhode Island: American Mathematical Society, June 2014. ISBN: 978-1-4704-1547-1.
- [33] Megan M. Khoshyaran and Jean-Patrick Lebacque. “A Stochastic Macroscopic Traffic Model Devoid of Diffusion”. en. In: *Traffic and Granular Flow ’07*. Berlin, Heidelberg: Springer Berlin Heidelberg, 2007, pp. 139–150. ISBN: 978-3-540-77073-2.
- [34] Jorge A. Laval and Bhargava R. Chilukuri. “The Distribution of Congestion on a Class of Stochastic Kinematic Wave Models”. en. In: *Transportation Science* 48.2 (May 2014), pp. 217–224. ISSN: 0041-1655, 1526-5447.
- [35] Jorge A. Laval and Ludovic Leclercq. “A mechanism to describe the formation and propagation of stop-and-go waves in congested freeway traffic”. en. In: *Philosophical Transactions of the Royal Society A: Mathematical, Physical and Engineering Sciences* 368.1928 (Oct. 2010), pp. 4519–4541. ISSN: 1364-503X, 1471-2962.
- [36] Jorge A. Laval, Christopher S. Toth, and Yi Zhou. “A parsimonious model for the formation of oscillations in car-following models”. en. In: *Transportation Research Part B: Methodological* 70 (Dec. 2014), pp. 228–238. ISSN: 01912615.
- [37] Jean-Patrick Lebacque, Salim Mammar, and Habib HAJ Salem. “Generic Second Order Traffic Flow Modelling”. In: *Transportation and Traffic Theory 2007. Papers Selected for Presentation at ISTTT17*. London, England, 2007.
- [38] Jean-Patrick Lebacque, Habib HAJ Salem, and Salim Mammar. “Second order traffic flow modeling: supply-demand analysis of the inhomogeneous riemann problem and of boundary conditions”. en. In: *Advanced OR and AI Methods in Transportation* (Jan. 2005), p. 9.
- [39] Randall J LeVeque. *Finite Volume Methods for Hyperbolic Problems*. Cambridge University Press, 2002.
- [40] Randall J LeVeque. *Some Traffic Flow Models Illustrating Interesting Hyperbolic Behavior*. en. 2001.
- [41] Randall J. LeVeque. *Numerical Methods for Conservation Laws*. en. Basel: Birkh user Basel, 1992. ISBN: 978-3-0348-8629-1.

- [42] Jia Li et al. “Analysis of LWR model with fundamental diagram subject to uncertainties”. en. In: *Transportmetrica* 8.6 (Nov. 2012), pp. 387–405. ISSN: 1812-8602, 1944-0987.
- [43] M. J. Lighthill and G. B. Whitham. “On kinematic waves II. A theory of traffic flow on long crowded roads”. en. In: *Proceedings of the Royal Society of London. Series A. Mathematical and Physical Sciences* 229.1178 (May 1955), pp. 317–345. ISSN: 2053-9169.
- [44] Michel Mandjes and Jaap Storm. “A Gaussian segment-based traffic flow model for the design and control of transport networks”. en. In: *arXiv:2007.07339 [math]* (July 2020). arXiv: 2007.07339.
- [45] Liou Meng-Sing and Bram Van Leer. “Splitting of Inviscid Fluxes for Real Gases”. In: *Journal of Computational Physics* 87 (1990).
- [46] Kamel Mohamed, Mohammed Seaid, and Mostafa Zahri. “A finite volume method for scalar conservation laws with stochastic time–space dependent flux functions”. en. In: *Journal of Computational and Applied Mathematics* 237.1 (Jan. 2013), pp. 614–632. ISSN: 03770427.
- [47] Kai Nagel and Michael Schreckenberg. “Traffic jam dynamics in stochastic cellular automata”. In: Stuttgart, Germany, Aug. 1995.
- [48] G.F. Newell. “A simplified theory of kinematic waves in highway traffic, part I: General theory”. en. In: *Transportation Research Part B: Methodological* 27.4 (Aug. 1993), pp. 281–287. ISSN: 01912615.
- [49] D. Ngoduy. “Multiclass first-order traffic model using stochastic fundamental diagrams”. en. In: *Transportmetrica* 7.2 (Mar. 2011), pp. 111–125. ISSN: 1812-8602, 1944-0987.
- [50] *NGSIM*. 2005.
- [51] Daiheng Ni, Hui K. Hsieh, and Tao Jiang. “Modeling phase diagrams as stochastic processes with application in vehicular traffic flow”. en. In: *Applied Mathematical Modelling* 53 (Jan. 2018), pp. 106–117. ISSN: 0307904X.
- [52] Harold J Payne. “Models of freeway traffic and control”. In: *Mathematical models of public systems* (1971), pp. 51–61.
- [53] Daniel Revuz and Marc Yor. *Continuous martingales and brownian motion*. en. OCLC: 758879947. Berlin; Heidelberg: Springer, 2005. ISBN: 978-3-540-64325-8.
- [54] Paul I. Richards. “Shock Waves on the Highway”. en. In: *Operations Research* 4.1 (Feb. 1956), pp. 42–51. ISSN: 0030-364X, 1526-5463.
- [55] Bernard Schnetzler and Xavier Louis. “Anisotropic second-order models and associated fundamental diagrams”. en. In: *Transportation Research Part C: Emerging Technologies* 27 (Feb. 2013), pp. 131–139. ISSN: 0968090X.
- [56] Michael Schreckenberg and Kai Nagel. “Physical modelling of traffic with stochastic cellular automata”. In: *28th ISATA*. Stuttgart, Germany, Aug. 1995.

- [57] Joel Smoller. *Shock Waves and Reaction—Diffusion Equations*. en. Ed. by M. Artin et al. Vol. 258. Grundlehren der mathematischen Wissenschaften. New York, NY: Springer New York, 1994. ISBN: 978-1-4612-6929-8.
- [58] Jiah Song. “Mathematical Modeling and Simulations of Traffic Flow”. en. PhD thesis. 2019.
- [59] Jiah Song and Smadar Karni. “A Second Order Traffic Flow Model with Lane Changing”. en. In: *Journal of Scientific Computing* 81.3 (Dec. 2019), pp. 1429–1445. ISSN: 0885-7474, 1573-7691.
- [60] Yuki Sugiyama et al. “Traffic jams without bottlenecks—experimental evidence for the physical mechanism of the formation of a jam”. en. In: *New Journal of Physics* 10.3 (Mar. 2008), p. 033001. ISSN: 1367-2630.
- [61] Elvira Thonhofer and Stefan Jakubek. “Investigation of stochastic variation of parameters for a macroscopic traffic model”. en. In: *Journal of Intelligent Transportation Systems* 22.6 (Nov. 2018), pp. 547–564. ISSN: 1547-2450, 1547-2442.
- [62] Antoine Tordeux and Andreas Schadschneider. “White and relaxed noises in optimal velocity models for pedestrian flow with stop-and-go waves”. en. In: *Journal of Physics A: Mathematical and Theoretical* 49.18 (May 2016), p. 185101. ISSN: 1751-8113, 1751-8121.
- [63] Martin Treiber and Arne Kesting. *Traffic Flow Dynamics*. en. Berlin, Heidelberg: Springer Berlin Heidelberg, 2013. ISBN: 978-3-642-32459-8.
- [64] Martin Treiber, Arne Kesting, and Dirk Helbing. “Three-phase traffic theory and two-phase models with a fundamental diagram in the light of empirical stylized facts”. en. In: *Transportation Research Part B: Methodological* 44.8-9 (Sept. 2010). arXiv: 1004.5545, pp. 983–1000. ISSN: 01912615.
- [65] Haizhong Wang et al. “Stochastic modeling of the equilibrium speed-density relationship”. en. In: *Journal of Advanced Transportation* 47.1 (Jan. 2013), pp. 126–150. ISSN: 01976729.
- [66] Yu Wang et al. “Stability Analysis of Stochastic Linear Car-Following Models”. en. In: *Transportation Science* (Jan. 2020), trsc.2019.0932. ISSN: 0041-1655, 1526-5447.
- [67] H M Zhang. “A non-equilibrium traffic model devoid of gas-like behavior”. en. In: *Transportation Research Part B: Methodological* 36.3 (Mar. 2002), pp. 275–290.
- [68] H. M. Zhang. “Comment on “On the controversy around Daganzo’s requiem for and Aw-Rascle’s resurrection of second-order traffic flow models” by D. Helbing and A.F. Johansson: What faster-than-traffic characteristic speeds mean for vehicular traffic flow”. en. In: *The European Physical Journal B* 69.4 (June 2009), pp. 563–568. ISSN: 1434-6028, 1434-6036.